Dissertation
submitted to the
Combined Faculties for the
Natural Sciences and for Mathematics
of the Ruperto–Carola University of Heidelberg, Germany
for the degree of
Doctor of Natural Sciences

Put forward by

Diplom-Physiker: **Christoph Johannes Barth**
Born in: **Heidelberg, Germany**

Oral examination: February 1st, 2012

Investigating AHL-lipid bilayer interactions using nonlinear optical spectroscopy

Referees: **Prof. Dr. Joachim Spatz**
Prof. Dr. Patrick Koelsch

Publications related to the work in this thesis

D. Jakubczyk, C. Barth, F. Anastassacos, P. Koelsch, U. Schepers, G. Brenner-Weiss, S. Bräse, "The interaction of N-acyl-L-homoserine lactone (AHL) inter-kingdom signalling molecules with model lipid membranes", *Analytical and Bioanalytical Chemistry*, submitted (NOV 2011)

C. Barth, D. Jakubczyk, F. Anastassacos, U. Schepers, G. Brenner-Weiss, S. Bräse, P. Koelsch "Spectroscopic investigation of acylated homoserine lactones of different chain length with respect to orientation and diffusion behavior in model lipid membranes", *Biophysical Journal*, in preparation

M. Muglali, C. Barth, P. Koelsch, A. Erbe "Combined spectroscopic and electrochemical investigations on the unusual desorption behavior of terphenyl-size thiolate self-assembled monolayers", in preparation

C. Barth, M. Muglali, A. Erbe, P. Koelsch "Optical $\chi^{(3)}$ Effects in Thin Organic Films at Charged Metal/Liquid Interfaces", *Physical Review Letters*, in preparation

Other contributions as a PhD student

R. Konietzny, C. Barth, S. Harms, K. Raetzke, P. Koelsch, C. Staudt, "Structural investigations and swelling behavior of 6FDA-copolyimide thin films", *Polymer International*, Webpublished (JUN 2011).

M. Bruns, V. Trouillet, S. Engin, D. Wedlich, P. Nagel, C. Howell, C. Barth, P. Koelsch, "Structure and Chemical Composition of Thiol-SAMs for Immobilization of Biomolecules", *Surface and Interface Analysis*, submitted (AUG 2011)

The interaction of biological molecules with model membranes as studied with SFG spectroscopy

Acylated homoserine lactones (AHLs) play an important role in bacterial infection and biofilm formation and also allow communication between microorganisms and their eukaryotic host cells (Inter-kingdom signaling). The detailed mechanism of these interactions is yet unknown. To mimic interactions between AHLs and cell membranes, the incorporation of AHLs with different chain lengths in supported lipid bilayers (SLBs) was studied using vibrational sum-frequency generation (SFG) spectroscopy. Deuterium-labelled AHLs were synthesized to prevent the overlap of spectroscopic bands allowing the detailed analysis of the interaction. Three AHLs of different chain length were investigated and their orientation within the lipid bilayer was determined. Moreover, the development of AHL-related SFG signals over 5 h was studied providing evidence that AHLs can cross the bilayer in a flip-flop process. However, the determined half life of this process is of the order of days indicating that it is not relevant for the signaling in bacterial biofilms.

Furthermore, to relate structural changes with terminal groups and chain lengths, differently terminated self-assembled monolayers (SAMs) were studied with SFG spectroscopy in air and *in situ*. Pyridine-terminated SAMs present a different behavior upon electrochemical desorption depending on an odd or even numbered aliphatic chain. Using SFG spectroscopy it was determined that even numbered pyridine-terminated self-assembled monolayers retain their structure, whereas odd numbered monolayers lose their conformation upon desorption. Furthermore, nonlinear third-order effects were observed with this experimental setup and could be readily explained with theoretical predictions.

Die Untersuchung der Interaktion biologischer Moleküle mit Modelmembranen mit SFG Spektroskopie

Azylierte Homoserin-Lactone (AHLs) werden von gramnegativen Bakterien synthetisiert. Diese *Quorum sensing* Moleküle spielen eine wichtige Rolle bei bakteriellen Infektionen und der Bildung von Biofilmen. Darüber hinaus erlauben sie die Kommunikation zwischen den Mikroorganismen und den Zellen ihres eukaryotischen Wirtes (Inter-kingdom Signaling). Der detaillierte Mechanismus dieser Interaktion ist jedoch noch weitgehend unbekannt. Um die Interaktion zwischen AHLs und Membranen nachzubilden, wurde die Inklusion von AHLs verschiedener KettenlŠnge in Modelmembranen mit Hilfe von Summenfrequenzerzeugungsspektroskopie (SFG Spektroskopie) studiert. Mit Deuterium markierte AHLs wurden synthetisiert, um den spektroskopischen Überlapp mit anderen Banden zu verhindern, was eine detaillierte Analyse der Interaktionen erlaubt. Drei AHLs verschiedener Kettenlänge wurden untersucht und ihre Orientierung in der Lipiddoppelschicht bestimmt. Darüber hinaus wurde über 5 Stunden die Entwicklung des SFG-Signals der AHLs beobachtet, was darauf hinweist, dass AHLs in einer Art Flip-Flop-Prozess durch die Doppelschicht flippen können. Jedoch lag die Halbwertszeit dieser Prozesse bei Tagen, was darauf hindeutet, dass er für das Signaling in Biofilmen nicht relevant ist.

Um außerdem strukturelle Änderungen mit verschiedenen Endgruppen und Kettenlängen in Verbindung zu bringen, wurden selbst-aggregierende Monolagen (SAMs) mit SFG Spektroskopie in Luft und *in situ* studiert. SAMs mit Pyridinendgruppen zeigen ein unterschiedliches Verhalten bei elektrochemischer Desorption je nachdem, ob sie eine aliphatische Kette mit gerader oder ungerader Atomzahl besitzen. Mit Hilfe von SFG Spektroskopie konnte bestimmt werden, dass Monolagen mit geraden Atomzahl ihre Struktur behalten, wohingegen Filme mit ungerader Anzahl diese nach Desorption verlieren. Darüber hinaus wurden nichtlineare Effekte dritter Ordnung mit diesem experimentellen Aufbau beobachtet und mit den theoretischen Vorhersagen beschrieben.

Contents

List of Figures

LIST OF FIGURES

LIST OF FIGURES

List of Tables

1

Introduction and goals

In this chapter the research subjects of this thesis, i.e. acylated homoserine lactones (AHLs) and self-assembled monolayers (SAMs), will be introduced and the arising scientific questions as well as goals will be discussed. Briefly, AHLs are a subclass of signaling molecules involved in the communication of bacterial biofilms. One question related to these small molecules is whether they are able to integrate into or even penetrate a cellular membrane. However, the study of conglomerates of cells such as biofilms or a thin layer of tissue is already hard as they form complicated biological systems. Even the membrane of a single cell is so complicated that its role in specific processes is hard to study with standard biological techniques such as fluorescence microscopy. In order to answer this question the studied systems have to be simplified dramatically and new paths have to be struck in the study of membrane interacting biological molecules. One way is to form model membrane on a solid support. But to trigger the formation of these lipid bilayers the support has to be functionalized with SAMs having an appropriate end group. To find the ideal candidate for the formation of stable and closed supported lipid bilayers a systematic study of SAMs is important.

1.1 Bacterial biofilms and the role of acylated homoserine lactones

Bacterial biofilms accompany us in our daily life. They do not only form in all kinds of natural habitats such as the deep ocean or deep groundwater, but they also occupy artificial habitats like metallic pipelines or the heat exchangers of power plants. It

is noteable that their insulating properties are eventually so high that the exchange efficiency is decreased by at least 10 % [9][10][11] [12]. Bacterial biofilms even survive the harsh conditions in a nuclear power plant as they can be found in its condenser tubes [13]. They also form in the human body, where they colonize the skin, the gastro-intestinal tract or the oral cavity [14]. There biofilms are also involved in the development of severe, chronic human diseases. Bacterial biofilms cause for example musculoskeletal infections, bacterial prostatitis or dental caries [15]. Unfortunately, they also form on medical implants such as artificial hip joints or cardiac pacemakers necessitating a new surgery including the removal of the implant and the insertion of a fresh one [16]. Another problem accompanying both afore mentioned issues is high resistance of biofilms against antibiotics. This property arises directly from their slimy and dense composition, which makes it hard for antibiotic agents to reach the bacterial cells in an biologically active state [17].

Since biofilms pose such huge problems to either the industry or the human health, their formation is currently a hot topic in microbiology. If a surface offers bacteria the right environmental conditions it triggers the transition from free floating life to life on a surface and a biofilm starts to form on the surface. However, the involved signals vary from bacteria to bacteria and the triggering factors comprise nutritional content as well as temperature, osmolarity, pH, and oxygen. Since the formation procedures are as manifold as the potential triggering signals, in the following paragraph the biofilm formation of *Pseudomonas aeruginosa* will be exemplarily considered in detail.

Pseudomonas aeruginosa is a bacterium involved in the development of e.g. Cystic fibrosis pneumonia (cf. [9]). It was shown that flagellae and type-IV pili play an important role during the attachment of *P. aeruginosa* to the surface. It is remarkable that the bacteria apparently swim across the surface as if scanning for an appropriate location for the initial contact. Once the contact is established the bacteria seem to rest on the surface (see Fig. 1.1, 1). When the bacteria finally form a monolayer they start to move again (Fig. 1.1, 2). However, their movement is somewhat different from the movement prior to the contact with the abiotic surface as they use more their pili in a creeping-like motion. Studies have shown that this motility is only exhibited when they are in contact with other cells which depends on a certain communication between the cells [18]. As a consequence of this twitching motility the bacteria move toward each other and start to form microcolonies which themselves as clusters begin to move

together (also Fig. 1.1, 2). Beginning late in stage 2 and during stage 3 *P. aeruginosa* starts with an augmented production of exopolysaccharides (EPS) forming a dense matrix as shown in Fig. 1.1, 3. This matrix holds the biofilm together and finally leads to the accumulation of also other organisms that use the organic molecules as e.g. nutrients (see Fig. 1.1, 4). In the late stage of biofilm development, planktonic cells start to leave the biofilm according to a specific program that converts a subpopulation of the cells into motile planktonic cells and that leads to the degradation of parts of the EPS (see Fig. 1.1, 5). Also, at a late maturation stage it is even possible that biofilms extend so wide into their aquatic environment, that pure shear forces can ablate parts of the bacteria carrying EPS which therefore leads to a spreading of the biofilm.

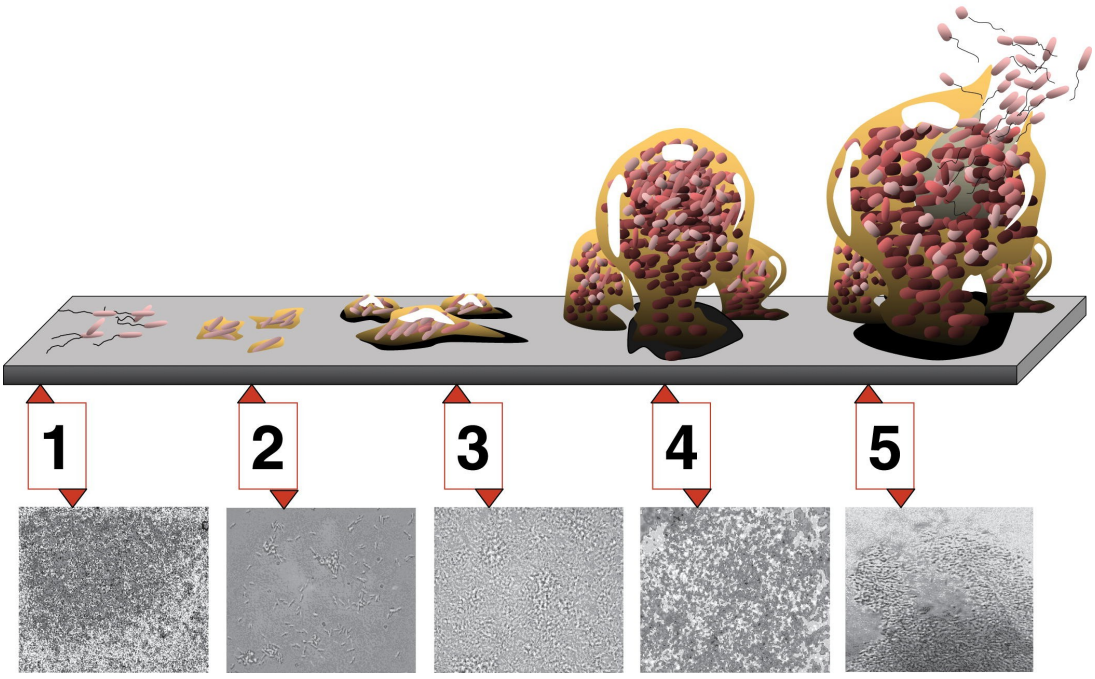

Figure 1.1: Different stages of biofilm formation are depicted here. 1: Bacteria approach the surface and actively search for an appropriate location to settle. 2: Exopolysaccharides are produced to form a dense matrix. 3: EPS holds the biofilm together and also attracts of other organisms. 4: The biofilm extends wide into the environment leading to the potential ablation of the biofilm. 5: Planctonic cells leave the film to find new settlement spots. (Figure from Monroe [1]).

When considering those complicated and concerted processes it is obvious that

they have to be coordinated in a certain way. This is accomplished via direct cell-to-cell signaling which drives for instance the expression of various genes [19]. One class of molecules which has been identified as responsible for the signaling are acylated homoserine lactones or AHLs. As these signaling molecules need a certain population density for gene activation, the term *quorum sensing* has been coined for this type of gene regulation [20].

Recently, several studies have shown that AHL-signaling is not restricted to bacteria, but that these molecules also interact with eukaryotic cells in a phenomenon termed *inter-kingdom signaling* [21]. N-(3-oxododecanoyl)-L-homoserine lactone (3OC12-HSL, see Fig. 1) 1 is the most prominent molecule in this class. Several effects on mammalian cells induced by 3OC12-HSL have been reported, particularly in the context of the immune system [22, 23].

In contrast to adverse effects reported in literature, e.g. down-modulation of defense-relevant functions [24, 25, 26] or induction of apoptosis [27], 3OC12-HSL might also support the host defense by induction of chemotaxis of human polymorphonuclear neutrophils (PMNs) in vitro [28]. These phagocytic cells are known as the first line defense against bacterial infections and their migration into infected sites is crucial for an efficient host defense [22, 23].

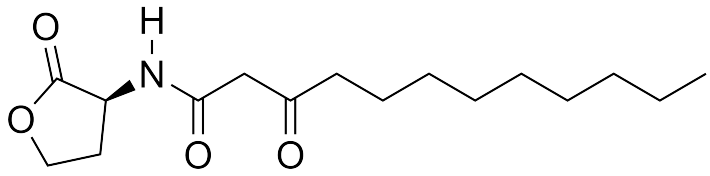

(a) 3OC12-HSL

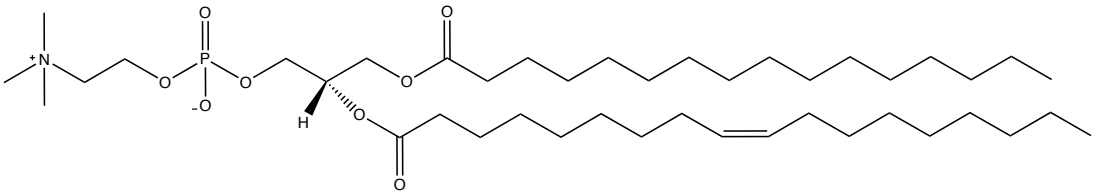

(b) 1-palmitoyl-2-oleoyl-sn-glycero-3-phosphocholine (POPC)

Figure 1.2: (a) depicts the structure of one member of the AHL family (3OC12-HSL), (b) shows exemplarily the phosphoplipid POPC. They both possess a striking amphiphilic similarity allowing AHLs to potentially integrate into and flip through a lipid bilayer.

As yet, little is known about the detailed mechanism of the interaction between AHL and host cells. Since 3OC12-HSL retains intracellular activity [29], an intracellular receptor seems most likely, but an extracellular membrane-bound receptor cannot be excluded. Nevertheless, to interact with intracellular components 3OC12-HSL must cross the cell membrane. Both, a receptor-mediated path or membrane crossing by diffusion are feasible. Figure 1.2 demonstrates the striking similarity between AHL and lipids, the main components of cell membranes. Due to the similarity in amphiphilic character of lipids and AHL, non-receptor mediated diffusion through the cell membrane is reasonable [30].

Thus, the goal of this work is to provide evidence for one of the two theories. Moreover, if indications for a flipping process can be found, orientations of various molecular groups of the acylated homoserine lactones as well as their flipping rate through the membrane will be determined. This will necessitate the implementation of a platform to easily form lipid bilayers and to integrate biological molecules. This system has to be combinable with a suitable technique for the determination of orientation and flipping rate of AHLs. With its high sensitivity and specificity sum-frequency generation (SFG) spectroscopy has proven to be a versatile tool capable to achieve these goals. It has already been extensively used to study adsorbates at various interfaces [31][8][32][33] as well as to follow the flipping process of phospholipids in model membranes [34] and to determine the influence of antimicrobial peptides on lipid bilayers [35]. However, to verify the formation of supported lipid bilayers other techniques such as quartz crystal microbalance with dissipation monitoring (QCM-D) and electrochemistry were employed. In order to reliably study the orientation of acylated homoserine lactones incorporated in lipid bilayers they had to be deuterated leading to a shift of their spectral bands and thus avoiding an overlap with bands emanating from other molecules.

1.2 Self-assembled monolayers

Establishing a system to study supported lipid bilayers i.e. the integration of potentially interacting molecules requires a suitable support. Thus, the use and study of self-assembled monolayers to tailor the substrate's wettability, one determining factor for the formation of lipid bilayers, is essential for the success of SLBs (cf. Lahiri et al.[36]).

Self-assembled monolayers were given their name for the spontaneous adsorption they exhibit upon exposure to a specific substrate. Upon adsorption they also form a single well-ordered quasi-crystalline film [4][37]. The constituents of self-assembled monolayers are organic molecules formed by a chemical functionality bearing a high affinity to a specific surface (Fig. 1.3 *A*). Furthermore, most headgroups are not only exhibiting a high affinity to the surface, but they cleave already adsorbed organic material from the substrate. A couple of headgroups are well-known for their high binding affinity to different materials such as metals, metal oxides or semiconductors. Attached to the headgroup is an aliphatic chain of varying length (Fig. 1.3 *B*). This alkane chain is terminated by a group defining the chemical properties of the monolayer such as wettability or the possibility for further surface chemistry (Fig. 1.3 *C*).

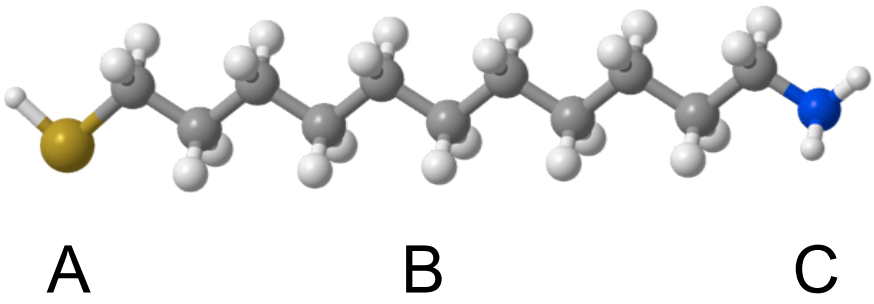

Figure 1.3: Chemical structure of an alkanethiolate exemplarily shown with an amino undecanethiol. *A* marks the headgroup responsible for the attachment to the surface, here a sulfur atom. *B* depicts the aliphatic chain whose length can vary according to the thiol molecule. *C* is the terminal group whose chemical behavior finally tailors the surface properties.

Self-assembled monolayers prepared from alkanethiolates on gold have been studied for more than twenty years with various surface-sensitive techniques such as X-ray photoelectron spectroscopy or infrared reflection absorption spectroscopy [38]. Whereas in the beginning the attention was mainly on a fundamental understanding of the processes happening during the adsorption of the film [33] and their structural determinants [4], in recent years the functionalization of surfaces with various terminal groups was drawn into the focus of research. Functionalizing the organothiols with an appropriate group

opens the possibility of tailoring, for instance, the wettability of the surfaces [2], their affinity for cell attachment [39][40][41] or protein adsorption [42].

1.3 Pyridine-terminated Thiolates

While studying SAMs with different end groups pyridine-terminated thiols, a subclass with interesting electrochemical properties, was examined. The lone pair of nitrogen electrons provided by the pyridine unit can act as a Lewis base. The complexation of palladium salts can for example be accomplished with this functionality which subsequently can be electrochemically reduced to yield metallic Pd particles [43][44]. Pyridine-functionalized surfaces have been shown to promote the electron transfer between electrodes and the solution phase of cytochrome c [45]. Recent studies also revealed that the chemical behavior of those SAMs regarding protonation is rather complicated [46]. In addition, it has been shown that the interaction of pyridine-terminated self-assembled monolayers with water is rather complex. In general, no direct conclusions can be drawn from findings for pyridines in solution [47][48]. Thus, further studies of pyridine-terminated surfaces are needed.

First studies of pyridine-terminated self-assembled monolayers have been conducted in the early 2000s using 4-mercapto-pyridine [44][45][49]. However, it is often a challenge to form a contamination-free and ordered 4-mercaptopyridine monolayer from these components, as this requires special treatments such as adjustment of solution pH and potential-controlled adsorption. In the last years, other pyridine-functionalized thiols or disulfides have been used in order to deepen the knowledge of factors influencing e.g. film quality or the interaction with water. In the present work two pyridine-terminated thiols with backbones formed by both aromatic and aliphatic parts have been studied. These thiols combine the structural and electronic properties of the aromatic chains with the pyridine functionalization of the substrate and offer more easily to handle alternatives to 4-mercaptopyridine monolayers. (4-(4-(4-pyridyl)phenyl)phenyl)methanethiol (PyPP1) consists of a pyridine unit that is subsequently connected to two phenyl rings at the respective 4^{th} carbon atom. Over a methyl unit the last phenyl ring is attached to a thiol binding to the substrate. 2-(4-(4-(4-pyridyl)phenyl)phenyl)ethanethiol (PyPP2) is essentially similar to PyPP1, however, instead of the methylene unit that connects the phenyl and the thiol an ethylene group has been inserted (see Fig. 1.4). In precious

studies it could be shown that the additional carbon atom leads to a tilt of more than 15° with respect to the surface normal [2].

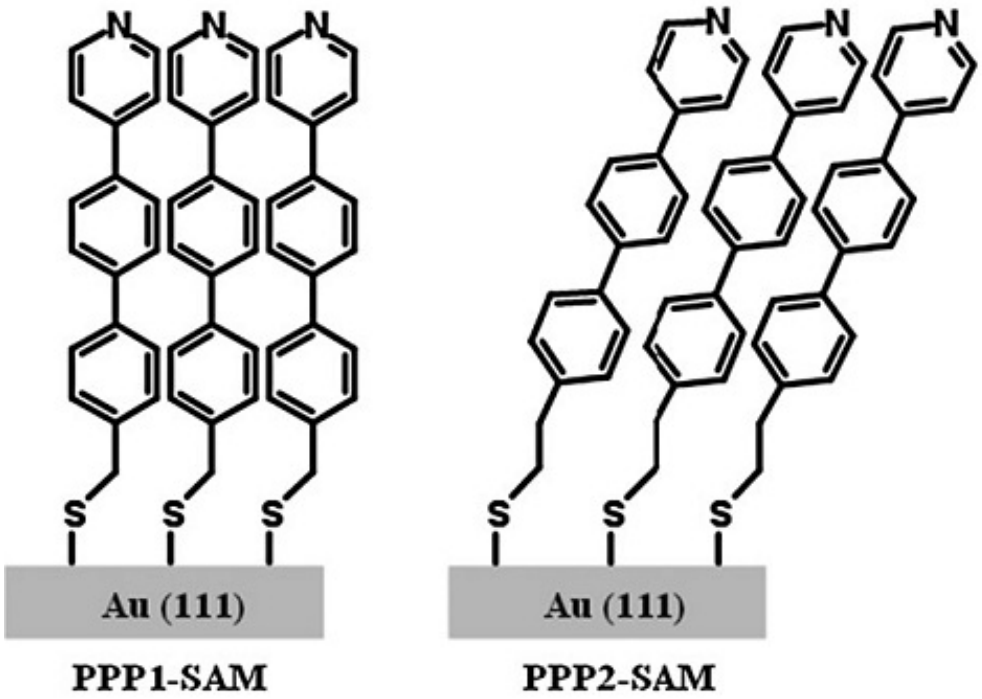

Figure 1.4: This figure depicts the chemical structure of the investigated pyridine-terminated self-assembled monolayers PyPP1 and PyPP2. Clearly visible is that PyPP2 is tilted by an angle of more than 15° with respect to the surface normal caused by the additional ethylene group (Figure from Liu et al. [2]).

First cyclovoltammetric measurements on the two investigated self-assembled monolayers revealed that in agreement with Long et al. [50] the desorption peak potential and the charge densities vary essentially from even to odd numbered methylene spacers. Relating this phenomenon only to the thickness of the investigated monolayer would be an oversimplified answer though. It is more likely that stronger intermolecular interactions influence the desorption and re-adsorption of the odd numbered alkane spacers. However, the verification of this assumption proved to be very hard as it has to be carried out in the electrochemical environment shortly after or parallel to the desorption and re-adsorption. Most of the common surface characterization techniques need a high vacuum and therefore cannot be applied in liquid environment inhibiting the

combination with electrochemical measurements on the monolayers of interest. The high vacuum technique XPS for example provides the researcher only with information about the composition of the examined monolayer and limited detailed information about its structure. In contrast, infrared spectroscopy is a technique enabling the experimenter to observe changes in the structure of the studied molecules, even *in situ*. However, due to the high infrared absorption of water in spectroscopically interesting regions, its sensitivity is strongly decreased and thus it is hard to follow structural changes within thiol monolayers in real-time.

To combine *in situ* electrochemical cylcovoltammetric measurements with highly sensitive measurements on structural changes within the self-assembled monolayer, femtosecond SFG vibrational spectroscopy experiments were conducted in a home-made electrochemical sample cell. This offered the possibility to follow the structural changes of the pyridine-terminated monolayers in real-time and correlate them with phenomena in the recorded cyclovoltammograms. Moreover, the high sum-frequency signals generated from the pyridine group revealed the highly interesting nonlinear optical phenomenon of $\chi^{(3)}$ effects which are related to the additionally applied electric field. This effect has been known since the first theoretical papers on nonlinear optical effects [51][52] and it has also been considered in the first electrochemical SFG experiments [53]. However, detailed considerations of this third order nonlinear optical phenomenon regarding its implications for vibrational bands and moreover its effects in a femtosecond system are still missing. Thus, this experimental setup was used to further investigate influence of the afore mentioned $\chi^{(3)}$ effects on the band shapes and intensities and relate them to predictions made from theory.

2

Materials and Methods

This chapter introduces and discusses all methods as well as the materials used in the course of this work. The first two sections will intensively deal with the theory of SFG spectroscopy and the employed home-built spectrometer. The following sections focus on the production of supported lipid bilayers, the preparation of acylated homoserine lactones and the supporting techniques used for an independent investigation of the studied samples such as FTIR, QCM-D or electrochemistry.

2.1 The theory of sum frequency generation

SFG is a second-order and thus nonlinear optical process. The spectroscopic technique based on it have already been used for the investigation of self-assembled monolayers of various compositions (e.g. [33][40][54]), for the study of air-liquid interfaces with different ionic and molecular solutions [55] as well as with a charged interface [56]. As SFG emerged also other interface phenomena such as protein adsorption [57] or the formation of the extracellular matrix [58]. In recent years the technique was also employed to study supported lipid bilayers and biological or artificial molecules interacting with the bilayers (e.g. [59][60][61]). In this work SFG spectroscopy will be used to drive the knowledge in both fields further. In order to illustrate the nonlinearity of the process, it is helpful to briefly recapitulate the theory of processes that are considered to be optically linear. After a short summary the theory of nonlinear optical processes especially SFG will be discussed. The focus of the last subsection lies on the employed data analysis methods.

2.1.1 Linear optical response

Light or electromagnetic radiation in general interacting with matter causes a distortion of the internal charge distribution within a dielectric. Particularly, the electric field displaces the electron cloud around the nucleus from the equilibrium position and thus a net dipole moment is created. By assuming a harmonic potential for the atom $U(x) = \frac{1}{2}m_e\omega_0^2x^2$ as proposed by H.A. Lorentz the movement of the electron can be modeled with a simple spring system obeying Hooke's law [62][63].

$$m_e(\frac{d^2x}{dt^2} + 2\alpha\frac{dx}{dt} + \omega_0^2x) = -eE_0\cos\omega t \tag{2.1}$$

with the displacement x, the electronic charge e and the electron mass m_e. E_0 is the amplitude of the incident electric field $E(t)$ oscillating at frequency ω. ω_0 is the natural frequency of the undisturbed harmonic oscillator at resonance. α is a damping constant that was introduced as electrons experience strong restoring forces from neighboring atoms and electrons in their vicinity. Thus, an substantial amount of their kinetic energy is dissipated. Eq. 2.1 can be solved with $x(t) = Ae^{i\omega t}$.

$$-A\omega^2e^{-i\omega t} + 2i\alpha A\omega e^{-i\omega t} + \omega_0^2Ae^{-i\omega t} = \frac{-eE_0}{m_e}\cos\omega t \tag{2.2}$$

$$A\cos\omega t = \frac{-eE_0}{m_e(\omega_0^2 - \omega^2 + 2i\alpha\omega)} \tag{2.3}$$

$$x(t) = \frac{-eE_0e^{i\omega t}}{2m_e(\omega_0^2 - \omega^2 + 2i\alpha\omega)} + c.c. \tag{2.4}$$

The dipole moment induced by the incident electromagnetic radiation is defined as

$$\mu = -ex(t) \tag{2.5}$$

With Eq. 2.4 obtained from the previous considerations Eq. 2.5 can be rewritten to

$$\mu = -ex(t) = \frac{e^2E_0e^{i\omega t}}{2m_e(\omega_0^2 - \omega^2 + 2i\alpha\omega)} + c.c. \tag{2.6}$$

In order to measure an effect of the incident electromagnetic field all microscopic dipole moments μ_n can be combined to yield the macroscopic polarization $P = \sum_n \mu_n/V$. Considering the previous results and assuming that the dipole moments μ_n of N electrons per volume V are of the same order of magnitude and direction, the polarization can be written as

$$P = \frac{Ne^2E_0e^{i\omega t}}{2m_eV(\omega_0^2 - \omega^2 + 2i\alpha\omega)} + c.c. \tag{2.7}$$

This equation can also be expressed in a notation similar to classical electrodynamics

$$P = \frac{1}{2}\epsilon_0(\chi E_0 e^{i\omega t} + c.c.) \tag{2.8}$$

with $\chi = \chi(\omega) = \frac{Ne^2}{\epsilon_0 m_e(\omega_0^2 - \omega^2 + 2i\alpha\omega)}$ and the permittivity ϵ_0. From Eq. 2.7 it can be deduced that without any energy dissipation, hence $\alpha = 0$, P is purely real and linearly depending on the applied electric field.

2.1.2 Nonlinear optical processes

However, if the field strength E of the incident electromagnetic radiation exceeds a certain level, the force upon the valence electrons does not linearly depend on the displacement anymore. This is comparable to a physical pendulum where the restoring force only depends linearly on the displacement if this is small. A high field strength, as it is created by high energy pulsed lasers, forces the electrons to leave their equilibrium positions into a region where the linear dependence is not true anymore. Since the restoring force is now nonlinear, Eq. 2.1 has to be extended to

$$m_e(\frac{d^2x}{dt^2} + \omega_0^2 x) - C_2x^2 - C_3x^3 = -eE_0\cos\omega t \tag{2.9}$$

still assuming that the dielectric is not absorbing, hence $\alpha = 0$. In order to find a general formulation for $x(t)$ and thus draw conclusions for $P(t)$ in terms of $E(t)$ a solution for Eq. 2.9 in special cases is helpful. Assuming a case where $C_2 = 0$ and $E(t) = 0$ with initial conditions $x(0) = a$ and $\dot{x} = 0$ the solution is

$$x(t) = a\cos\omega_1 t - (C_3a^2/32m_e\omega)(\cos 3\omega_1 t - \cos\omega_1 t) + \dots \tag{2.10}$$

with $\omega_1^2 = \omega_0^2 - 3a^2C_3/4m_e + \dots$. The natural response of the system remarkably involves a third harmonic term. The electron shall now be driven by an external force e.g. an electric field $E(t) \neq 0$ oscillating at frequency ω. With a first approximation $x_1 = x\cos\omega t$ the exact solution for the differential equation can be determined iteratively. In the next iteration step

$$x_2 = a\cos\omega t - \frac{C_3a^3}{46m_e\omega^2}\cos 3\omega t \tag{2.11}$$

An oscillation at frequency ω forced upon the system will thus be answered with an oscillation at frequencies ω and 3ω. For a cubically nonlinear system, x has contributions of E and E^3 and consequently $P \propto E + E^3$. It can similarly be shown for

$C_2 \neq 0, C_3 = 0$ that a solution to Eq. 2.9 contains only contributions with frequencies ω and 2ω and hence $P \propto E + E^2$. These findings can be generalized to

$$P = \epsilon_0[\chi^{(1)}E + \chi^{(2)}E^2 + \chi^{(3)}E^3 + \dots] \tag{2.12}$$

with the linear susceptibility $\chi^{(1)}$ and the second- and third-order nonlinear susceptibilities $\chi^{(2)}$ and $\chi^{(3)}$.

So far, the polarization P as well as the electric fields E were treated as one-dimensional. In reality this is true only for the least cases. A generalization of Eq. 2.12 is straightforward though and yields.

$$\mathbf{P} = \sum_{i=0}^{\infty} \mathbf{P}^{(i)}(\omega) = \epsilon_0 \sum_{i=0}^{\infty} \chi^{(i)} \otimes \mathbf{E}^i(\omega) \tag{2.13}$$

In the case of SFG the polarization is dominated by the second-order term

$$\mathbf{P}^{(2)}(\omega) = \epsilon_0 \chi^{(2)} : \mathbf{E}^2(\omega) \tag{2.14}$$

with $\chi^{(2)}$ being a tensor of third rank. The combined electric field of two intense laser beams overlapping at an interface can be expressed as the summation of the two respective electric fields oscillating at different frequencies ω_1 and ω_2.

$$\mathbf{E}(\mathbf{r}, t) = \mathbf{E}(\omega_1, t) + \mathbf{E}(\omega_2, t) \tag{2.15}$$

$$= \mathbf{E}(\omega_1)e^{-i\omega_1 t} + \mathbf{E}^*(\omega_1)e^{i\omega_1 t} + \mathbf{E}(\omega_2)e^{-i\omega_2 t} + \mathbf{E}^*(\omega_2)e^{i\omega_2 t} \tag{2.16}$$

Inserting Eq. 2.16 into Eq. 2.14 yields

$$\begin{aligned} \mathbf{P}^{(2)} &= \epsilon_0 \chi^{(2)} : [\mathbf{E}_1^2 e^{-2i\omega_1 t} + \mathbf{E}_2^2 e^{-2i\omega_2 t} + 2\mathbf{E}_1\mathbf{E}_2 e^{-i(\omega_1+\omega_2)t} \\ &+ 2\mathbf{E}_1\mathbf{E}_2^* e^{-i(\omega_1-\omega_2)t} + (\mathbf{E}_1^*)^2 e^{2i\omega_1 t} + (\mathbf{E}_2^*)^2 e^{2i\omega_2 t} \\ &+ 2\mathbf{E}_1^*\mathbf{E}_2^* e^{i(\omega_1+\omega_2)t} + 2\mathbf{E}_1^*\mathbf{E}_2 e^{i(\omega_1-\omega_2)t}] \end{aligned} \tag{2.17}$$

Eq. 2.17 shows that the nonlinear polarization contains several frequency components.

$$\begin{aligned} \mathbf{P}^{(2)}(2\omega_1) &= \epsilon_0 \chi^{(2)} \mathbf{E}_1^2 e^{-2i\omega_1 t} && \text{SHG} \\ \mathbf{P}^{(2)}(2\omega_2) &= \epsilon_0 \chi^{(2)} \mathbf{E}_2^2 e^{-2i\omega_2 t} && \text{SHG} \\ \mathbf{P}^{(2)}(\omega_1 + \omega_2) &= 2\epsilon_0 \chi^{(2)} \mathbf{E}_1\mathbf{E}_2 e^{-i(\omega_1+\omega_2)t} && \text{SFG} \\ \mathbf{P}^{(2)}(\omega_1 - \omega_2) &= 2\epsilon_0 \chi^{(2)} \mathbf{E}_1\mathbf{E}_2^* e^{-i(\omega_1-\omega_2)t} && \text{DFG} \\ \mathbf{y}\mathbf{P}^{(2)}(0) &= 2\epsilon_0 \chi^{(2)} (\mathbf{E}_1\mathbf{E}_1^* + \mathbf{E}_2^*\mathbf{E}_2) && \text{OR} \end{aligned}$$

The nonlinear processes described by the formulae above are second harmonic generation (SHG), sum-frequency generation (SFG), difference-frequency generation (DFG) and optical rectification (OR).[1] Even though, four frequency components are generated by the incident radiation, usually only one of these components is generated at a detectable intensity. For each of these processes an own phase-matching condition has to be fulfilled which in rare cases can only be accomplished for two or more of the components.

Dipoles induced by an external electromagnetic field radiate a field with a typical dipole pattern and its own phase essentially depending on the incident beam. As indicated in the previous paragraph it is possible to generate a sum-frequency beam of substantial intensity only if the relative phase of the induced dipoles is such that their radiation adds up constructively. Thus the two incident light beams have to be spatially and temporally overlapping at the surface. This rule can be expressed in the notation of momentum conservation as

$$\mathbf{k}_{\mathrm{SFG}} = \mathbf{k}_{\mathrm{IR}} + \mathbf{k}_{\mathrm{vis}} \tag{2.18}$$

This equation can be rewritten to incorporate the incident and reflected angles of all three respective beams.

$$n(\omega_{\mathrm{SFG}})\omega_{\mathrm{SFG}} \sin\theta_{\mathrm{SFG}} = n(\omega_{\mathrm{IR}})\omega_{\mathrm{IR}} \sin\theta_{\mathrm{IR}} + n(\omega_{\mathrm{vis}})\omega_{\mathrm{vis}} \sin\theta_{\mathrm{vis}} \tag{2.19}$$

with the refractive index of the medium $n(\omega_i)$ at each frequency ω_i and the incident or reflected angles θ_i of the respective beams i = SFG, IR or vis. This notation is more intuitive for the experimental design as it allows predictions with respect to the expected sum-frequency signal.

2.1.3 The second-order susceptibility $\chi^{(2)}$

As already stated in section 2.1.2 the second-order susceptibility $\chi^{(2)}$ is a third-rank tensor comprising $3^3 = 27$ elements. Thus it is appropriate to write it as

$$\chi^{(2)} = \chi^{(2)}_{jkl} \tag{2.20}$$

[1] Here the complex conjugates have been omitted for clarity.

As well Eq. 2.17 can be rewritten to

$$\begin{aligned} P_j^{(2)} &= \epsilon_0 \sum_{k,l} \chi_{jkl}^{(2)} [E_{1,k}^2 e^{-2i\omega_1 t} + E_{2,l}^2 e^{-2i\omega_2 t} + 2E_{1,k}E_{2,l}e^{-i(\omega_1+\omega_2)t} \\ &+ 2E_{1,k}E_{2,l}^* e^{-i(\omega_1-\omega_2)t} + (E_{1,k}^*)^2 e^{2i\omega_1 t} + (E_{2,l}^*)^2 e^{2i\omega_2 t} \\ &+ 2E_{1,k}^* E_{2,l}^* e^{i(\omega_1+\omega_2)t} + 2E_{1,k}^* E_{2,l} e^{i(\omega_1-\omega_2)t}] \end{aligned} \tag{2.21}$$

where j, k and l extent over the three Cartesian coordinates. Eq. 2.21 can be further reduced to the for this work interesting component of SFG

$$P_j^{(2)} = 2\epsilon_0 \sum_{k,l} \chi_{jkl}^{(2)} E_{1,k}E_{2,l}e^{-i(\omega_1+\omega_2)t} + E_{1,k}^* E_{2,l}^* e^{i(\omega_1+\omega_2)t} \tag{2.22}$$

The extraordinary surface-sensitivity of the SFG directly results from the structure of the second-order susceptibility tensor $\chi^{(2)}$. A centrosymmetric environment implies that $\chi^{(2)}$ has to be invariant under parity transformation $\hat{P} : \mathbf{r} \longrightarrow -\mathbf{r}$.

$$\hat{P}(\chi^{(2)}(\mathbf{r})) = \chi^{(2)}(-\mathbf{r}) \stackrel{!}{=} \chi^{(2)}(\mathbf{r}) \tag{2.23}$$

Moreover, the second-order susceptibility tensor is polar i.e. its components reverse sign upon reversal of the coordinates

$$\chi^{(2)}(\mathbf{r}) = -\chi^{(2)}(-\mathbf{r}) \tag{2.24}$$

Combining these two conditions leads to the following equation which has to be fulfilled

$$\chi^{(2)}(-\mathbf{r}) = -\chi^{(2)}(-\mathbf{r}) \tag{2.25}$$

Obviously, Eq. 2.25 can only be true if $\chi^{(2)}$ is identically zero for all frequencies in the considered medium. Thus SFG is forbidden in a centrosymmetric environment. However, not only highly ordered structures such as crystals or self-assembled monolayers are centrosymmetric, also the bulk phase of liquids or transparent solids such as water or CaF_2 do not contribute to the generation of a sum-frequency signal as they are isotropic, hence centrosymmetric. This makes them invisible in SFG spectroscopy making the technique highly suited for the investigation of interface phenomena. Furthermore, lipid bilayer membranes are a highly ordered and isotropic structure and thus their $\chi^{(2)}$ is vanishing. However, integrated molecules break the inversion symmetry by the distortion of the isotropy and thus affect the overall $\chi^{(2)}$. This allows the generation

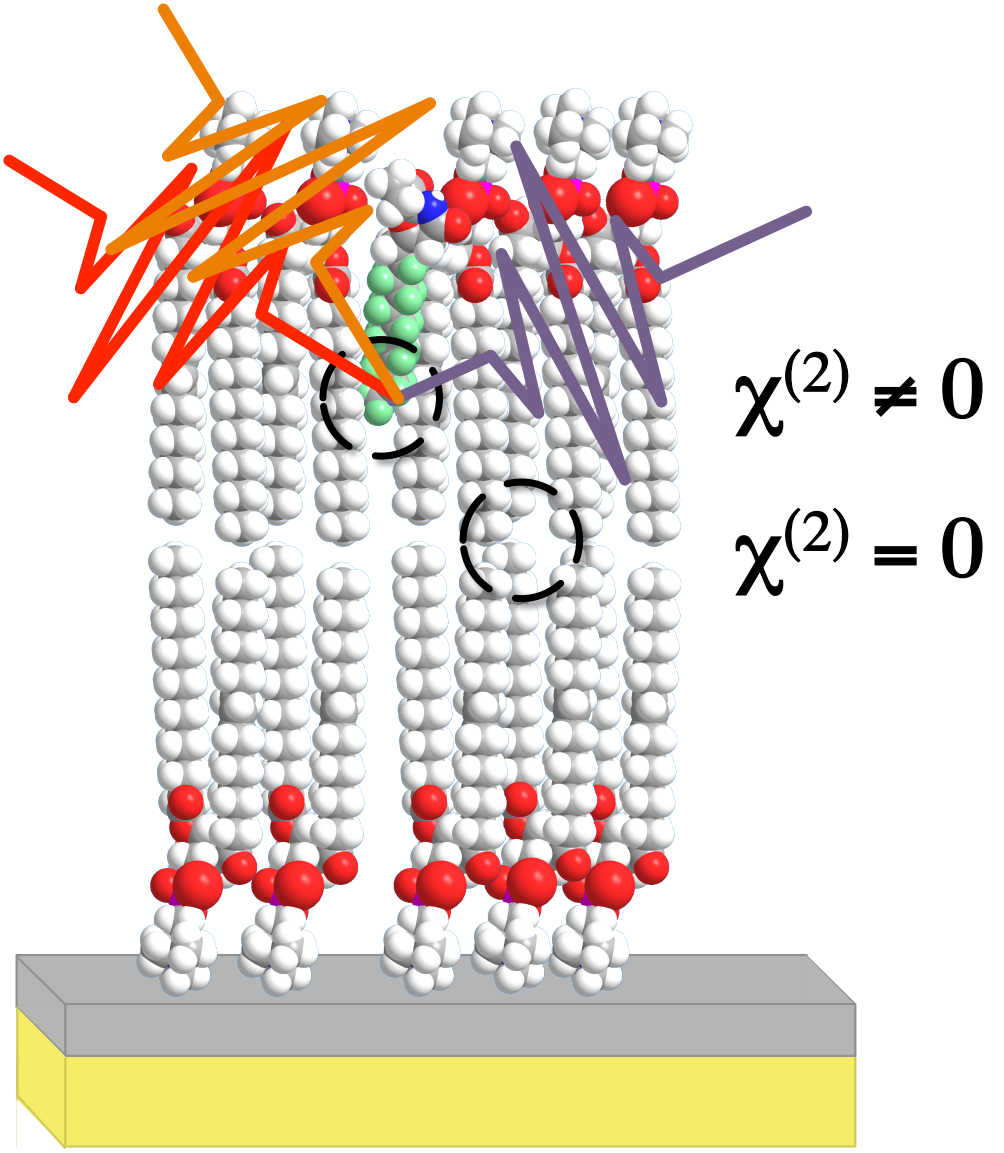

Figure 2.1: Here a typical sample arrangement is shown including from top to bottom the lipid bilayers and an inserted AHL, the hydrophilic 50 nm SiO_2 layer as well as the reflective 200 nm gold layer. The incident infrared and visible laser beams are depicted in red and orange, respectively, whereas the outgoing SFG beam is violet. Due to their isotropy the lipid bilayers do not contribute to the SFG signal. However, an integrated molecule such as an AHL breaks the isotropy and leads to the generation of an SFG signal.

of a sum-frequency signal exclusively from membrane-integrated components (cf. Fig. 2.1).

However, the signals recorded by an SFG spectrometer are not explicitly the generated electric fields $\mathbf{E}_{\mathrm{SFG}}$. It is rather the intensity that is recorded and that is defined as

$$I_{\mathrm{SFG}}(\omega_1+\omega_2) \propto \left|\mathbf{P}^{(2)}\right|^2 = \left|\epsilon_0 \chi^{(2)} : \mathbf{E}_{\mathrm{vis}}(\mathbf{r},t)\mathbf{E}_{\mathrm{IR}}(\mathbf{r},t)\right|^2 \tag{2.26}$$

Therefore the intensity of the produced sum-frequency beam is proportional to the two incident beams, scaled with the second-order susceptibility

$$I_{\mathrm{SFG}}(\omega_1+\omega_2) \propto \left|\chi^{(2)}\right|^2 I_{\mathrm{vis}} I_{\mathrm{IR}} \tag{2.27}$$

Hence the spectroscopically resolved shape of the acquired signal intensity depends essentially on the structure of $\chi^{(2)}$ and the incident visible and infrared beam intensities. If the probed sample furthermore exhibits a C_∞ symmetry, it is invariant under arbitrary rotations around z-axis defined as the surface normal. Considerations for x and y similar to Eq. 2.25 show in this case that $\chi^{(2)}$ is reduced to seven nonzero elements. With correctly polarized beams it is now possible to probe only specific elements of the tensor. An overview of the possible experimental geometries is given in Tab. 2.1. Where not indicated differently, the spectra in this work were recorded in ppp combination. As the shape of the recorded SFG signal plays a key role in the processing of the spectra and determines the exact analytical steps, it will be considered in the next section 2.1.4.

Polarization combination	**Probed tensor elements**
pss	$\chi^{(2)}_{zyy}$
sps	$\chi^{(2)}_{yzy}$
ssp	$\chi^{(2)}_{yyz}$
ppp	$\chi^{(2)}_{zzz}, \chi^{(2)}_{zzx}, \chi^{(2)}_{xzx}, \chi^{(2)}_{xxz}$

Table 2.1: Probed $\chi^{(2)}$ tensor elements in a C_∞ symmetry with respect to the used polarization combination for sum-frequency, visible and IR beam.

2.1.4 SFG spectrum and data analysis

As stated at the end of the previous section the SFG signal is, according to Eq. 2.27, depending on $\chi^{(2)}$ and the intensities of the two incident beams. In the performed experiments the intensity of the visible laser light can be considered as constant over the investigated range of frequencies. However, the infrared beam possesses a Gaussian-shaped profile which must be taken into account when the strengths of the analyzed SFG-active bands are compared. Furthermore, for the performed measurements, the second-order susceptibility tensor consists of two different parts

$$\chi^{(2)} = \chi^{(2)}_{\mathrm{NR}} + \chi^{(2)}_{\mathrm{R}} \tag{2.28}$$

where $\chi^{(2)}_{\mathrm{NR}}$ is a nonresonant contribution generated by electronic transitions between electronic bands in the gold substrate and $\chi^{(2)}_{\mathrm{R}}$ is a contribution due to resonant vibrational modes [64]. As the electronic transitions involved do in principal not change with IR frequency, $\chi^{(2)}_{\mathrm{NR}}$ can be considered as constant and the nonresonant background signal from the gold substrate is purely Gaussian-shaped as it is generated by the Gaussian infrared beam profile. To obtain the lineshape of the resonant sum-frequency contributions the microscopic origin of $\chi^{(2)}_{\mathrm{R}}$ has to be examined in detail. A general expression for $\chi^{(2)}_{\mathrm{R}}$ can be derived with second-order perturbation theory as an infinite sum over all quantum mechanical states of the investigated system [65][32].

$$\chi^{(2)}_{\mathrm{R}} \propto \sum_{s,q} \left[\frac{\langle g|\,\mu_l\,|s\rangle\,\langle s|\,\mu_m\,|v\rangle}{\hbar(\omega_{\mathrm{sum}} - \omega_{sg})} - \frac{\langle g|\,\mu_m\,|s\rangle\,\langle s|\,\mu_l\,|v\rangle}{\hbar(\omega_{\mathrm{vis}} + \omega_{sg})} \right] \times \frac{\langle v|\,\mu_n\,|g\rangle}{\omega_{\mathrm{IR}} - \omega_q + i\Gamma_q} \tag{2.29}$$

where l, m, n represent all three cartesian coordinates, $|g\rangle$ is the ground state, $|v\rangle$ the excited state of the q-th vibrational mode and $|s\rangle$ any other state and ω_{sg} the frequency related to the transition from $|g\rangle$ to $|s\rangle$. In spite of its complicated appearance, Eq. 2.29 possesses a rather simple interpretation. The first term (in brackets) is the quantum mechanial representation of the Raman transition moment, whereas the second term represents the IR transition moment. This nicely illustrates that a vibration is only SFG-active if it is both Raman- and IR-active. Moreover, Eq. 2.29 also shows that such a SFG-active band is resonantly enhanced. When $\omega_{\mathrm{IR}} \approx \omega_q$, the frequency of the resonant band, the denominator of the last term approaches 0 and in turn $\chi^{(2)}_{\mathrm{R}}$ increases dramatically resulting in a resonant enhancement. A diagrammatic representation of the energy levels in the SFG process is depicted in Fig. 2.2. The infrared light ω_{IR}

excites a molecular vibration $|v\rangle$. This state is then up-converted to a virtual level $|s\rangle$ by the visible light ω_{vis} before a photon carrying the sum of the incident energy $\omega_{\text{SFG}} = \omega_{\text{vis}} + \omega_{\text{IR}}$ is emitted in an anti-Stokes process. This brings the system back to its ground state $|g\rangle$.

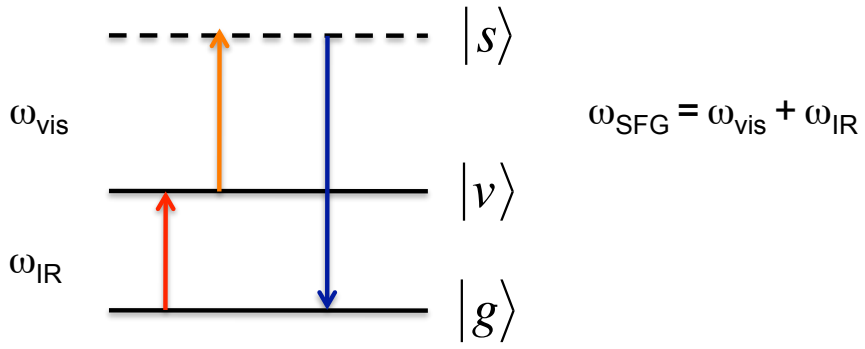

Figure 2.2: Energy level diagram of the SFG process: The infrared beam excites the atom from its ground state to an elevated vibrational state. The visible beam excites the atom further to a virtual state that is destroyed in an anti-Stokes process by the emission of a sum-frequency photon.

Equation 2.29 can be rewritten to

$$\chi_{\text{R}}^{(2)} \propto \sum_q \frac{A_q}{\omega_{\text{IR}} - \omega_q + i\Gamma_q} = \sum_q \left| \frac{A_q}{\omega_{\text{IR}} - \omega_q + i\Gamma_q} \right| e^{i\phi_q} \tag{2.30}$$

where A_q is a measure of the signal strength and ϕ_q the phase of the q-th vibrational mode. Introducing $\chi_{\text{NR}}^{(2)} = \left|\chi_{\text{NR}}^{(2)}\right| e^{i\psi}$ while inserting Eq. 2.30 into Eq. 2.28 and combining the result with the expression for the SFG intensity 2.27 yields

$$I_{\text{SFG}} \propto \left| \left|\chi_{\text{NR}}^{(2)}\right| + \sum_q \left| \frac{A_q}{\omega_{\text{IR}} - \omega_q + i\Gamma_q} \right| e^{i\Delta_q} \right|^2 I_{\text{vis}} I_{\text{IR}} \tag{2.31}$$

with Δ_q being the phase difference of the nonresonant SFG contribution and the resonant responses of the system. This phase difference plays a crucial role in the analysis of sum-frequency spectra. Bain et al. could already show in 1993 that the phase difference indicates the orientation of the transition dipole moment of molecular vibrations with respect to the surface [66]. For the methyl vibrations, for instance, a change of the phase difference of π implies a change from a vibration directed away from the surface to an orientation towards the gold surface.

With all previous considerations in mind an accurate analysis of the recorded SFG spectra has to involve the following steps. A raw spectrum consists of the convolution of Lorentzian-like functions and the Gaussian-shaped infrared intensity. Hence the shape of the spectrum strongly depends on the phase difference Δ_q between resonant and nonresonant susceptibility. The SFG-active bands might appear as a dip or peak. However, a simple inspection of the raw spectrum might lead to false conclusions with regard to the phase difference and thus the orientation of the functional groups. Also, the variable intensity of the infrared beam has to considered. To accurately work out peak positions, intensities and phases it is inevitable to perform a peak fitting on the raw spectra. To accomplish this task an appropriate fitting function using a Levenberg-Marquardt algorithm was written in Origin® (OriginLab) implementing Eq. 2.31 with a Gaussian function for I_{IR} and assuming constant values for $\chi^{(2)}_{\mathrm{NR}}$ and I_{vis}. Thus it is possible to remove the nonresonant background to obtain purely contributions from resonant vibrations. But there is a point that has to be considered in this procedure. The determination of the parameters for the Gaussian function (position ω_G, width w_G and area A_G) does not pose a big problem as this is a strong contribution. However, especially ω_q and Δ_q are strongly correlated making the determination of unique values impossible. Therefore, one of the two variables should be known a priori and kept constant for this routine. The identification of the phase difference of a vibrational mode is rather complicated. But the following paragraph describes a simple way to determine the exact spectral position of a SFG-active band with the SFG spectrometer used in this work.

Lagutchev et al. showed in 2007 that it is possible to suppress the nonresonant background of the substrate while keeping resonant molecular contributions [67]. The nonresonant electronic sum-frequency response of the metal substrate has a shorter life time than the molecular vibrations induced by the IR beam. Thus reducing the temporal overlap from its ideal position decreases the nonresonant signal. At the same time also the amplitude of resonant bands declines. But when the electronic signal has already decayed a resonant sum-frequency signal can still be detected. Fig. 2.3 depicts a delay shift series from 0 fs to 833 fs for a strong pyridine-related band in the amide region. Here, 0 fs correspond to a temporal superposition of infrared and visible beam maximizing resonant and nonresonant contributions. With the method described by Lagutchev the phase information is lost which makes conclusions on the

molecular orientation difficult. However, the position and width determined with the delay-shifted spectrum can be used as input parameters for the fitting procedure which help to calculate phases and amplitudes from the raw spectra. An overview of the whole analysis process including raw spectra, background-suppressed spectra as well as calculated spectra and values is given in Fig. 2.4.

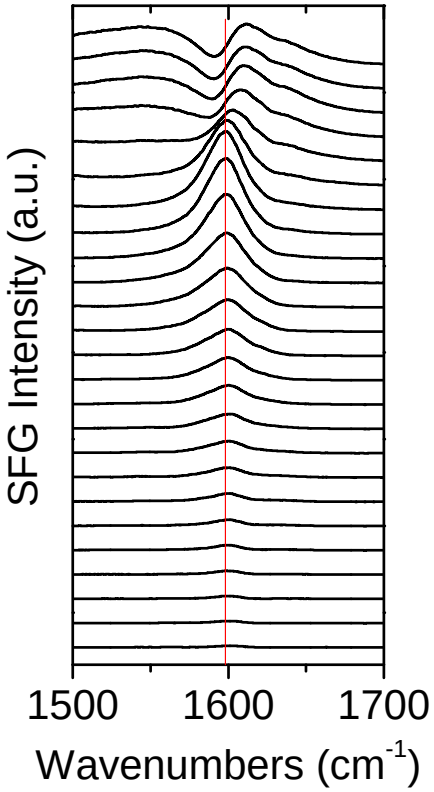

Figure 2.3: This figure depicts the course of a typical SFG-active band with a successively reduced temporal overlap. The shown overlap reaches from 0 fs to 833 fs.

2.2 The SFG spectrometer and the employed sample cell

Since for the generation of higher-order polarization components including second-order sum-frequency signals a high laser power is necessary and pulsed lasers are usually used [54]. A sufficiently high energy density is obtained with picosecond or femtosecond laser systems. However, ps-based systems have the drawback that the data acquisition time is in the order of tens of minutes. Furthermore, the bandwidth scanned during

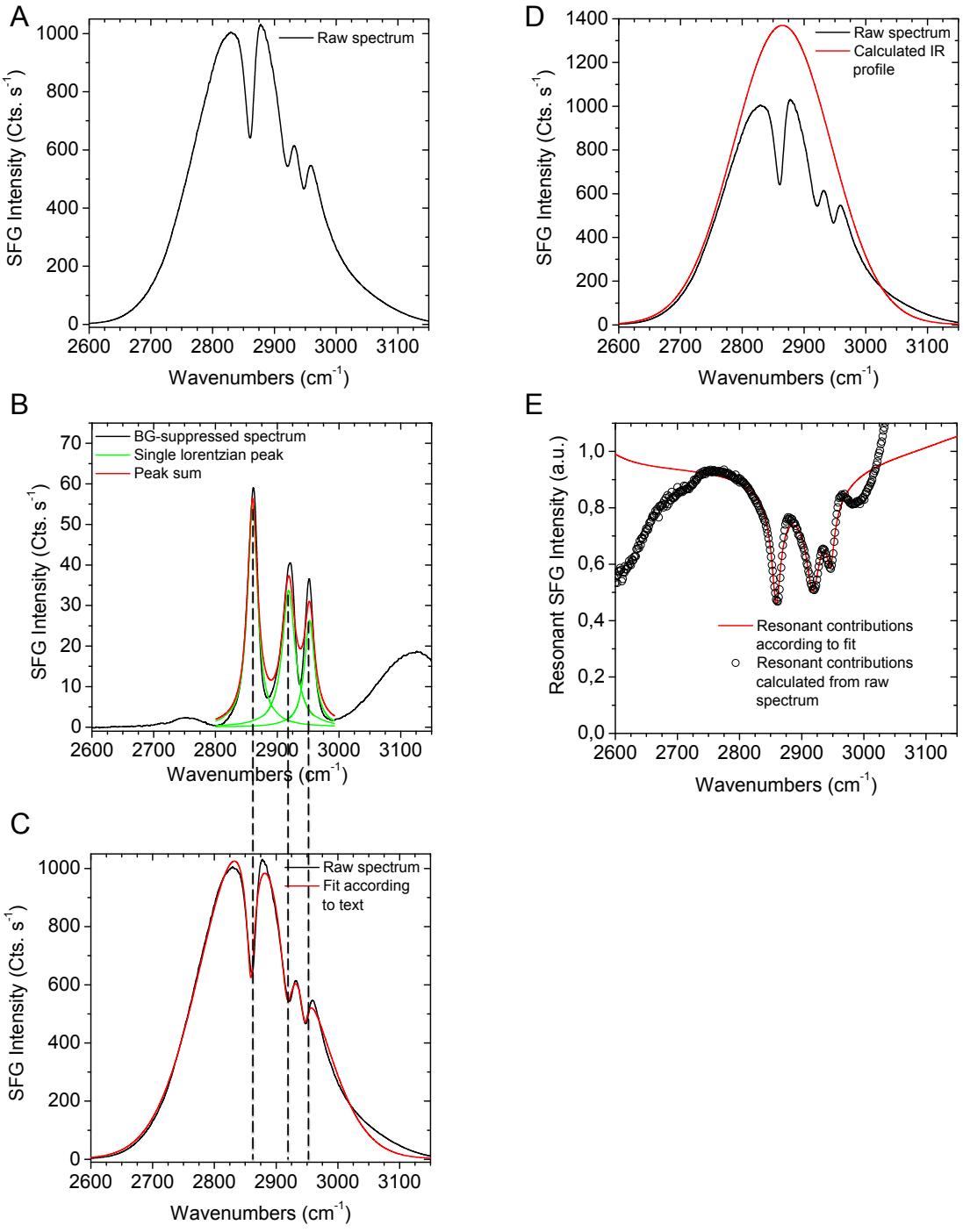

Figure 2.4: A depicts a raw SFG spectrum, for convenience normalized to counts per second. In B the corresponding background-suppressed spectrum is shown. Green and red curves represent fits with Lorentzian functions with fixed line width to obtain exact band positions. In C those positions are used to calculate the fit from the raw spectrum (in red & black, respectively). In D the calculated IR beam profile is shown together with the raw spectrum. It is then divided by the IR profile. The result is depicted in E (open circles). To demonstrate the quality of the fit the calculated resonant contributions from C are shown as a red line.

one measurement is highly limited due to Heisenberg's uncertainty principle [68]. In standard ps-measurements the IR beam is tuned to one specific frequency and the SF signal intensity is acquired for several minutes. Then, the IR laser is moved to the next frequency of interest. This protocol makes the whole measurement process very slow and time-dependent measurements over a broad range of frequencies cannot be performed simultaneously. In contrast, fs-based systems have the ability to cover a broad spectrum of about 100 to 250 cm^{-1}. Thus, dynamic processes can be followed in real-time and over a broad spectral range.

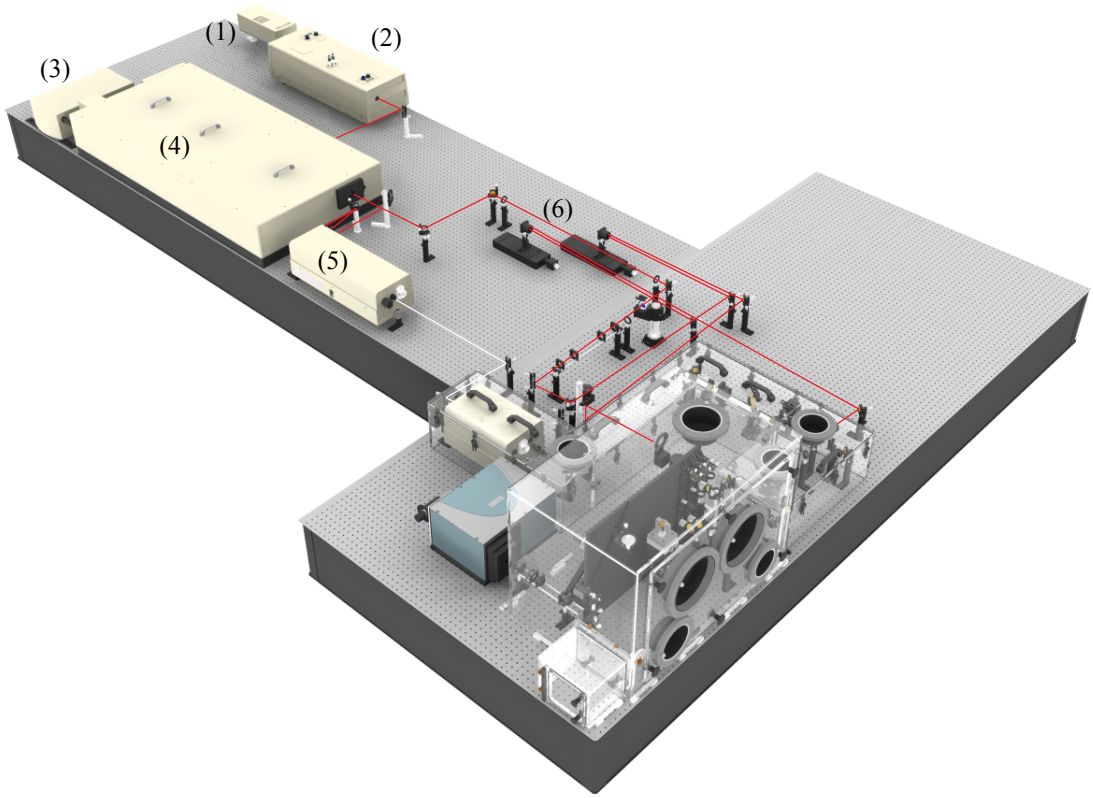

Figure 2.5: The SFG spectrometer setup. The indicated components are the pump laser (1) for the seed laser (2), the pump laser (3) for the regenerative amplifier (4), the optical parametric amplifier (5) and the delay line (6) [3].

The SFG spectrometer employed in the present work is based on the broadband scheme and located in a clean room hood to maintain a constant humidity and temperature (RH $\leq 40\%$ and $= 22 \pm 0.5°$ C) [3]. An overview over the whole setup can be seen in Fig. 2.5. It consists of a fs Ti:Sa regenerative amplifier (RGA) (Spitfire Pro 35F

XP, Spectra-Physics, Germany) that is seeded by a mode-locked Ti:Sa laser centered at 800 nm wavelength and approximately 40 nm bandwidth (Tsunami, 3941-MS, Spectra-Physics). The RGA is pumped by a Q-switched Nd:YLF laser with 1 kHz repetition rate and delivers 6 mJ per pulse (Empower 30, Spectra-Physics, 30 W, 1 kHz), whereas the seeding laser is pumped by a Nd:YVO_4 (Millenia Pro 5s, Spectra-Physics, 5 W). The amplifier generates pulses of 800 nm wavelength with a bandwidth of about 120 fs at a repition rate of 1 kHz. During the measurements an average power of 4 W was achieved. The RGA output beam is split into two parts with a ratio of 80:20. The larger fraction pumps an electrically automated optical parametric amplifier (OPA) (TOPAS-C, Light Conversion, Lithuania). The signal and idler output beams of the OPA seed a similarly automated noncollinear difference-frequency generator (NDFG) to produce broadband infrared pulses with a FWHM of 70 to 200 cm^{-1}. The IR pulses are tunable from 2.6 to 12 μm. Signal and idler beams also leaving the NDFG are initially spacially separated and then filtered by a germanium plate (Crystec, Germany). The smaller fraction of the amplified 800 nm beam ($\sim$ 20%) is directed through several optics and fed into an air-spaced Fabry-Perot etalon (SLS Optics, UK) to reduce the bandwidth of the original pulses to a FWHM of about 1 nm. After being focused in a telescope the beam is directed through an automated delay line allowing for the exact adjustment of the temporal overlap of IR and visible beams thus maximizing the acquired sum-frequency signal. The maxima of the obtainable energies were $\sim 20\mu$J/pulse for the IR beam and $\sim 25\mu$J/pulse for the visible beam. However, in order to prevent the sample or the used CaF_2 prism from damage the infrared and visible energies were for the investigation of AHL integration into lipid bilayers with pinholes reduced to equally 4 μJ/pulse.

The sample stage is mounted to a vertically aligned breadboard restricting the beam paths to the same plain (cf Fig. 2.5). The stage itself consists of a rolling block with micrometer screws and goniometer. Thus, it can be moved in X, Y and Z directions and the incident angles can be changed without changing mirror positions. The incident visible beam is focused onto the sample through a BK7 lens while the infrared beam is focused by a curved mirror. The generated sum-frequency signal is directed with several mirrors through a telescope to be collimated. After being dispersed in an imaging spectrograph (Shamrock SR-301i-B, Andor Technology) the SF beam is directed onto a water-cooled CCD chip. With full energy a spectrum with optimal signal-to-noise

ratio can be acquired within seconds. However, decreasing the energy as previously indicated results in an increase of measurement time to up to 80 s depending on the sample.

The NDFG stage, the whole IR beam path as well as the previously described sample stage are incorporated in a home-built purging chamber to remove ambient water vapor and hence prevent IR beam absorption. The air is cleaned from the gaseous H_2O with two FTIR purging gas generators (75-45-12 VDC, Parker-Balston, Germany). This allows measurements in the amide region at around 1600 cm^{-1} which would be otherwise not accessible due to water vapor absorption.

All experiments were performed with the Thin Layer Analysis cell (TLA) designed by Volker Kurz [3]. It is based on the cell from Skoda et al. [69] which was developd for IR spectroscopy measurements of self-assembled monolayers in liquid. A scheme of the TLA cell as well as a photograph are shown in Fig. 2.6. It consists of a Teflon® base containing a heating/cooling water flow system with meandering pattern. An aluminium block provides the required stability and houses the Teflon® prism adapter. The principal component of the cell is a hemispherical prism made of IR transparent calcium fluoride with optically polished curved and basal surfaces (Crystec, 13 × 20 mm). The prism guides infrared and visible laser beams onto the sample. Moreover, with the help of a threaded rod, it is possible to adjust the thickness of the probed liquid layer and hence reduce energy absorption due to liquid vibrational modes. In addition, the curved surface of the prism minimizes intensity losses due to reflection. In the experiments performed in liquid the sample was covered with an adequate amount of liquid. Subsequently, the prism was placed on top of the sample and fixed with the rod. In experiments including lipid bilayers, the prism was positioned on top of the QCM-D crystal in the liquid phase (cf. Sec. 2.3). Due to adhesion forces the prism could then be moved to the TLA cell without air touching the crystal surface. To prevent the bilayers from damage the prism was just loosely fixed with the rod. For the time-series experiments performed to determine the flipping process of AHL through lipid bilayers a high stability of IR and visible laser intensity is necessary. To ensure this stability these experiments were started after the laser system has been allowed to stabilize for at least 3 hrs.

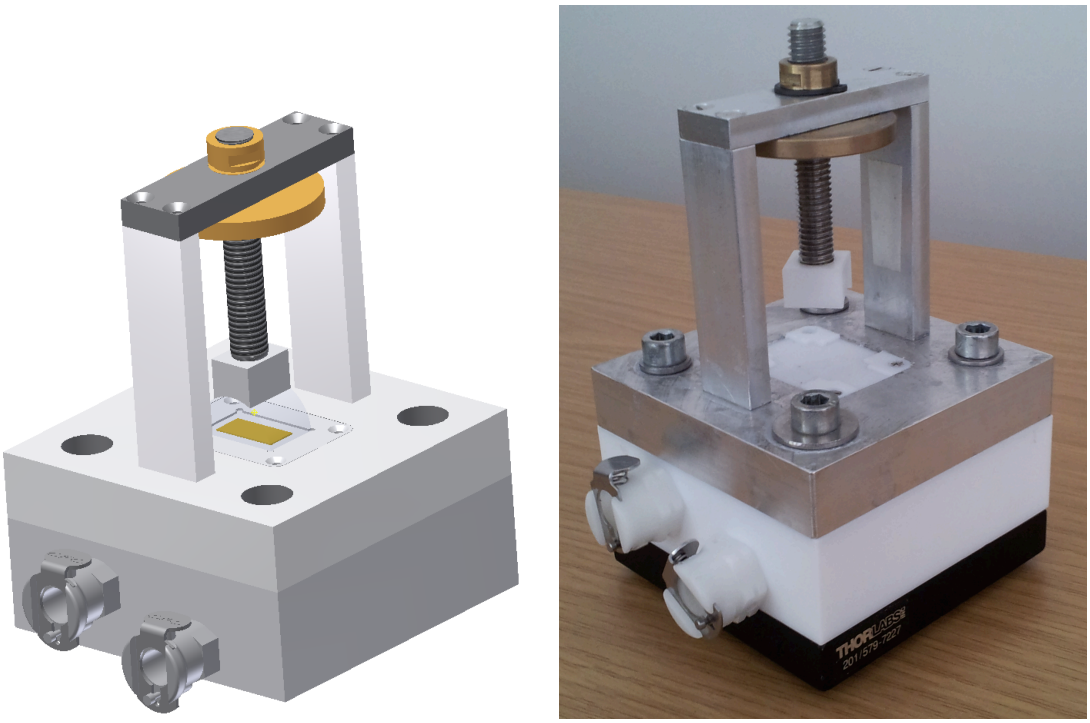

(a) Scheme of the TLA cell

(b) Photograph of the TLA cell

Figure 2.6: (a) shows a scheme of the TLA cell designed for the investigation of thin films *in situ* with all relevant parts. For convenience screws have been removed. (b) shows a photo of the respective cell.

2.2.1 Combined SFG and electrochemical measurements

Simultaneous cyclovoltametric and SFG experiments have been achieved with a TLA cell modified as follows. The gold substrates usually limited to a size as big as the prism were enlarged so that they extended over the larger side of the CaF_2 prism. The working electrode was connected to the gold from one side of the prism. On the other side the film was scratched just next to the prism in order to connect both the counter electrode and the reference electrode. Thin gold wires were used to connect the respective sides of the gold substrates to the cables leading to the potentiostat COMPACTSTAT.e (Ivium, Eindhoven, Netherlands). The gold wires were pressed down on the gold with glass capillaries fixed at the sides of the CaF_2 prism. A Ag/AgCl microreference electrode built by Mutlu I. Muglali from the Max-Planck Institute for Iron Research acted as reference electrode which was also fixed at the sides of the prism. The electrolyte 0.1 M NaOH (at pH 13) was stored in pools built at both sides from X60 two-component adhesive (HBM, Germany). The previously described glass capillaries also stored parts of the electrolyte and released it during the measurements while the rest of the electrolyte evaporated due to constant purging with dry air. Between different experiments the electrolyte was refilled. In order to suppress any leakage current metallic parts of the TLA cell which might get in contact with electrolyte were sealed with standard laboratory tape. A photograph of the modified TLA cell is shown in Fig. 2.7.

After the assembly of the electrochemical SFG cell, measurements began immediately. However, prior to starting the combined SFG and electrochemical measurements a cyclovoltammogram was recorded at a peak voltage of -300 mV which is lower than the known desorption potential of -1600 mV. After the functionality of the voltammetry had been checked the recording of a series of spectra with an exposure time of 0.4 s in the background-suppressed mode was started; after 10 recorded spectra the potential was turned on varying from 0 to -1600 mV with a scan rate of 50 mV/s as displayed in Fig. 2.8. In addition to the recordings in the background-suppressed mode the behavior of the nonresonant signal with a varying electric field was also studied. Spectra of pure nonresonant background were recorded at 2900 cm^{-1}.

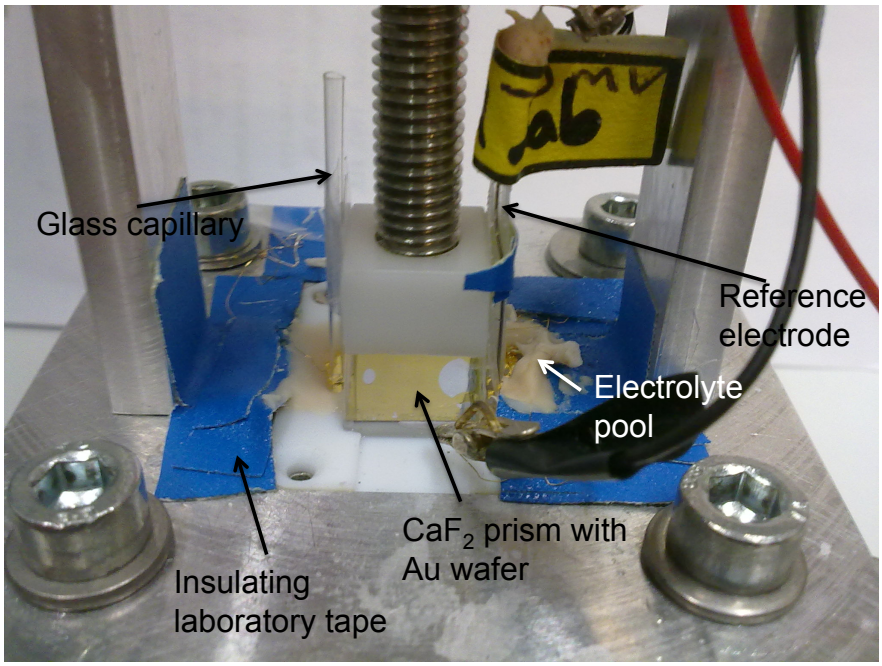

Figure 2.7: This photograph depicts the modified TLA cell. Next to the prism the whitish X60 epoxy as well as the glass capillaries fixing the gold wires can be seen. The reference electrode is marked with yellow flag. The blue tape prevents leakage current from disturbing the measurements.

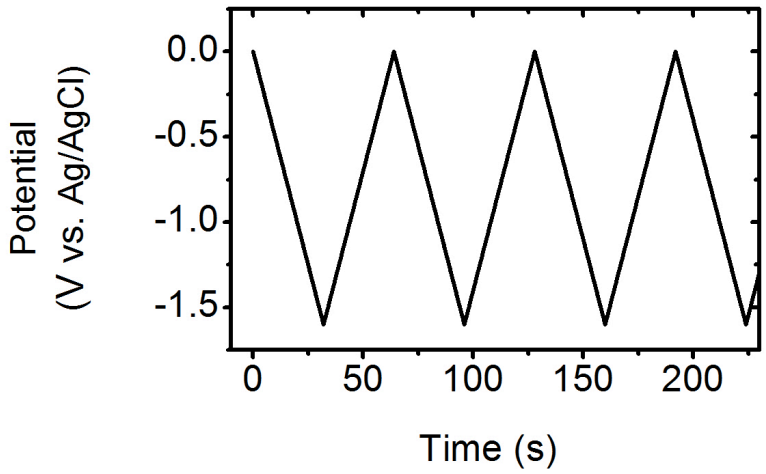

Figure 2.8: Course of the applied potential during the electrochemical SFG experiments.

2.3 Lipid bilayer production

To study the integration of AHL a well-defined lipid bilayer is essential. In principle, there are two ways to produce such supported lipid bilayers. The first is the Langmuir-Blodgett/Langmuir-Schaeffer method. In this method a monolayer spread out in a Langmuir trough at the air/water interface is compressed at a constant surface pressure of 32 - 36 mN/m and then transferred to a hydrophilic support. Subsequently, a second monolayer is added at the same pressure corresponding to the bilayer equivalence pressure [70]. This method is known to produce high quality bilayers [71, 72]. However, for potential future applications such as the integration of membrane spanning proteins this method is inadequate. In contrast, lipid bilayer production via vesicle fusion is dedicated for this task, as the vesicles may also include reconstituted membrane proteins such as ion channels [73]. In order to induce the fusion of vesicles the liposomes have to be very small i.e. their diameter has to be below or near 100 nm. Furthermore, the fusion is induced by the presence of divalent ions such as Ca^{2+}[74].

For the study of AHL integration different lipid composition have been tested including 1-palmitoyl-2-oleoyl-sn-glycero-3-phosphoethanolamine (POPE), 1-palmitoyl-2-oleoyl-sn-glycero-3-phospho-(1'-rac-glycerol) (POPG) and 1-palmitoyl-2-oleoyl-sn-glycero-3-phosphocholine (POPC). Eventually, an established and well-studied phospholipid mixture was chosen for the preparation of the model membranes (cf. [75, 76, 77]). POPC and POPG were mixed in a 1:1 weight ratio. Both pospholipids comprise two aliphatic chains containing 16 and 18 single carbon bonds, respectively. Each of the 18 C aliphatic chains contains additionally one carbon double bond at the 9th position as displayed in Figs. 2.9(a) and 2.9(b). However, POPC is terminated by a choline, whereas POPG possesses a glycerol as terminal group. Thus POPG is negatively charged, whereas POPC is an uncharged lipid. Both phospholipids were purchased from Avanti Polar Lipids Inc. solved in chloroform at a concentration of 25 mg/mL and used without further purification. To simplify the mixing procedures the lipid concentration was adjusted to 10 mg/mL with chloroform purchased from Sigma-Aldrich Co. LLC at CHROMASOLV® Plus quality.

All employed glass ware was thoroughly rinsed twice with absolute ethanol (from Sigma-Aldrich Co. LLC, at CHROMASOLV® Plus quality). To guarantee a complete removal of all organic traces the glass ware was subsequently flushed with chloroform.

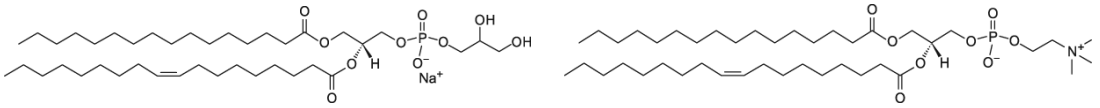

(a) 1-palmitoyl-2-oleoyl-sn-glycero-3-phospho-(1'-rac-glycerol) (POPG)

(b) 1-palmitoyl-2-oleoyl-sn-glycero-3-phosphocholine (POPC)

Figure 2.9: Chemical structure of the two phospholipids used for the preparation of supported lipid bilayers.

It was then blown dry with gaseous nitrogen and sealed with parafilm until further usage. Directly prior to usage, it was once more rinsed with chloroform and blown dry again. Appropriate amounts of lipids solved in chloroform were mixed in a glass vial to obtain a final lipid mass of 2.5 mg. By evaporating the chloroform with a gentle stream of nitrogen the dissolved lipids formed a film on the glass walls. Constantly turning the vial ensured that the lipid film was as thin as possible. After all visible traces of chloroform had been evaporated the vials were put into a desiccator under constant vacuum drain to ensure that the produced lipid film was solvent-free.

After at least two hours the glass vials were taken out of the desiccator and the lipid film was rehydrated under constant vortexing with Tris buffer to obtain a lipid concentration of 2.5 mg/mL. In agreement with Andersson et al. the buffer comprised 100 mM NaCl and 10 mM tris(hydroxymethyl)aminomethane (Tris). The pH was adjusted to 8 with hydrochloric acid (HCl) [78]. The resulting solution containing multilamellar vesicles (MLV) showed an opaque nature indicating the rather high vesicle size of several hundreds nanometers due to a high scattering rate of the incident light (see Fig. 2.11(a)). To finally obtain small unilamellar vesicles necessary for the formation of high quality supported lipid bilayers MLVs were extruded through polycarbonate membranes with 100 nm pore size using a commercially available extruder (Miniextruder, Avanti Polar Lipids Inc., Fig. 2.10). According to Briand et al. the vesicles were extruded at least 11 times through the membranes in order to obtain SUVs with a size close to 100 nm (see section 3.1) [79]. The resulting suspension appeared clear indicating that the vesicle size is no longer of the same order of magnitude as the wavelength of the incident light which prevents its scattering (Fig. 2.11(b)).

Depending on the substrate two different procedures for the formation of supported lipid bilayers were followed. For bilayers formed on silicon dioxide coated QCM-D crys-

Figure 2.10: This manually operated extruder was used for the production of small unilamellar vesicles of about 100 nm size.

(a) Opaque look of the MLV solution.

(b) Clear look of the SUV suspension after being extruded through membranes with 100 nm pore size

Figure 2.11: These figures illustrate the visual appearance of the lipid vesicle suspension before (a) and after extrusion (b)

tals the SUV suspension was diluted to 0.1 mg/mL using a Ca/Tris buffer comprising 100 mM NaCl, 10 mM Tris and 10 mM $CaCl_2$. The divalent Ca^{2+} ions promote the rupture and fusion of lipid vesicles and thus the formation of supported lipid bilayers on the SiO_2 substrate [80]. The SiO_2-coated QCM-D crystals were cleaned from any detergent or adherent organic material by immersing them in 10 mM sodium dodecyl sulfate (SDS) for 10 mins and rinsing them with copious amounts of distilled water. Subsequently crystals were flushed with ethanol and dried with gaseous nitrogen. Directly prior to bilayer formation crystals were cleaned in a UV/ozone cleaner for 30 mins on the one hand to remove remaining organic traces and on the other hand to render the SiO_2 hydrophilic. After the ozone treatment crystals were directly transferred to a small petri dish containing enough Ca/Tris buffer to cover the crystal and thus preventing the contamination with molecules and dust particles from the ambient air. After thoroughly vortexing, the diluted vesicles 1 mL of the lipid suspension was pipetted on top of the crystal and mixed about ten times. To prevent the destruction of an already formed lipid bilayer the crystal was not allowed to get in contact with air. The petri dish was left for about 20 mins to allow the formation of a supported lipid bilayer. Subsequently, the following procedure was repeated five times to remove non-adherent lipid vesicles from the petri dish. 1 mL of buffer is added to the petri dish on top of the crystal. Then five times 1 mL of liquid is taken from the side of the dish and added on top of the crystal without allowing air to touch the crystal surface. Afterwards 1 mL of liquid is disposed from the petri dish to remove excess lipid vesicles.

Bilayers on self-assembled monolayers were produced according to the following procedure. 55 μL of SUVs in Ca-free Tris buffer at different concentrations were added to the Teflon measurement chamber on top of the freshly prepared self-assembled monolayer/gold surface (for details see sections 2.4 and 2.6). After allowing the vesicles to settle for 20 mins at room temperature, excess lipids were removed by exchanging the solution in the chamber with standard Tris buffer. A complete removal was ensured by four repetitions. The rupture of lipid vesicles and the bilayer formation were induced by injecting 10 μL of pure 100 mM $CaCl_2$ solution into the chamber. Further measurements were performed after an incubation time of 20 mins at room temperature to allow the complete bilayer formation.

2.4 Electrochemical Measurements

A quick and reliable method to confirm the formation and quality of lipid bilayers are electrochemical measurements. In the present work the home-built sample cell shown in Fig. 2.12 was used. Gold wafers tailored hydrophilic with the SAM mercaptohexanoic

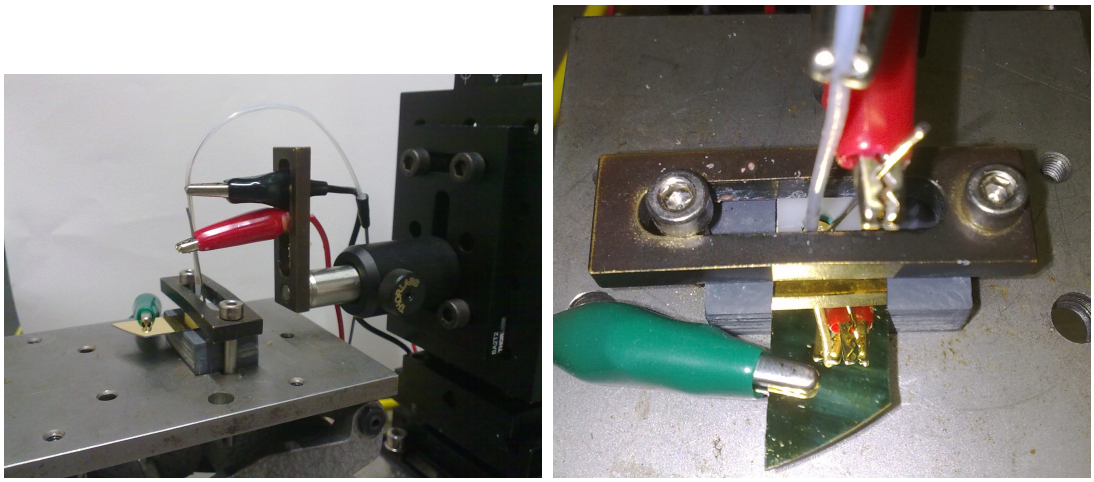

(a) View sideways (b) Front view

Figure 2.12: This figure depicts the home-built electrochemical sample cell for lipid bilayer measurements. The red clamp / platin wires acted as working electrodes, the green clamp / Au substrate as the counter electrode. The reference electrode was a Ag/AgCl electrode held by the black clamp.

acid (for the preparation see section 2.6) were fixed with a clamp in between two teflon blocks. Of those two the upper block featered a teflon O-ring and thus prevented the leakage of liposome and buffer solutions (cf. Fig. 2.12(b)). The whole apparatus was placed on a vertical stage to adjust the height and bring the electrodes in contact with the solution. For fine adjustments in height as well as translation in x and y directions the electrode holder was fixed on two lateral translation stages (Fig. 2.12(a)). The gold substrate providing the surface for the bilayer formation also acted as the counter electrode. The working electrode was formed by a platin wire whereas a commercially available Ag/AgCl electrode was the reference electrode (FLEXREF, World Precision Instruments, Berlin, Germany). All electrodes were connected to a computer-operated potentiostat (EmStat, PalmSens, Netherlands).

The measurements were conducted as follows. For reference a voltammogram with pure Ca/Tris buffer solution as used for the final bilayer measurements was recorded. Subsequently, a bilayer was formed on the substrate according to the procedure described at the end of section 2.3. To check the integrity of the formed bilayer the voltage was increased from -300 mV to 300 mV with a rate of 5 mV/s while the current was constantly recorded. The recorded data underwent no further processessing and was analyzed as obtained with the potentiostat.

2.5 Quartz-crystal microbalance with dissipation monitoring (QCM-D)

In 1959 Sauerbrey proposed the use of quartz-crystals as microbalances. Shortly after the first QCM measurements were performed in the late fifties and early sixties of the last century [81]. It was already a well established technique in fields of electrochemistry and as a sensor in biomedical sciences [82, 83, 84] before Kasemo et al. showed in 2000 that quartz-crystal microbalances with dissipation monitoring are a valuable tool for the investigation of lipid bilayer formation from lipid vesicles [85]. Soon after his publication it emerged as a standard technique in this area of research [73, 80].

A QCM essentially based on the fact that the eigenfrequency of a quartz-crystal depends on its mass and on the mass being in contact or moving with the oscillating crystal. However, a quartz crystal can exhibit three types of vibrations: an extensional, a shear and a torsional vibration in each of the three axes. Moreover, the different modes could also couple to exhibit very complicated resonances. The vibrational mode that is most sensitive to an addition of mass is the thickness-shear mode. However, the suppression of all unwanted oscillations can be achieved by cutting the quartz crystal to a specific orientation with respect to the crystal axes. These cuts are typically the AT- and BT-cuts describing the angle at which a crystal is cut with respect to its growing direction. Using AT- and BT-cuts facilitates the description of the crystal's vibration in pure shear mode as its motion is only one-dimensional [86].

The mass m of the crystal (and adherent material) is related to the eigenfrequency over its thickness d

$$d = \frac{m}{A \cdot \rho} \tag{2.32}$$

with A being the area and ρ the density of the crystal. As the vibration of the AT-cut crystal is an oscillation in shear mode, the crystal's thickness equals half the wavelength corresponding to the eigenfrequency f

$$f = \frac{v_{\mathrm{tr}}}{2 \cdot d} \tag{2.33}$$

with the transverse velocity v_{tr}. By substituting Eq. 2.32 into Eq. 2.33 the mass can be directly related to the eigenfrequency

$$m = \frac{v_{\mathrm{tr}} A \rho}{2f} \tag{2.34}$$

A change of the eigenfrequency $\frac{\Delta f}{f}$ can therefore be calculated from the thickness change Δd.

$$\frac{\Delta f}{f} = -\frac{\Delta d}{d} = -\frac{\Delta m_Q}{m_Q} = -\frac{\Delta m_Q}{\rho_Q A d} \tag{2.35}$$

with a mass change of the quartz crystal Δm_Q. An adsorption of other material but of about the same thickness results in the same frequency change

$$\frac{\Delta f}{f} = \frac{\Delta m}{\rho_Q A d} \tag{2.36}$$

where Δm is the adsorbed mass. Thus the change of mass is directly proportional to a change of the eigenfrequency Δf.

$$\Delta m = -C \Delta f \tag{2.37}$$

The constant C was introduced to combine all intrinsic properties of the quartz crystal.

$$C = \frac{f}{A d \rho_Q} \tag{2.38}$$

However, equation 2.37 is only true under the assumption that the adsorbed mass is uniformly distributed over the oscillating crystal and that it is smaller than the weight of the crystal itself, i.e. $\Delta f / f \ll 1$. For one side of an AT-cut crystal being covered by the mass Δm the constant $C = 4.5$ ng/cm^2 Hz^{-1} [87].

Kasemo et al. showed in 1995 that, given the correct experimental setup, it is possible to simultaneously monitor the changes of the eigenfrequency and the energy dissipation which can be directly related to mass and viscosity changes of adherent material, respectively [87]. Dissipation factor D or Q factor Q can be defined as

$$D = 1/Q = \frac{E_{\mathrm{diss}}}{2\pi E_{\mathrm{stored}}} \tag{2.39}$$

with the energy dissipated during one oscillation cycle E_{diss} and the energy stored in the system E_{stored}. In a gaseous environment a 10 MHz AT-cut quartz crystal has typically a dissipation factor of 10^{-4} to 10^{-6}. However, in liquid environments D rises drastically due to liquid coupling to the crystal and thus increasing the viscosity of the system.

The simple electric circuit shown in Fig. 2.13 is the electrical equivalent of a quartz crystal unit near resonance. The capacitance C represents the mechanical elasticity and the inductance L corresponds to the vibrating mass of the oscillating crystal. The resistance R is a measure of the total loss of energy to the surrounding medium and the supporting structure. The capacitance C_0 is the actual capacitance originating from the connected electrodes and stray capacitance of the supporting structure. A resonance

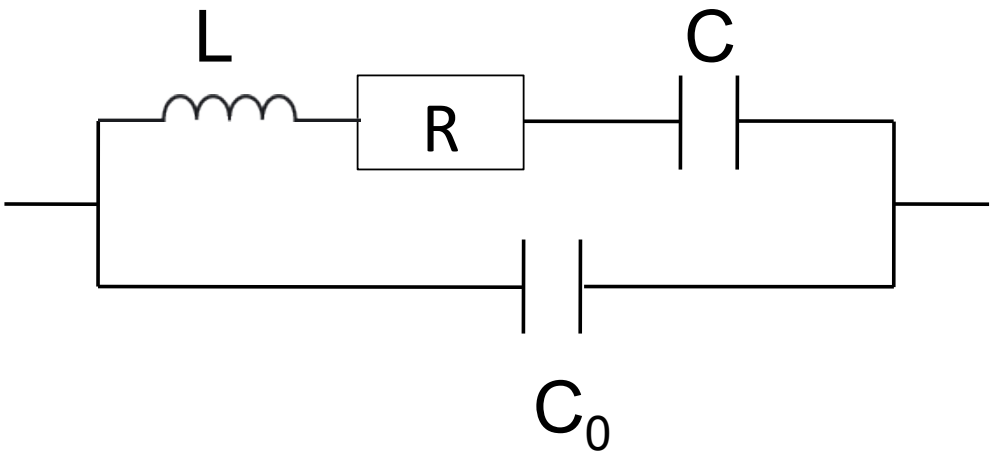

Figure 2.13: The electric circuit represents the piezoelectric quartz crystal oscillator.

of the quartz crystal occurs when the complex impedance of the equivalent circuit is only resistive. This is achieved for the two resonant frequencies f_s and f_p

$$f_s = \frac{1}{2\pi\sqrt{LC}} \tag{2.40}$$

and

$$f_p = \frac{1}{2\pi}\sqrt{\frac{1}{LC} + \frac{1}{LC_0} + \frac{R^2}{L^2}} \tag{2.41}$$

The frequencies are called series and parallel resonances. A quartz crystal resonator used as a microbalance usually operates in the series resonance mode. Thus from Eq.

2.40 it can be seen that the resonance frequency is not affected by C_0. But Eq. 2.40 also illustrates that a shift of the resonance frequency is related to a change of the motional inductance L. According to Eq. 2.40 an increase or a decrease in mass of the resonator (or its equivalent L) corresponds to a decrease or an increase in the resonance frequency f. From the equivalent electrical circuit in Fig. 2.13 the dissipation factor D can be derived

$$D = \frac{R}{\omega L} = \frac{R}{2\pi f L} \tag{2.42}$$

For the simple circuit in Fig. 2.13 the resonance frequency changes according to

$$f = f_0 \sqrt{1 - \frac{D^2}{2}} \approx f_0 \tag{2.43}$$

with f_0 being the resonance frequency without any losses. The approximation is true for $D \ll 1$. The maximum amplitude of the motion $A_{\max}$ at resonance is

$$A_{\max} = \frac{F}{D\sqrt{1 - \frac{D^2}{4}}} \approx \frac{F}{D} \tag{2.44}$$

where F is the driving force divided by the force constant. Again the approximation holds only for $D \ll 1$. For a quartz crystal resonator used as a microbalance D is in fact the sum of all losses in the system

$$D = \sum_i D_i \tag{2.45}$$

with D_i being the dissipation factor e.g. due to energy losses because of internal friction in the crystal or the mounting. Furthermore, the adsorbed film can also be a cause of energy dissipation. For instance, a film slipping on the electrode can be used to determine the coefficient of friction between the film and the electrode. Moreover, from the energy dissipation it is possible to infer the degree of viscosity the film exhibits.

To accurately determine the dissipation factor D Kasemo et al. concentrated on the fact that the oscillation of the quartz crystal is damped when the driving force is switched off. The oscillatory amplitude then follows a sinusoidal curve for $t \geq 0$

$$A = A_{\max,0} \exp -t/\tau \sin(2\pi t + \varphi) + C \tag{2.46}$$

where $A_{\max,0}$ is the maximum amplitude at $t = 0$, τ is the decay time, φ is the phase and C a constant due to a DC offset. τ can be related to the total dissipation factor

D according to

$$D = \sum_i D_i = \frac{1}{\pi f \tau} \tag{2.47}$$

Thus an increase of one dissipation factor D_i due to a higher viscosity leads e.g. to a smaller decay time τ. By monitoring the oscillatory motion and fitting it to Eq. 2.46 the dissipation factor can be derived from Eq. 2.47. An accurately determined dissipation factor D enables the researcher to draw conclusions regarding structural changes in the film. Therefore the quartz crystal microbalance emerged to QCM-D, an abbreviation for quartz crystal microbalance with dissipation monitoring, an integral technique for studying film properties *in situ*. For the bilayer formation experiments a commercially available QCM-D setup (Q-Sense E1, Sweden) with flow module was used kindly provided by the Institute for Functional Interfaces (KIT). The QCM-D sensors were custom products based on standard 14 mm crystals with a 200 nm gold layer and 50 nm silicon dioxide on top.

2.6 Gold substrate and self-assembled monolayer preparation

As described in the introduction 1.2 self-assembled monolayers from alkanethiols offer a well-defined system for studying fundamental structural film properties. Moreover, they are easy to handle for the functionalization of several noble metals. In this work they were used to form SAMs on gold.

The gold films were kindly fabricated in the laboratory of Dr. Hans-Michael Bruns at the IAM-WPT (Karlsruhe Institute of Technology). Silicon wafers (Si-Mat Silicon Materials, Kaufering, Germany) were covered with a 10 nm adhesion layer of chromium using radio-frequency magnetron sputtering. On top of this layer a gold layer of 200 nm thick gold film was sputtered. Gold substrates produced with this method typically exhibit a (111) orientation as was also reported by Heister et al. [88]. Then, a glass cutter was used to cut the gold wafers into appropriate sizes. These pieces were cleaned by exposing them to UV/ozone (UV-cleaner 42-220 from Jelight) for 2 hrs. To avoid island formation as observed by Woodward et al. the clean wafers were immersed in pure ethanol for at least 10 mins prior to film deposition [89].

The alkanethiols utilized for the SAM preparation were purchased from Sigma-Aldrich Chemie GmbH (Munich, Germany) in the case of dodecanethiol (DDT) and mercaptohexanoic acid (MHA). Aminoundecanethiol (AUT) and mercaptoundecaneamide (MUA) were ordered from ProChimia Surfaces Sp. z o.o. (Sopot, Poland). All chemicals were used as delivered without any further purification. The DDT, MHA and MUA films were produced by immersing the clean gold substrates in 3 mM ethanolic thiol solutions for at least 20 hrs at room temperature. In contrast, the AUT solutions additionally contained 3 % (v/v) triethylamine to prevent multilayer formation as observed by Jiang et al. [90]. The samples were then removed from the solutions, thoroughly rinsed with ethanol and dried with a stream of gaseous nitrogen. AUT samples underwent the a slightly different procedure. After being rinsed with ethanol they were rinsed with a 10 % (v/v) solution of acetic acid and again ethanol before being dried with nitrogen.

2.6.1 Preparation of pyridine-terminated self-assembled monolayers

The gold substrates used for the formation of pyridine SAMs were prepared differently than previously described. Onto freshly cleaved mica sheets 150 nm gold (99.99 %, Chempur GmbH, Karlsruhe, Germany) was evaporated at 450° C to produce a Au(111) film. Prior to use, the substrates were annealed with a hydrogen flame and mirror polished.

The pyridine-terminated thiols were prepared as described by Schüpbach and Terfort [91]. Briefly, the synthesis of PyPP1 and PyPP2 was performed using a building block approach. The commercially available 4-(4-bromophenyl)pyridine was reacted with the Grignard reagents 4-bromophenylalkyl TIPS-thioethers with a chain length of one and two carbon atoms in the presence of Pd(dppf)Cl_2. This so-called Kumada reaction produced the coupling products. Eventually, the thiol group was deprotected protolytically with hydrochloric acid, before the pyridyl ring was deprotonated by adjusting the pH to 8. The PyPP1 and PyPP2 films were formed by immersing the gold wafers in 20 μM ethanolic solution for 20 to 24 hrs. Prior to electrochemical SFG experiments wafers were removed from the thiol solutions, rinsed thoroughly with ethanol and dried under a gentle stream of gaseous nitrogen.

2.7 Dynamic light scattering (DLS)

Dynamic laser light scattering is well known for its ability to probe properties of e.g. biological macromolecules. Intensity fluctuations of scattered light caused by the diffusive motion of small particles in solution is used for the determination of size or shape of these macromolecules [92]. Hence it is predestined for the size determination of small unilamellar vesicles [93][94].

Laser light of a fixed wavelength and incident on a particle solution is scattered by the particles and detected with an autocorrelator to calculate an autocorrelation function of first order [95]. The normalized time autocorrelation function of the intensity I of the scattered light is given by

$$g^{(2)}(\tau) = \frac{\langle I(t)I(t+\tau)\rangle}{\langle I(t)\rangle^2} \tag{2.48}$$

where the brackets indicate a time averaging and τ is a given delay time. The intensity autocorrelation function 2.48 can now be rewritten with the field-field time autocorrelation function and reads

$$g^{(2)}(\tau) = C + \beta[g^{(1)}(\tau)]^2 \tag{2.49}$$

where C defines a baseline most often chosen to be 1, β is a correction factor and $g^{(1)}(\tau)$ is defined as

$$g^{(1)}(\tau) = \frac{\langle E(t)E^*(t+\tau)\rangle}{\langle E(t)E^*(t)\rangle} \tag{2.50}$$

Here $E(t), E^*(t+\tau)$ are the scattered electric fields at the respective time points. $g^{(1)}(\tau)$ can then be expressed as a function of the decay rate Γ and the diffusion coefficient D

$$g^{(1)}(\tau) = \int_0^\infty G(\Gamma)e^{-\Gamma\tau}d\Gamma \tag{2.51}$$

with a distribution of decay rates $G(\Gamma)$ and $\Gamma = Dq^2$. However, if the solution is monodisperse the integral in Eq. 2.51 is superfluous and the equation simplifies to

$$g^{(1)}(\tau) = e^{-Dq^2\tau} \tag{2.52}$$

The scattering vector q can be deduced from known quantities with

$$q = \frac{4\pi n}{\lambda}\sin(\theta/2) \tag{2.53}$$

Here λ is the fixed wavelength of the incident light, n the refractive index of the solvent and θ the incidence angle of the scattered light. As in the present experiment $\theta = 90°$ Eq. 2.53 simplifies to $q = \frac{2\sqrt{2}\pi n}{\lambda}$. Thus it is possible to fit the determined intensity autocorrelation function 2.48 and quantify the diffusion coefficient D. D is now related to the radius of the particles r through the Einstein-Stokes equation

$$D = \frac{k_B T}{6\pi\eta r} \tag{2.54}$$

with Boltzmann's constant k_B, the temperature T and the viscosity η [96].

The measurements have been conducted on a Zetasizer 5000 from Malvern Instruments at the Institute of Functional Interfaces at the KIT. To ensure reliable and reproducible results the temperature was held constant at 25° C and the lipid solutions were appropriately diluted prior to the experiments.

2.8 AHL preparation

All solvents and chemicals used for the reactions were purchased from commercial suppliers. Solvents were dried under standard conditions; chemicals were used without further purification. All reactions were carried out under nitrogen in flame-dried glassware. The evaporation of solvents and the concentration of reaction mixtures were performed in vacuo at 60° C on a Büchi rotary evaporator. Thin-layer chromatography (TLC) was carried out on silica gel plates (Kieselgel 60, F254, Merck) with visualization by iodine vapor. Normal-phase silica gel (Silica gel 60, 230-400 mesh, Merck) was used for preparative chromatography. At first, 5-acyl Meldrum's acid derivatives (3 a-c) were prepared in nearly quantitative yields by 1-ethyl-3-(3-dimethylaminopropyl)carbodiimide (EDC) mediated condensation of appropriate deuterated carboxylic acids (1 a-c) with Meldrum's acid (2,2-dimethyl-1,3-dioxane-4,6-dione) (2) in the presence of 4-(N,N-dimethylamino)pyridine (DMAP) (cf. Fig. 2.14). To a stirred 0.80 mM solution of the previously prepared acylated Meldrum's acid in 30 mL acetonitrile 0.80 mM L-homoserine lactone hydrobromide and 0.96 mM triethylamine was added. The complete mixture was stirred at room temperature for 2 hrs, then heated under reflux for 3 hrs and again at room temperature overnight. The solvent was removed by rotary evaporation and the residue was redissolved in ethyl acetate. The organic solution was sequentially washed with saturated $NaHCO_3$, 1 M $KHSO_4$ solution and brine. The

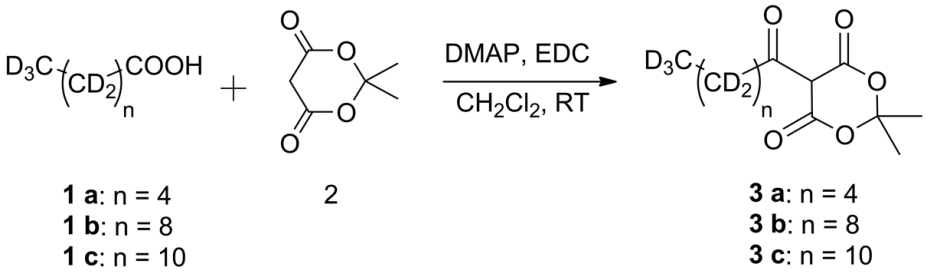

Figure 2.14: Acylation of Meldrum's acid (2) by deuterated fatty acids (1a-c).

combined aqueous layers were washed one more time with ethyl acetate. The combined organic layers were dried over Na_2SO_4 and concentrated under reduced pressure. The crude product was purified by flash column chromatography (hexane/ethyl acetate 1:2) to yield the desired deuterated AHL (4a-c) as a white solid (cf. Fig. 2.15 and Tab. 2.2).

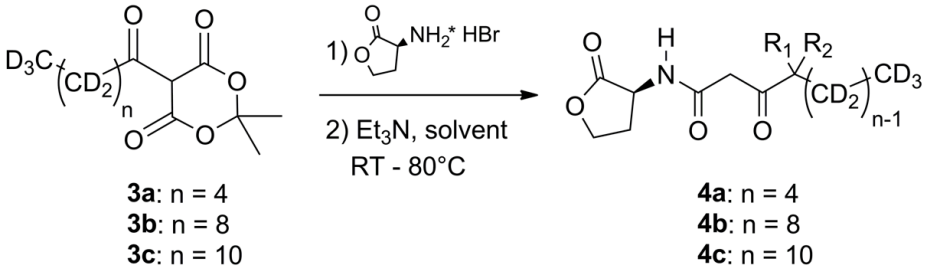

Figure 2.15: Amidation of 3a-c with L-homoserine lactone (L-HSL) hydrobromide (R1, R2 = H or D).

AHL	n	Product	Time (hrs)	Yield (%)	Solvent
D-9	4	4a	24	70	CH_3N
D-17	8	4b	17	60	CH_3N
D-21	10	4c	36	42	EtOAc

Table 2.2: Results of the amidation

2.9 Contact angle measurements

As already described in the introductory chapter 1.2 the wettability of SAMs is essential for the formation of high quality lipid bilayers on a solid support. In order to study whether and to which extent a self-assembled monolayer renders a surface hydrophilic contact angle measurements are performed. Furthermore, these measurements also provide an easy and quick method to check the correct formation of the SAMs of interest.

The contact angle of a water droplet on a surface is a measure of the liquid's internal cohesion forces in relation to the adhesion forces between droplet and substrate. Is the adhesion force greater than the cohesion force then the contact angle is below 90° and the substrate must be hydrophilic (cf. Fig. 2.16). In contrast, higher cohesion forces lead to a contact angle greater than 90° marking a hydrophobic surface [97]. A setup

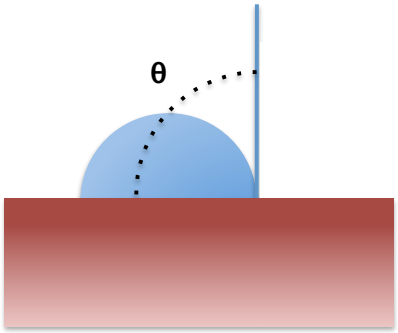

Figure 2.16: Scheme of a droplet on a hydrophobic surface. The contact angle is denoted as θ.

to measure the contact angle can be quite simple. It consists of a, preferably, point light source and a device to observe the water droplet consisting of HPLC pure water. In the setup used in this work a CCD camera was employed to take digital photos of droplet and surface. Furthermore, to obtain an accurate image the sample was placed on a traveling stage allowing the accurate positioning of the sample and allowing to change the tilt angle. The analysis of the digital images was performed with the free Java-based computer program ImageJ in combination with the LBADSA plugin [98].

2.10 Infrared reflection absorption spectroscopy (IRRAS)

Infrared light is able to induce vibrational motions within molecular bonds resulting in the absorption of infrared light of a specific wavelength. In turn, this leads to a decrease of the transmitted intensity at that particular wavelength. This drop in intensity is measured after the sample and compared to the previously recorded value of a reference. The decrease is directly related to the amount of the molecular bonds excited in the investigated sample. Moreover, the absorbed wavelength is unique for each bond and therefore the sample composition can be deduced from the recorded spectra [5].

The wavelength λ (or frequency $\nu = c/\lambda$) of the photons absorbed by the molecular vibrations can be derived from a simple diatomic spring model consisting of two masses m_1 and m_2. The displacements of the masses from their equilibrium positions is described by x_1 and x_2. According to Hooke's law the restoring force acting on the atoms is then given by

$$F_r(x_1 - x_2) = -K(x_1 - x_2) = -K\Delta x \tag{2.55}$$

The classical equation of motion reads

$$m\ddot{x} = -K\Delta x \tag{2.56}$$

The wavelength of a vibrational band derived from this classical model is given by

$$\lambda = 2\pi c\sqrt{\frac{m_1 m_2}{K(m_1 + m_2)}} \tag{2.57}$$

Integrating Eq. 2.55 leads to the corresponding harmonic potential.

$$V(x) = \frac{1}{2}Kx^2 \tag{2.58}$$

Even though the model gives a good description of the observed bands, it is more accurate to consider that all processes are happening on an atomic scale. Therefore the Schrödinger equation of the process shall be briefly examined.

$$\widehat{H}\psi_\nu(x) = E_\nu\psi_\nu(r) \tag{2.59}$$

with a given state ν and its energy eigenvalue E_ν as well as the corresponding wave functions ψ_ν. According to Eq. 2.58 the Hamiltonian of the system is defined as

$$\widehat{H} = -\frac{\hbar}{2\mu}\frac{d^2}{dx^2} + V(x) = -\frac{\hbar}{2\mu}\frac{d^2}{dx^2} + \frac{1}{2}Kx^2 \tag{2.60}$$

with x being the position operator. The energy eigenvalues of the Schrödinger equation 2.59 are then given by

$$E_\nu = \left(n + \frac{1}{2}\right) h\nu = \left(n + \frac{1}{2}\right) \frac{hc}{\lambda} \tag{2.61}$$

where $n = 0, 1, 2, ...$ is the vibrational quantum number and h the Planck constant (6.626×10^{-34} Js).

Most of the infrared spectrometer employed today are Fourier-transform infrared (FTIR) spectrometer consisting of an infrared light source, a so-called glow bar, a Michelson interferometer and an IR detector. The Michelson interferometer directs one half of the IR beam on a moving mirror and the other half on a fixed mirror. The final path difference l leads to a phase shift of the waves $\phi = \frac{\omega l}{c}$ at the detector and thus results in an interferogram caused by destructive and constructive interference. For a monochromatic light source the intensity would be proportional to a cosine function

$$I(l) = I_0 \left[1 + \cos(2\pi l/\lambda)\right] \tag{2.62}$$

Since the glow bar emits polychromatic infrared light, the resulting interferogram is a superposition of all cosine functions which can be expressed as an integral

$$I(l) = \int_0^\infty I_0[1 + \cos(2\pi l/\lambda)]d\lambda \tag{2.63}$$

The IR spectrum can then be obtained by an inverse Fourier transform of Eq. 2.63

$$I(\lambda) = \frac{1}{2\pi} \int_{-\infty}^{\infty} I(l) e^{-il\lambda} dl \tag{2.64}$$

As several factors like ambient air, light source and, for SAMs, the gold substrate, with its plasmon resonances, all contribute to the spectra and each to a different extent, it is necessary to record a background or reference spectrum I_{BG} prior to the acquisition of the sample spectrum I. Vibrational bands of the sample are then displayed as a so-called difference spectrum in absorption units and are calculated as follows

$$A(\lambda) = -\log_{10} \frac{I(\lambda)}{I_{\mathrm{BG}}(\lambda)} \tag{2.65}$$

For the study of thin films such as SAMs the reflection absorption technique is predestined. The metallic substrate with the investigated monolayer is placed in an adequate accessory that allows a low incidence angle of the IR beam. This low angle

as well as dual penetration of the film increases the amount of probed material and thus increases the overall signal strength. In the present work a Vertex 80 FTIR spectrometer from Bruker Optics, Germany was employed. The SAMs were measured with a Bruker IRRAS accessory with a fixed incidence angle of 80°. The absorption spectra of the SAMs were acquired against a perdeuterated reference SAM to obtain a clean background spectrum. Acquisition as well as further data processing were performed with the OPUS software distributed with the instrument.

3

Investigation of AHL - lipid bilayer interactions

In this chapter the investigation of AHL incorporation into lipid bilayers will be described in depth. The first three sections focus on the optimization of the formation of supported lipid bilayers. In section four the detection of AHLs with SFG spectroscopy will be discussed. Section five addresses the question if AHLs can flip through lipid bilayers.

3.1 Dynamic light scattering

When using the method of vesicle fusion for the formation of supported lipid bilayers it is essential to know their size after extrusion as only vesicles of a sufficiently small size form bilayers [73]. Hence the vesicle size of the lipid composition POPC:POPG 1:1 after extrusion was determined with the help of dynamic light scattering (DLS). In Fig. 3.1 DLS measurements of vesicles before (black) and after extrusion (red) are depicted. Before extrusion the size distribution is broad and spread from 2000 to over 3000 nm with an additional distribution around 500 nm. These big sizes do not allow the formation of uniform and stable lipid bilayers on a solid substrate. In contrast after the extrusion through 100 nm pore membranes the vesicle sizes are limited to a narrow distribution centered at 150 nm. Moreover the FWHM is only 40 nm. This favors the adherence and particularly the rupture of the liposomes on a solid substrate and thus allows the formation of high quality supported lipid bilayers. In order to

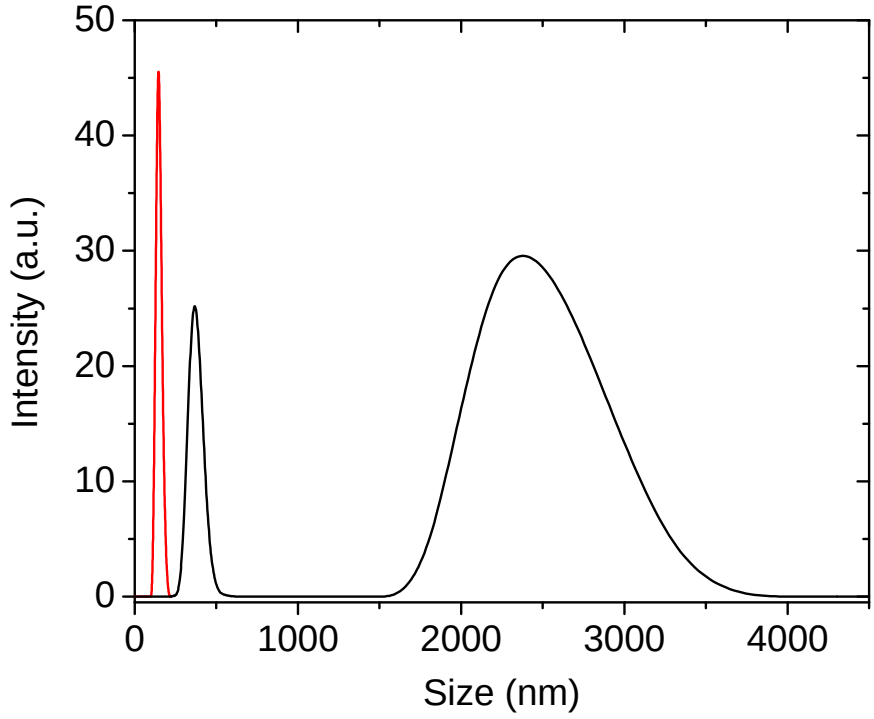

Figure 3.1: The black curve shows the size distribution of POPC:POPG 1:1 vesicles before extrusion. The size values are spread over a wide range from 2000 to 3000 nm which inhibiting lipid bilayer formation. Moreover, an additional second peak can be found at around 450 to 500 nm. After extrusion (red curve) the sizes are limited to just a narrow range at values around 150 nm.

establish a reliable and stable lipid composition for the AHL experiments several lipid compositions have been tested. Exemplarily, a DLS measurement of POPE:POPG 3:1 vesicles is compared in Fig. 3.2 to the finally chosen POPC:POPG 1:1 composition. As the tendency to form better bilayers decreases with the curvature, the bigger diameters of the POPE:POPG 3:1 liposomes at around 300 nm are not optimal for the formation of lipid bilayer. Furthermore, a broader size distribution with a FWHM of 70 nm as compared to the narrow distribution of the POPC:POPG 1:1 vesicles (FWHM 40 nm) indicates that the POPE:POPG 3:1 lipid composition does not produce lipid bilayers of high quality.

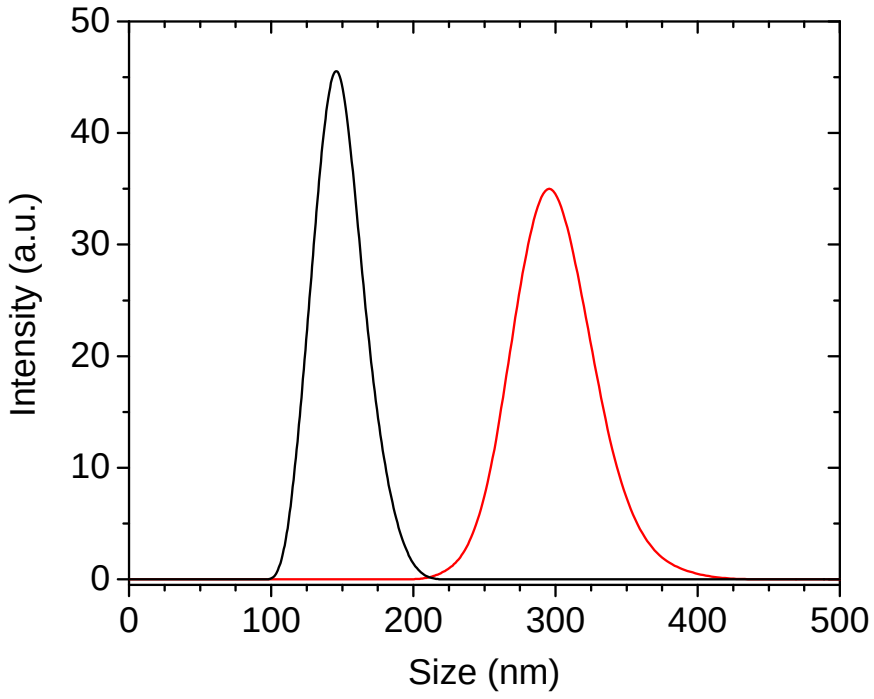

Figure 3.2: The black and red curves depict the size distributions of POPC:POPG 1:1 and POPE:POPG 3:1 vesicles, respectively. Liposomes produced from POPE:POPG show a broader size distribution as well as in general bigger sizes. Thus they are not as suited for the bilayer formation as the POPC:POPG vesicles.

3.2 Electrochemical measurements

Electrochemical measurements were conducted in order to find a SAM suitable as a substrate for supported lipid bilayers and subsequently to verify, if the produced liposomes are able to form stable and closed lipid bilayers. According to the procedure given in section 2.3 liposome solutions were transferred to the measurement chamber on top of the gold wafer functionalized with a hydrophilic SAM. The electrochemical measurements started immediately after the waiting time as described in section 2.4. The typical total duration of an experiment was about 1 hr.

In the first electrochemical experiments, depicted in Fig. 3.3, it was tested which of the employed SAMs mercaptohexanoic acid (MHA), aminoundecanethiol (AUT) and mercaptoundecane amide (MUA) is best suited for the formation of supported lipid bilayers. From the findings in the previous section the experiments were conducted with a POPC:POPG 1:1 lipid mixture at a concentration of 2.5 mg/mL. After the waiting time the currents through the chamber were recorded as a function of the applied voltage (vs. a Ag/AgCl reference electrode). As a control the current-voltage curve for a pure buffer sample was also measured. In the buffer control the current rises from -2.0 μA until its electrochemical window begins at around -0.1 V and the current stays nearly constant. In contrast, in the case of a supported lipid bilayer the loading current stays constant from the start and over a wide range of voltages. This originates from a bilayer acting basically like a capacitor. During a short period a current flows when it is charged (not shown here). Subsequently, no electric charge flows through the bilayer, if it is perfectly formed. Such a case can only be observed for the MHA SAM for which the current is nearly zero for the complete measurement range. In contrast, on MUA and AUT no bilayer forms. However, the flatter slopes show that some kind of resistance exists indicate that vesicles may have adhered to the SAMs but did not rupture. Hence in the subsequent experiments only gold wafers functionalized with MHA served as hydrophilic substrates.

Figure 3.4 shows the course of the recorded current vs. the applied voltage for the two different lipid compositions POPE:POPG 3:1 and POPC:POPG 1:1. Both curves were recorded with a lipid concentration of 2.5 mg/mL in standard Ca/Tris buffer. For the POPC:POPG bilayer the current is nearly zero for the complete measurement range demonstrating the formation of a bilayer. In the case of the POPE:POPG 3:1 lipid

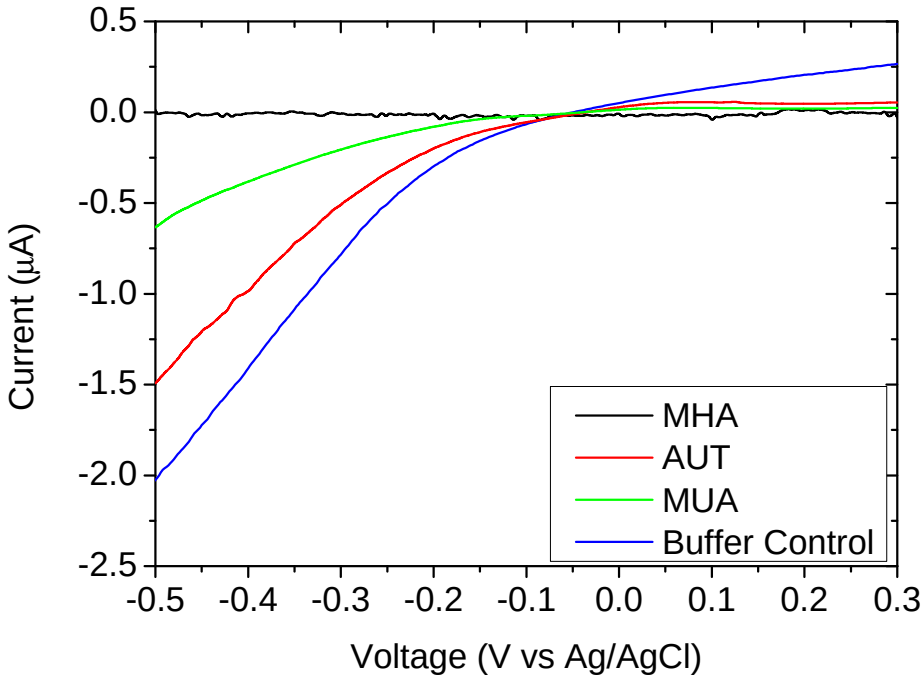

Figure 3.3: Current-voltage curves for three different hydrophilic alkanethiols on gold are shown. With the employed lipid mixture POPC:POPG 1:1 only the flat curve of MHA demonstrates the formation of a closed and stable supported lipid bilayer. In contrast AUT and MUA closely resemble the buffer control indicating no bilayer formation, but with the flatter slopes the potential adherence of unruptured lipid vesicles.

composition the rising current at 85 mV indicates that, although bilayers did form, they were not as stable and potentially closed as those formed by POPC:POPG 1:1. This current is due to a hole in the bilayer allowing ions to flow through and thus generating a current. In contrast, the POPC:POPG bilayer did not show such a phenomenon, hence it can be concluded that in the range of the measurement errors it is completely closed and stable. This result is in accordance to the DLS measurements which showing a size distribution substantially larger than the distribution for the POPC:POPG 1:1 composition.

Figure 3.5 shows a comparison of three different concentrations for POPC: POPG 1:1 lipid vesicles. Apparently, liposomes at a concentration of 0.1 mg/mL did not form bilayers at all. Vesicles added at a concentration of 1.0 mg/mL did produce a bilayer, however, the noise from this supported lipid bilayer was high indicating that the bilayer

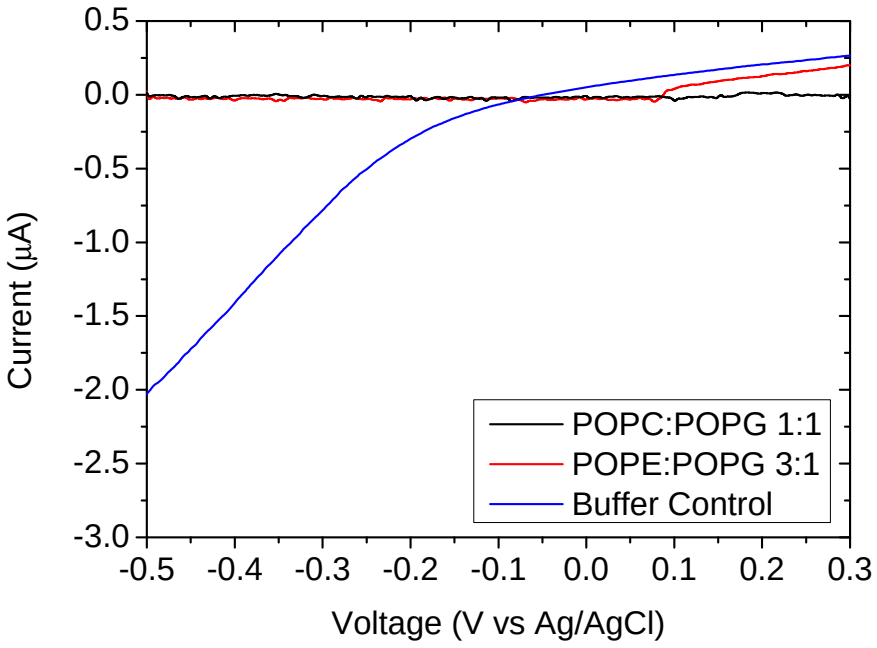

Figure 3.4: In this graph the currents at different applied voltages are shown for two different different lipid compositions. POPE:POPG 3:1 shows a significant increase at 0.1 V. This indicates that the SLB developed a great amount of defects allowing ions to flow through and leading to a current. For comparison a buffer control is also shown.

was not as good as the one at a concentration of 2.5 mg/mL. Nevertheless, all tested liposomes fabricated with the methods described in section 2.3 did form bilayers on a hydrophillically tailored gold substrate. Hence the employed procedure could be used for the preparation of lipid vesicles for the SFG experiments. However, the gold substrate in combination with a hydrophilic SAM does not offer a suitable support for the planned experiments. As will be shown in sections 3.4.1 and 4.3 both the lipid bilayer and the SAM give rise to SFG-active bands in the spectral C-H region. Thus a verification of bilayer formation would not be possible. The gold substrates also had to be discarded after each electrochemical experiment as the measurement procedure itself destroyed the hydrophilic SAM. Hence it would not be possible to confirm the substrates' ability to serve for bilayer formation with an independent technique. Therefore SiO_2-coated QCM-D crystals were chosen as supports in the actual AHL-bilayer interaction experiments.

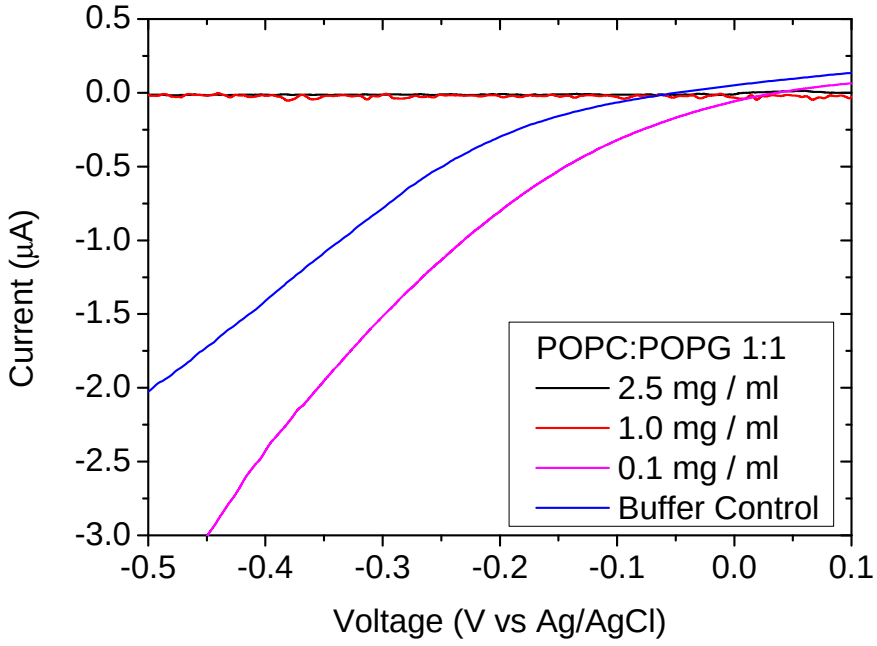

Figure 3.5: Current flowing through a POPC:POPG 1:1 bilayer at different applied voltages. Depicted are several lipid concentrations from which bilayers were formed. The graph indicates that the higher the concentration the higher the quality of a bilayer. The high noise of the red curve corresponding to a concentration of 1 mg/mL demonstrates that the bilayer is not free of defects.

3.3 QCM-D

All employed substrates i.e. several SiO_2-coated QCM-D crystals used for the formation of lipid bilayers in the AHL-bilayer interaction experiments were tested prior to the SFG measurements in a commercial QCM-D setup to ensure their quality and functionality. Figure 3.6 depicts the course of a QCM-D experiment with POPC:POPG 1:1 liposomes of about 150 nm diameter (cf. the results in section 3.1). The experiment typically started with Na/Tris buffer (1) to equilibrate the QCM-D crystal and check for the functionality of the setup. Furthermore, the temperature stability could be ensured. This is important for the validity of measurements as the resonant frequency depends directly on the temperature and any change would have resulted in a false

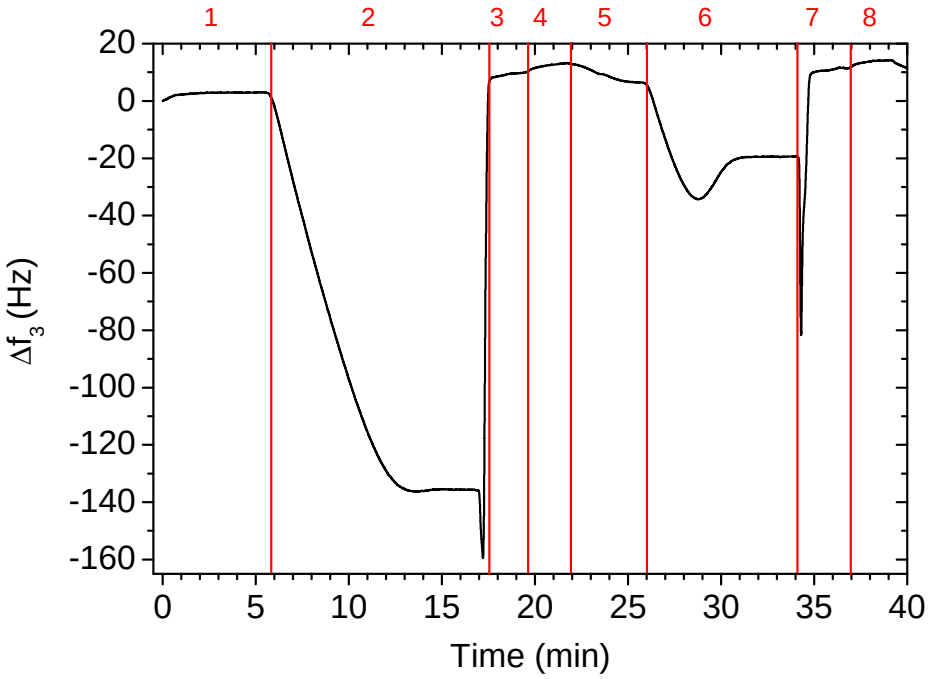

(a) Frequency changes of the third overtone of the resonance frequency.

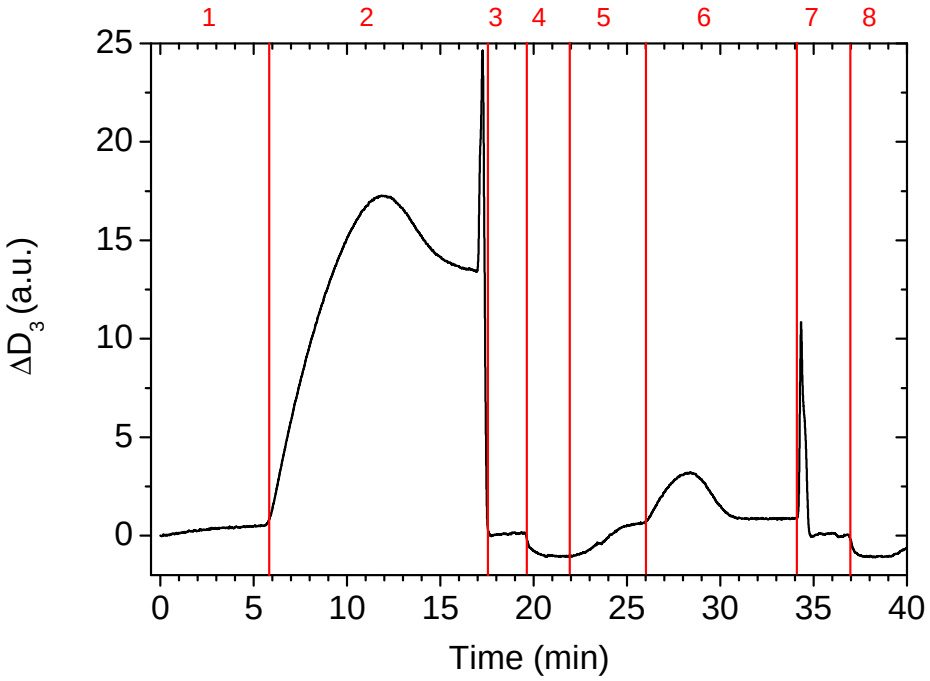

(b) Changes in energy dissipation of the third harmonic frequency

Figure 3.6: Course of a typical QCM-D experiment with POPC:POPG 1:1 liposomes, for details see the text. Numbers denote the employed solutions: 1. Na/Tris buffer 2. liposomes 3. SDS 4. MilliQ water 5. Na/Tris buffer 6. liposomes 7. SDS 8. MilliQ water

frequency change. On the addition of the liposome solution (2) the frequency dropped significantly due to vesicles adsorbing to the SiO_2 crystal surface. This increased the overall oscillating frequency and conversely decreased the resonance frequency. At the same time the dissipation increased as the adherent liposomes caused an increase in viscosity and hence an elevated energy demand to maintain the oscillation. The first addition of liposomes though did not result in the formation of a supported lipid bilayer after several minutes as can be seen from the constantly low frequency and high dissipation, i.e. only a vesicular layer had formed [80]. Thus the QCM-D crystal was cleaned with SDS (3) and water of MilliQ purity (4). Subsequently it was stabilized in Na/Tris buffer (5) to prepare another addition of POPC:POPG vesicles (6). This time the liposomes adhered to the surface and at a high vesicular coverage started to rupture, as can be seen from the abrupt increase in frequency and drop of energy dissipation. After a supported lipid bilayer did form successfully the QCM-D setup was flushed with SDS to clean all parts (7) and subsequently rinsed with MilliQ water to wash away the SDS.

In Fig. 3.7 a detailed graph of the course of frequency and dissipation during a successful lipid bilayer formation with POPC:POPG 1:1 liposomes is depicted. The change in frequency Δf_3 and dissipation ΔD_3 of the third harmonic of the resonance frequency are shown as a function of time. After a stable baseline has been established with Na/Tris buffer as well as a constant temperature, liposomes are added after ca. 4 minutes. The lipid vesicles adhere to the surface and result in a sharp drop of frequency Δf_3 and increase in dissipation ΔD_3. As explained in the last paragraph this is due to the adsorbed mass and the overall higher viscosity, respectively. At a sufficiently high vesicular coverage though the liposomes start to rupture. This causes an abrupt increase in frequency Δf_3 and decrease in dissipation ΔD_3. The drop of the energy dissipation ΔD_3 and thus of the viscosity can be explained as follows: Adherent intact vesicles extend wide into the solution above the crystal, but are at the same time connected to the crystal. Therefore the energy uptake to maintain the crystal movement is high as the torsional moment and the amount of moved water is high. However, when the vesicles break and form a bilayer on the surface, this is rather flat. Hence on the one hand almost no near-surface water and thus mass hinders the oscillation of the QCM-D crystal. On the other hand the torsional moment is almost not existent anymore as all mass is concentrated near the surface. This results in a sharp decrease of the

energy dissipation ΔD_3. The increase in frequency Δf_3 can be explained by the nature of the liposomes. They themselves are formed by a lipid bilayer and are hydrophilic at the inside and at the outside. Therefore they incorporate a high amount of water which is also coupled to the crystal adding to its mass and causing a change of the frequency Δf_3. When the vesicles rupture this water is released which results in an increase of the resonance frequency Δf_3. Ideally, the overall change of frequency δf_3 is much greater than 25 Hz corresponding to a mass uptake of $\Delta m = 112.5$ ng of lipids. In the shown experiment the supported lipid bilayer was formed by 68 Hz $\widehat{=}$ 306 ng of lipids. An optimal lipid bilayer would also result in only a small overall dissipation change $\delta D_3 < 0.5$ as shown in Fig. 3.6(b) 6. However, in this experiment there was still an overall dissipation change of $\delta D_3 = 7.5$ indicating that a certain amount of vesicles did not rupture and vesicles and bilayer coexisted on the surface.

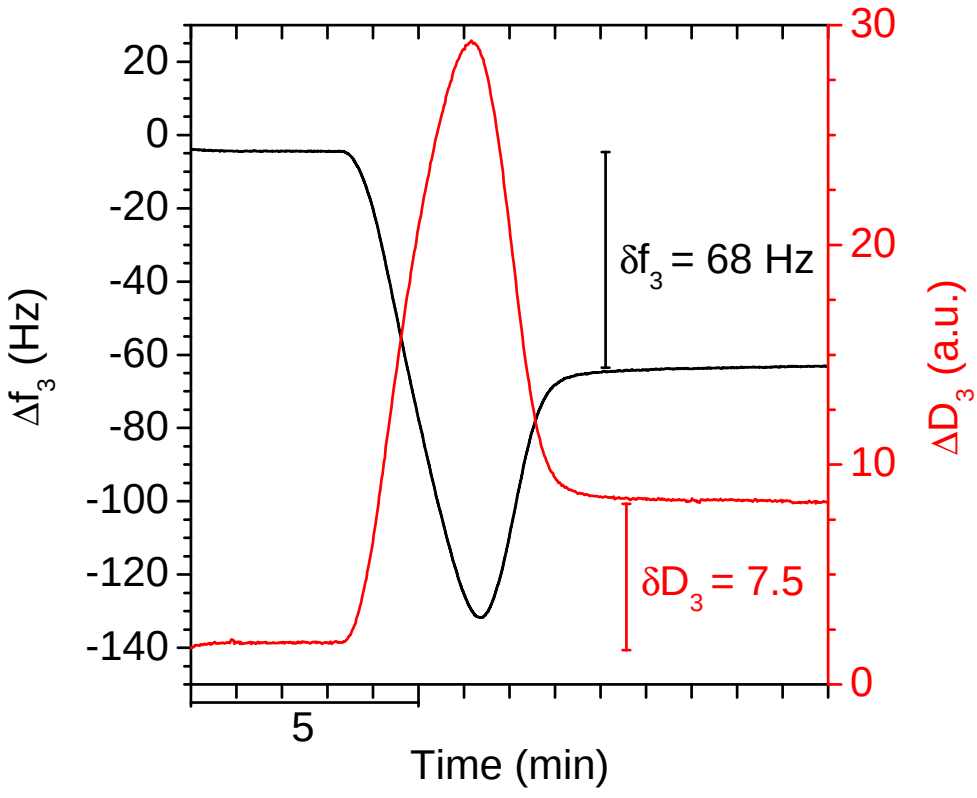

Figure 3.7: The black and red curves depict frequency and energy dissipation of the third overtone of the resonant frequency in a QCM-D experiment with POPC:POPG 1:1 vesicles.

3.4 Sum-frequency generation spectroscopy

With its surface-sensitivity SFG spectroscopy is the ideal technique to monitor the integration of molecules into a supported lipid bilayer as previously shown by Chen et al. [35] [99]. In the first section SFG spectroscopy will be used to investigate the formation of supported lipid bilayers on SiO_2 and how their quality depends on the presence of Ca^{2+} ions. The subsequent section will then focus on the integration and orientation of acylated homoserine lactones into lipid bilayers and how this can be determined by means of SFG spectroscopy.

3.4.1 SLB formation monitored with SFG spectroscopy

Supported lipid bilayers were produced according to the procedure described in section 2.3. However, for one sample the Ca/Tris buffer was carefully exchanged for a Tris buffer not containing Ca in order to determine potential changes in the bilayer structure and SFG signal. After all preparations had successfully been finished, SFG measurements started immediately using the TLA cell. In order to verify the signal quality and check for any malfunction of the SFG spectrometer, spectra were first recorded with the nonresonant background of gold. This allows real-time setup changes due to a higher SFG signal. Such spectra are depicted in Fig. 3.8(a). Slight variations in the spectra can be observed about 2900 cm^{-1}. However, the differences between black and red curves corresponding to Ca-free and Ca-containing buffer are not significant. They are rather due to a different spectrometer alignment for the respective samples than real bands. In order to confirm that supported lipid bilayers do not give rise to a strong SFG signals, the nonresonant background was suppressed as previously described (cf. section 2.1.4). Spectra of each sample are shown in Fig. 3.8(b). Here weak bands between 2800 and 2900 cm^{-1} can be observed. The signal-to-noise ratio is, even with exposure times of 90 s, very low. Bands attributable to C-H stretching vibrations are located here. However, because of signal strengths as low as 0.5 Cts. s^{-1} it will be refrained here from giving any detailed assignments. The signals are generated by small asymmetries in the bilayers. From the consistent band positions and their strength it can be concluded that within the detection limits of the spectrometer the removal of calcium has no effects on the bilayers. An increase in integration time to 240 s allowed the recording of more distinct spectra as can be seen in Fig. 3.9 showing spectra of

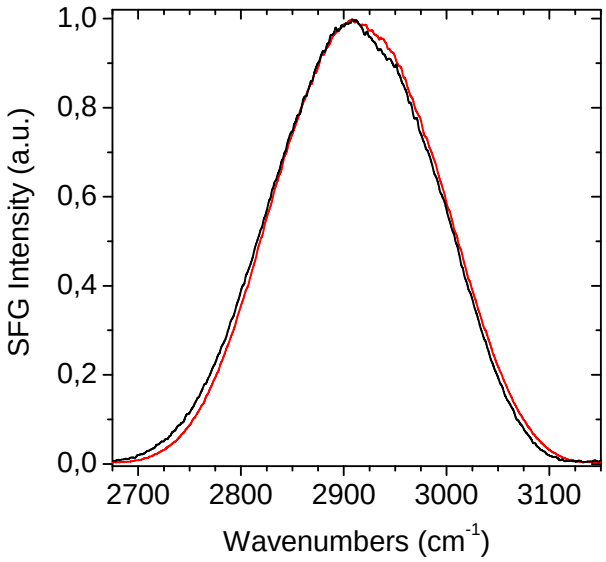

(a) Spectra including non-resonant background. For convenience spectra have been normalized.

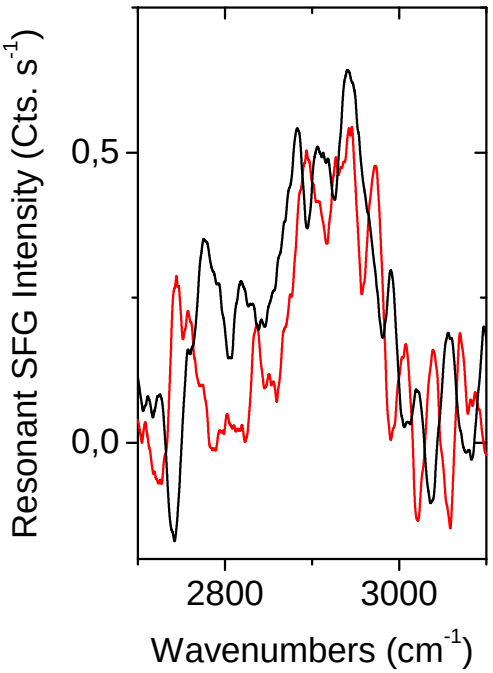

(b) Background-suppressed spectra, normalized to counts per second.

Figure 3.8: Spectra recorded from POPC:POPG 1:1 lipid bilayers, in a Tris/Ca buffer (red) and a Tris buffer without Ca (black).

POPC:POPG 1:1 bilayers produced with Ca/Tris buffer. The spectra though were recorded on two different days demonstrating the reproducibility of the results. The spectra were fitted with Lorentzian functions with a width of 25 cm^{-1} each. Two bands were determined at 2897 cm^{-1} and 2950 cm^{-1} which can be attributed to the symmetric CH_3 stretching mode and Fermi resonance, respectively. These bands are suited as markers to confirm the successful lipid bilayer formation.

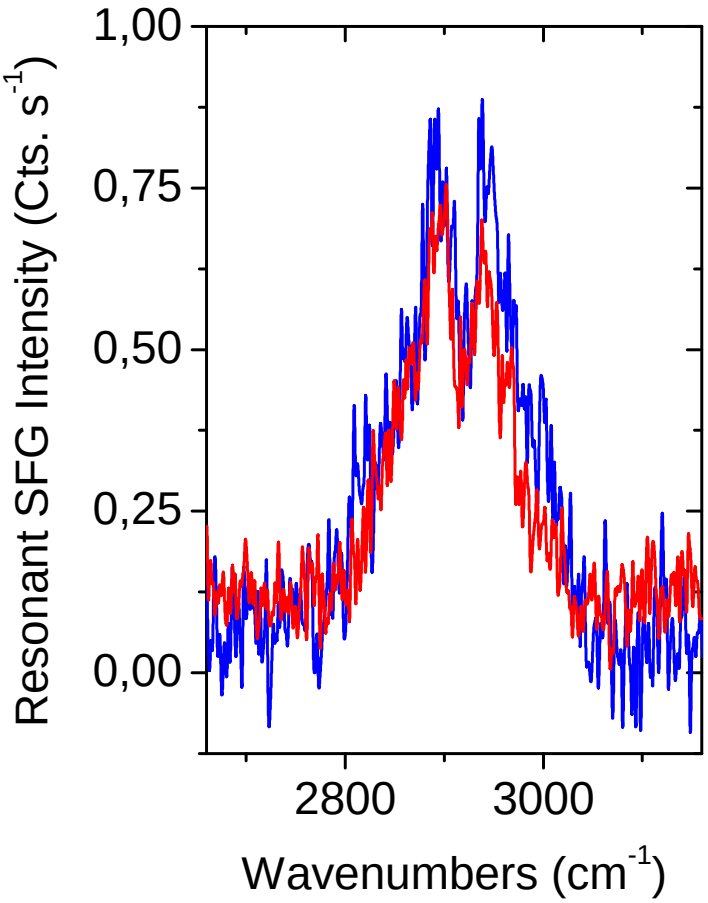

Figure 3.9: SFG spectra recorded in the background-suppressed mode and normalized to counts per second. The spectra were acquired on two subsequent days to demonstrate their reproducibility. The blue spectrum was recorded on day 1 and the red spectrum on day 2.

In order to exclusively detect bands emanating from the AHL molecules allowing an exact determination of their orientation, the AHLs were tested in a deuterated form.

Thus in present experiments it is necessary to change to a spectral region in which C-D vibrations are located. In the course of these experiments it was surprisingly observed that a band evolves over time at 2100 cm^{-1} (see Fig. 3.10). The appearance of this band is neither dependent on the employed lipid composition nor on the incorporation of AHL. Notably the band only evolves when the infrared laser beam is present. The visible laser does not lead to a development of this particular band. Moreover, the same band can be detected if only Ca/Tris buffer is added to a SiO_2 crystal as can be seen from Fig. 3.11(a). Figure 3.11(b) shows a background-suppressed SFG spectra of Ca/Tris buffer on a gold substrate. As it does not show any signs of a band, the band at 2100 cm^{-1} supposedly arises from Tris binding to the SiO_2 substrate over its OH groups. The energy provided by the infrared laser beam apparently leads to a bond similar to the binding of 3-aminopropyl-trimethylethoxy-silane to SiO_2. This assumption is strengthened by the fact that vibrations of nitrogen groups are located in this spectral region. These functional groups can for instance be found in the Tris molecule.

The finding of this particular band motivated us to wash the crystals with PBS instead of lipid-free Ca/Tris buffer after lipid bilayer formation as described in section 2.3. Hence all bilayers prepared for the incorporation of AHL were washed with PBS. The same applies for every wash to remove excess AHL.

3.4.2 Integration of AHL into SLB

If acylated homoserine lactones integrate into a lipid bilayer they are supposed to be oriented. In this case they do not possess a centrosymmetric conformation and would then, according to theory, give rise to an SFG signal. In addition the AHLs are deuterated preventing an overlap of AHL bands with bilayer markers, thus the AHLs are expected to generate high and distinctive spectral signals. This section describes the findings concerning AHL incorporation into model membranes i.e. POPC:POPG 1:1 supported lipid bilayers. As previously explained all supported lipid bilayers in the following experiments were produced with a subsequent PBS wash to remove tris(hydroxymethyl)aminomethane or simply Tris. Moreover, excess AHL solution was as well removed with a subsequent PBS wash after allowing its integration for about 10 mins.

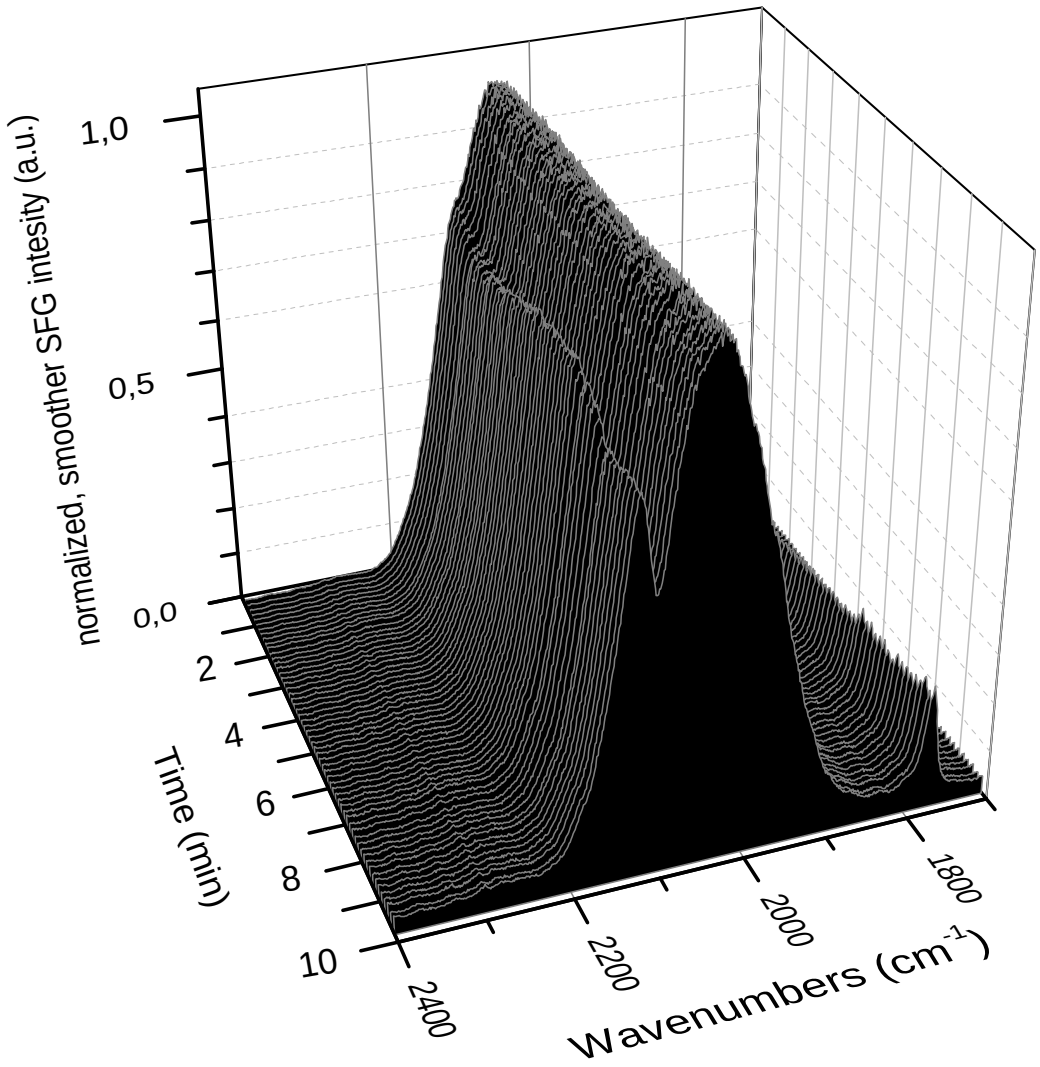

Figure 3.10: This 3D graph shows a POPC:POPG 1:1 lipid bilayer on a SiO_2-coated QCM-D crystal. In the course of the experiment a band developing at 2100 cm^{-1} was detected and followed for 10 mins. For clarity the SFG intensity was normalized to one. The intensity of the band reaches a plateau after about 8 mins

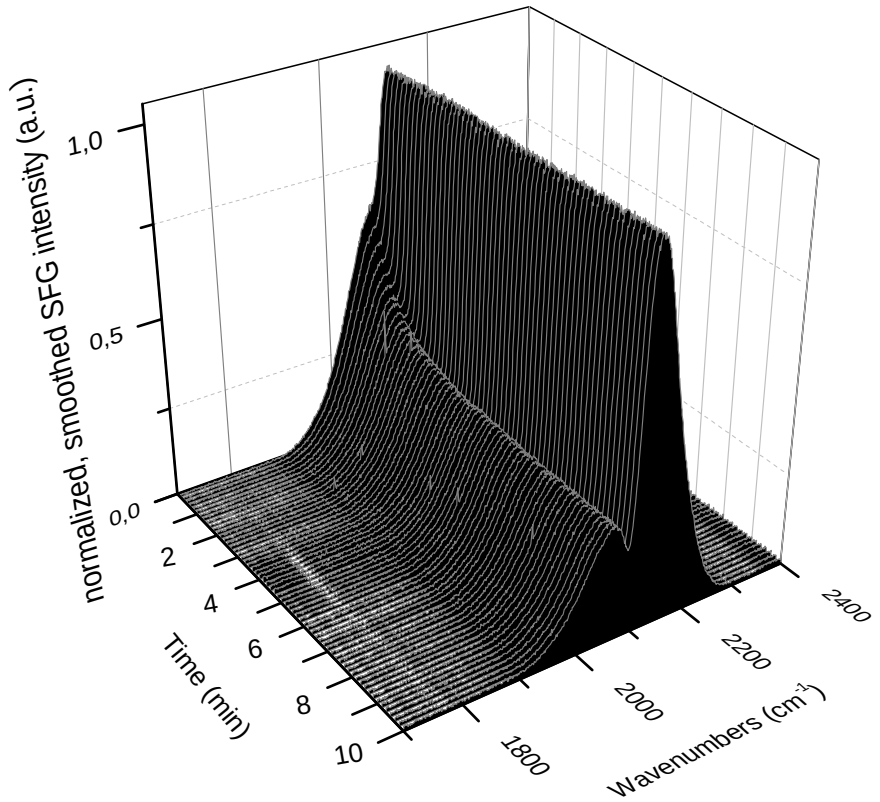

(a) Development of a band at 2100 cm^{-1} on a SiO_2-coated QCM-D crystal with pure Ca/Tris buffer.

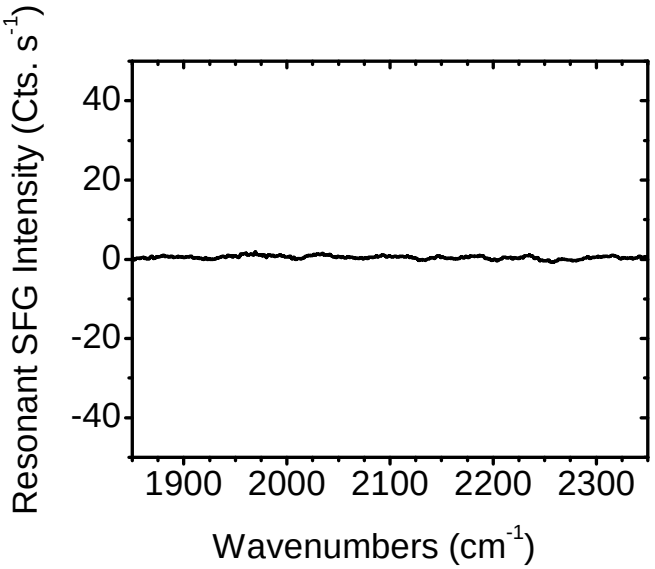

(b) Ca/Tris buffer on a gold substrate. After at least 10 mins of laser exposure no indications of a band are visible.

Figure 3.11: The spectra recorded from pure Ca/Tris buffer showed in (a) the development of a band on SiO_2-coated QCM-D crystals and no band on gold wafers (b).

All supported lipid bilayers employed in the SFG measurements have been produced according to the procedure described in section 2.3. In order to confirm the formation of such a bilayer recordings in the spectral CH stretching region were performed. These findings will not be repeated here as they have been thoroughly described in the previous section (3.4.1). If the bilayer specific bands in the CH region could not be detected the measurement was stopped immediately and restarted.

The experiments involved homoserine lactones with different aliphatic chain lengths of 4, 8 and 10 carbons denoted by D-9, D-17 and D-21 at a concentration of 1.0 mg/mL (for details see section 2.8). Figure 3.12 depicts the normal and background-suppressed spectra of the three lactones. In the normal spectra apparently two dips are visible. However, the background-suppressed spectra (Fig. 3.12(b)) shows that those two dips are actually one real dip i.e. a band with a phase difference to the background of about 0° and two peaks i.e. bands with a phase difference of about 180° forming a dip-like signal. The normal SFG spectrum was fit as described in section 2.1.4 which is shown exemplarily for D-17 in Fig. 3.13. Detailed peak positions and widths can be determined by fitting the obtained resonant contributions with Lorentzian curves. For D-17 the positions were found to be located at 2148 cm^{-1}, 2204 cm^{-1} and 2247 cm^{-1} and can be assigned to an antisymmetric stretching mode of deuterated methylene, the respective Fermi resonance and the CD_3 antisymmetric stretching vibration, respectively [100]. In Tab. 3.1 the results of the fits for the investigated AHLs with different chain length are summarized including positions, assignments and phases. The phases of the three different AHLs are rather similar. This indicates that their orientations within the lipid bilayer may be similar as well. The assigned phases of the Fermi resonances though are rather arbitrary as a Fermi resonance is an overtone of two vibrational modes and thus no phase can be assigned to this mode. Moreover, the phases determined for the asymmetric methyl stretching vibration are close to 180°. A phase of about 0° corresponds to a functional group oriented away from the substrate as can be seen from the observed phases of the subsequently investigated SAMs (Sec. 4.3). Conversely, a phase of approximately 180° is related to a functional group pointing to a certain extent towards the surface as has been shown by Bain et al. in 1993 [66]. Thus the vibration, i.e. the associated transition dipole moment, of methyl must be facing towards the gold substrate at a certain angle. Hence the AHL must be located in the upper leaflet of the bilayer. While the two longer AHLs present rather strong bands indicating that

the majority of their functional groups are oriented similarly, the low intensity of the D-9 bands suggests that the orientation of its functional groups is distributed more randomly as it has more space to move freely. Another possible explanation would be that less D-9 molecules have integrated into the bilayer which can be explained with a changed ratio of hydrophobic to hydrophilic parts making it less favorable to leave the aqueous solution.

AHL	Position (cm^{-1})	Assignment	Width (cm^{-1})	Phase (°)
D-17	2148	CD_3 FR	37	0
	2204	CD_2 asym.	17	119
	2247	CD_3 asym.	18	146
D-21	2146	CD_3 FR	31	0
	2207	CD_2 asym.	23	116
	2244	CD_3 asym.	26	132
D-9	2184	CD_3 FR	34	1
	2206	CD_2 asym.	14	122
	2244	CD_3 asym.	15	130

Table 3.1: C-D vibrational stretching modes of the deuterated AHLs as shown in Fig. 3.12. Positions are denoted as fitted with the function described in section 2.1.4. The assignments are taken from [100].

3.5 SFG time series study of AHL incorporation

As already explained in the introduction, AHLs supposedly flip through eukaryotic and prokaryotic cell membranes in order to initiate cellular responses by binding to an intracellular receptor. However, there is also the evidence of an existing membrane receptor. In order to confirm one of the two possibilities it is necessary to elucidate whether AHLs can penetrate biological membranes in a flipping process or not. Hence a time series experiment was performed for more than 5 hours in order to detect changes in the SFG signal which might indicate such a phenomenon.

In a first approach AHLs of all three chain lengths were allowed to integrate in the supported POPC:POPG bilayer for ten minutes as already explained. Subsequent to a PBS wash the SFG experiments started after the assembly of the TLA cell. Due to its

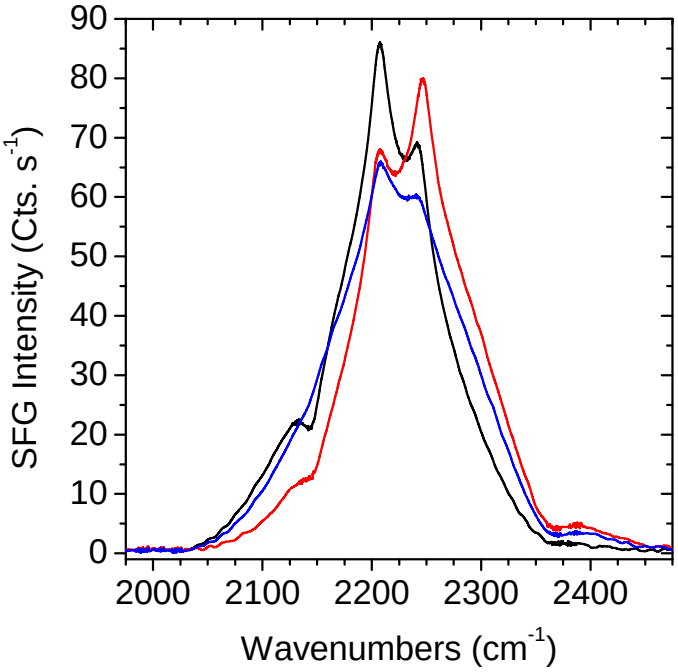

(a) Normal SFG spectra

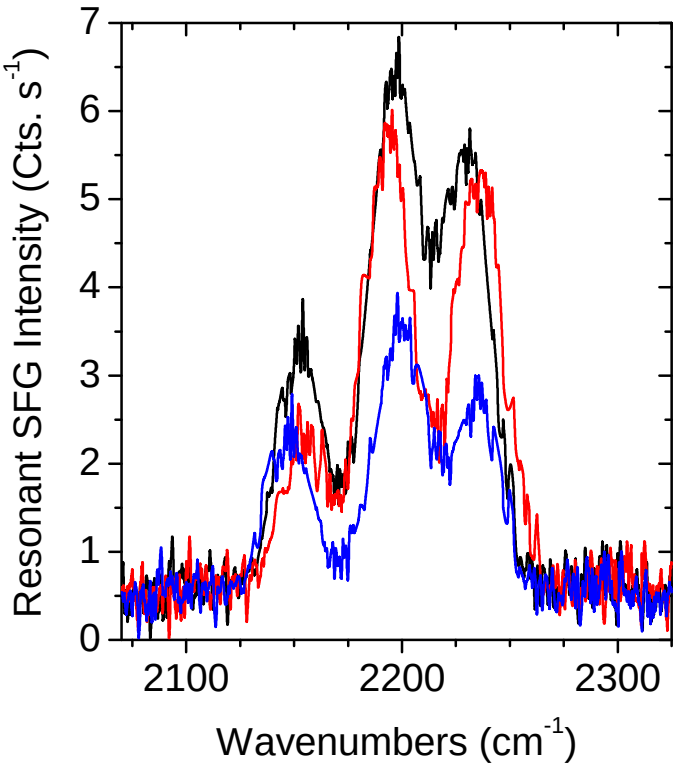

(b) Background-suppressed SFG spectra

Figure 3.12: SFG spectra of the deuterated N-acyl-L-homoserine lactones D-21, D-17 and D-9 in black, red and blue, respectively.

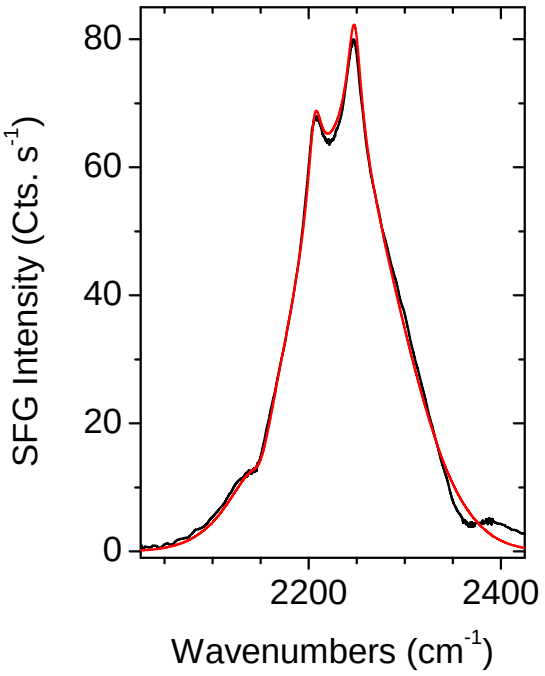

(a) Original spectrum including the best fit in red

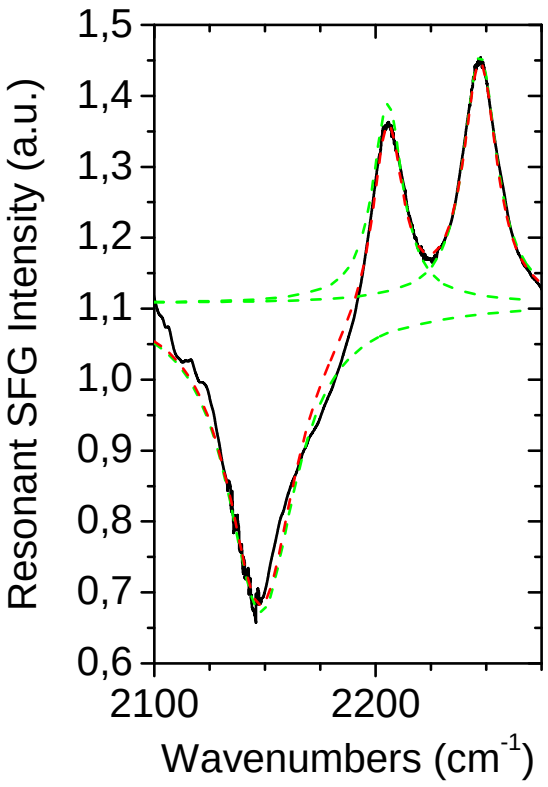

(b) Resonant contributions

Figure 3.13: For the deuterated homoserine lactone D-17, (a) shows the fitted original spectrum and (b) the resonant contributions calculated as described in section 2.1.4 including a fit with 3 Lorentzian curves (green) and its cumulative curve (red).

long aliphatic chain D-21 possesses the greatest similarity to phospholipids, thus it was assumed to possess the highest flipping rate. Conversely, this would result in the largest change of the signal intensity. Therefore the time series experiments started with this AHL. The recorded SFG signal consisted of nonresonant and resonant contributions as shown in Fig. 3.14(a) for D-21. A comparison of the first spectrum (black) and the spectrum recorded after 5.25 hrs (red) shows no substantial difference between both spectra. Furthermore, a comparison of the resonant contributions calculated from the fitted spectra turned out to be rather difficult and produced no reliable results.

Hence in the final time series experiments of all three investigated AHLs it was worked solely with background-suppression. Graphs of the initial spectrum and of the spectrum after 5 hrs recording time are exemplarily depicted for D-21 in Fig. 3.14(b) in black and red, respectively. Though the changes are subtle and hidden in the noise, it is possible to find a decrease in band intensities. However, due to the noise simply using the maximum as a measure of the band intensity is not reliable or impossible for the signal of D-9 as can be seen from Fig. 3.15(a) where the intensities in ratios of the initial intensity is depicted against the time points of recording. By fitting the spectra with three Lorentzian functions it is possible to circumvent this obstacle and obtain overall band intensities. For D-21 such a fitted spectrum at t = 0 hrs. is depicted in Fig. 3.15(b) with the single Lorentzia in green and their sum in red. The AHLs of different chain length D-17 and D-9 were investigated similarly. The obtained integrated intensities were added and are plotted in Fig. 3.16(a) as triangles. By comparing these results with graph 3.15(a) a significant improvement in signal stability can be observed. With this in mind the integrated intensity can be used as a measure of the AHL population difference. This generated SFG signal is directly proportional to the population difference

$$I \propto (N_U - N_L)^2 \tag{3.1}$$

with N_U and N_L denoting the numbers of AHL molecules in the upper and lower leaflet. Following Conboy's reasoning the process of a potential AHL flip-flop was assumed to be unimolecular with an equal and time independent rate constant k [34]. When at the start of the experiment $N_U = 1$ and $N_L = 0$ the first time derivative of the lower leaflet's population can be written as

$$\frac{dN_L}{dt} = kN_U - kN_L = -k(2N_L - 1) \tag{3.2}$$

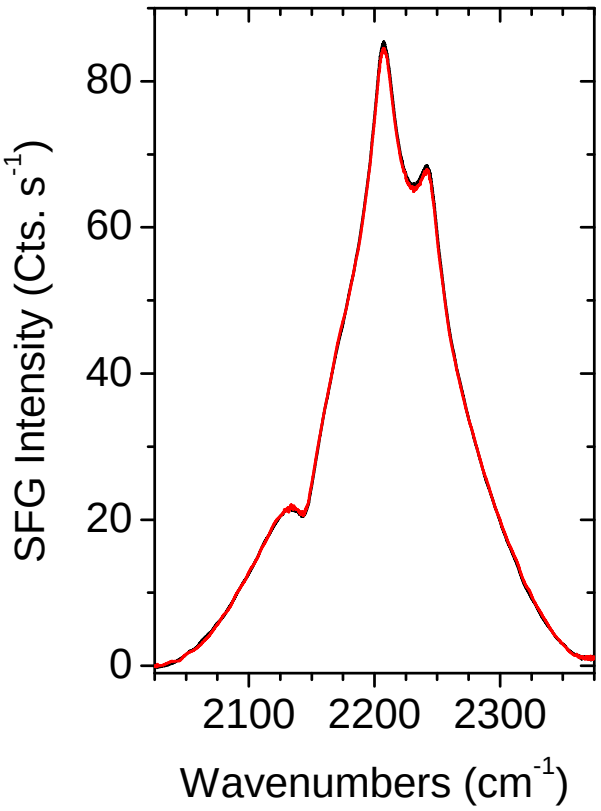

(a) Normal SFG spectra

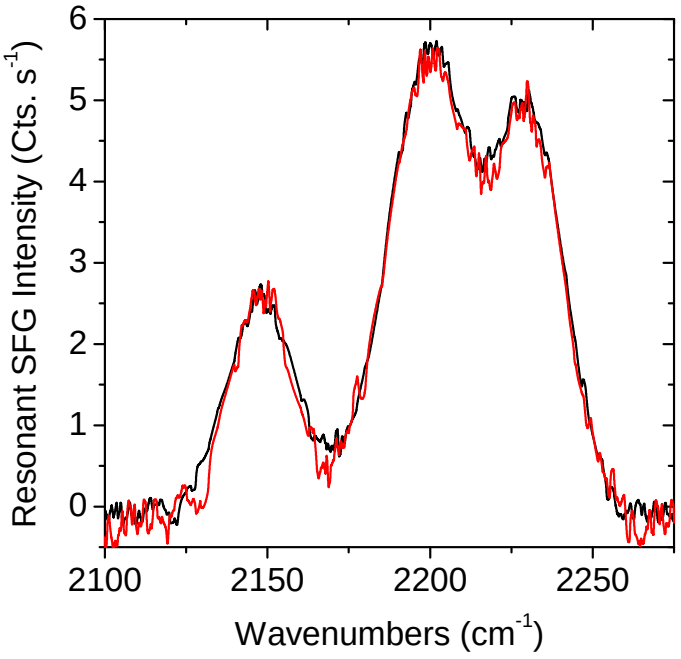

(b) Background-suppressed SFG spectra

Figure 3.14: The black curve depicts the initial and the red curve the final time series spectrum for D-21.

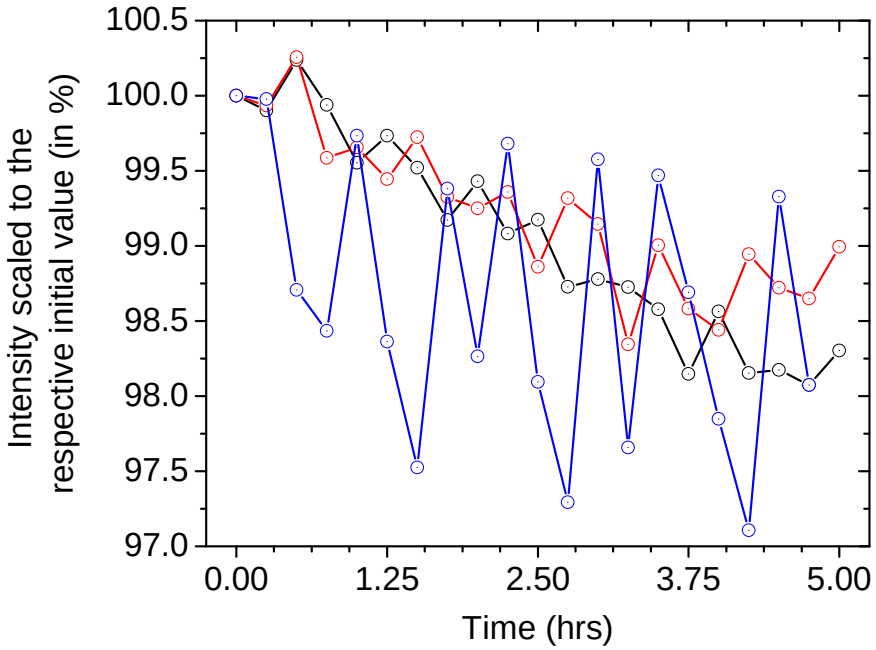

(a) Maximum intensity of background-suppressed D-21, D-17 and D-9 spectra in black, red and blue depicted versus time point of recording. Lines are guides for the eyes.

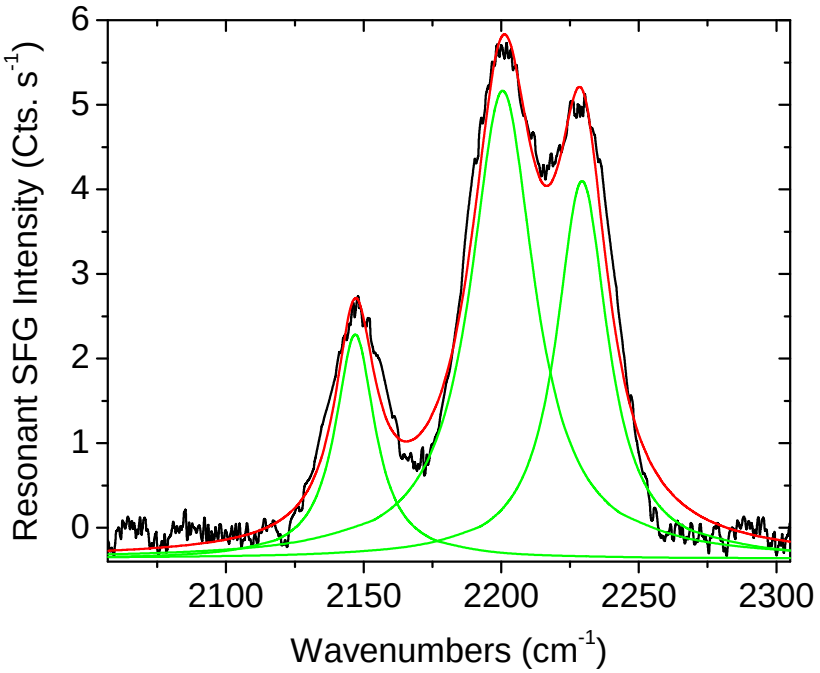

(b) Fitted initial background-suppressed spectrum of D-21, green: single Lorentzia, red: sum

Figure 3.15: (a) Course of the maximum intensity. (b) Fitting results for the background-suppressed spectrum of D-21.

Integrating the above expression and introducing it into Eq. 3.1 yields the following proportionality

$$I \propto \exp(-4kt) \tag{3.3}$$

The half life of the AHL flip flop process can then be determined according to

$$T_{1/2} = \frac{\ln 2}{2k} \tag{3.4}$$

Fitting the data for D-21 and D-17 AHLs with Eq. 3.3 yields good results for the decay constant k as can be seen from the small error. However, the fit for D-9 is difficult and the obtained value possesses a relative error of 36 %. Therefore the derived half time $T_{1/2}$ is not reliable either. Nevertheless, all three half times have the tendency to increase with decreasing chain length. This phenomenon can be explained as follows. When the AHLs have a high chain length comparable to the phospholipids it is energetically favorable for them to integrate into the lipid bilayer in a well-ordered manner. For the flipping they have to overcome a certain energy barrier which is for the long chain AHLs not as high as for the short chain AHLs. This explains the increase in flipping time from D-21 to D-17. However, the surge from 17.4 days to 112.5 days for D-9 is too high to be attributable to the shorter chain length. The absolute error of 40.1 days as well as the stable SFG signal indicate that it is more likely that D-9 does not flip at all through the lipid bilayer. The calculated value might arise from noise or a degradation process occurring after 5 hrs. On the other hand flip-flop half times on the order of days instead of hours are considered as not relevant for a signaling molecule. The flipping might be an additional process possible in nature, however due to tge high flipping time this process cannot be regarded as a useful pathway for the signaling in biofilms. Overall, the findings of AHLs integrating into a model lipid bilayer as well as the indications of a flip flop process provide another piece in the puzzle of how bacteria can communicate within a biofilm and also with their eukaryotic hosts.

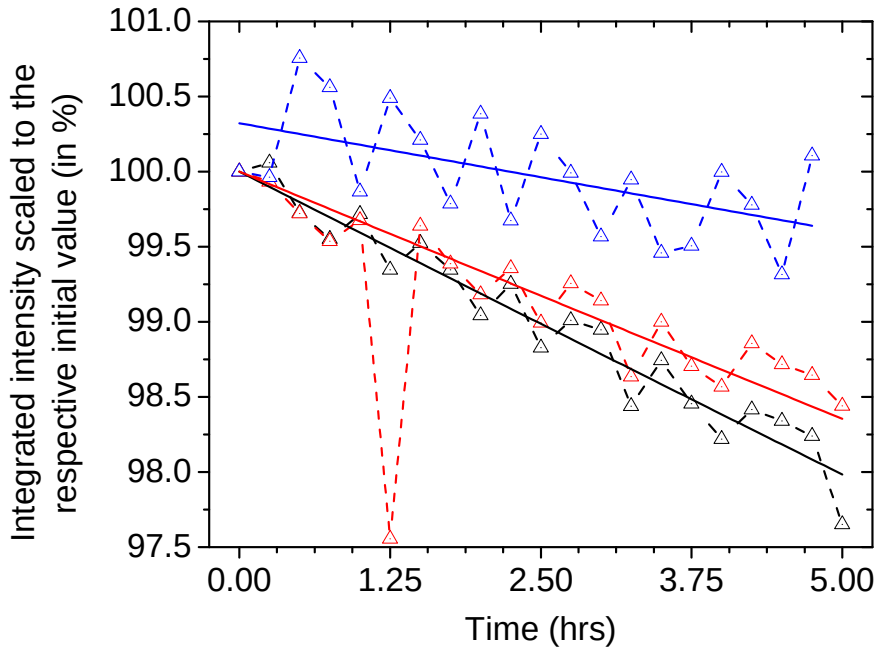

(a) Integrated band intensities of the background-suppressed spectra for D-21, D-17 and D-9 in black, red and blue, respectively. Values are scaled to their initial intensities. Dotted lines are guides for the eyes. Full lines are exponential fits according to the text.

AHL	**Decay constant k (10^{-4})**	**Half time $T_{1/2}$ (days)**
D-21	2.546 ± 0.076	14.2 ± 0.4
D-17	2.074 ± 0.023	17.4 ± 0.2
D-9	0.901 ± 0.321	112.5 ± 40.1

(b) Time decay constant obtained from fits according to the text, the related half time and their respective errors.

Figure 3.16: Results of the time lapse experiments for all three investigated AHLs with different chain length D-21, D-17 and D-9.

4

The investigation of differently terminated self-assembled monolayers

In this chapter SAMs with different terminal groups are studied in air and *in situ* with sum-frequency generation spectroscopy. The focus lies particularly on structural changes within the SAMs when exposed to water. In the second half of the chapter pyridine-terminated SAMs will be studied in a combined electrochemistry and sum-frequency generation experiment. Herein, structural changes occurring upon desorption from the substrate are of special interest. Moreover, nonlinear optical effects of third order will be considered in detail.

4.1 Infrared reflection absorption spectroscopy

After the SAMs had been prepared according to section 2.6 their successful formation was verified with an independent technique. For this purpose infrared reflection absorption spectroscopy (IRRAS) was used. It is dedicated for the analysis of surface composition. Moreover, in combination with Raman spectroscopy, IRRAS can be used to find suitable SFG-active bands.

Figure 4.1 shows the results for the IRRAS measurements of DDT, AUT, MUA and MHA on gold in the CH stretching region (from bottom to top). The positions of the bands as well as their assignments are listed in Tab. 4.1. MHA (in blue) does not

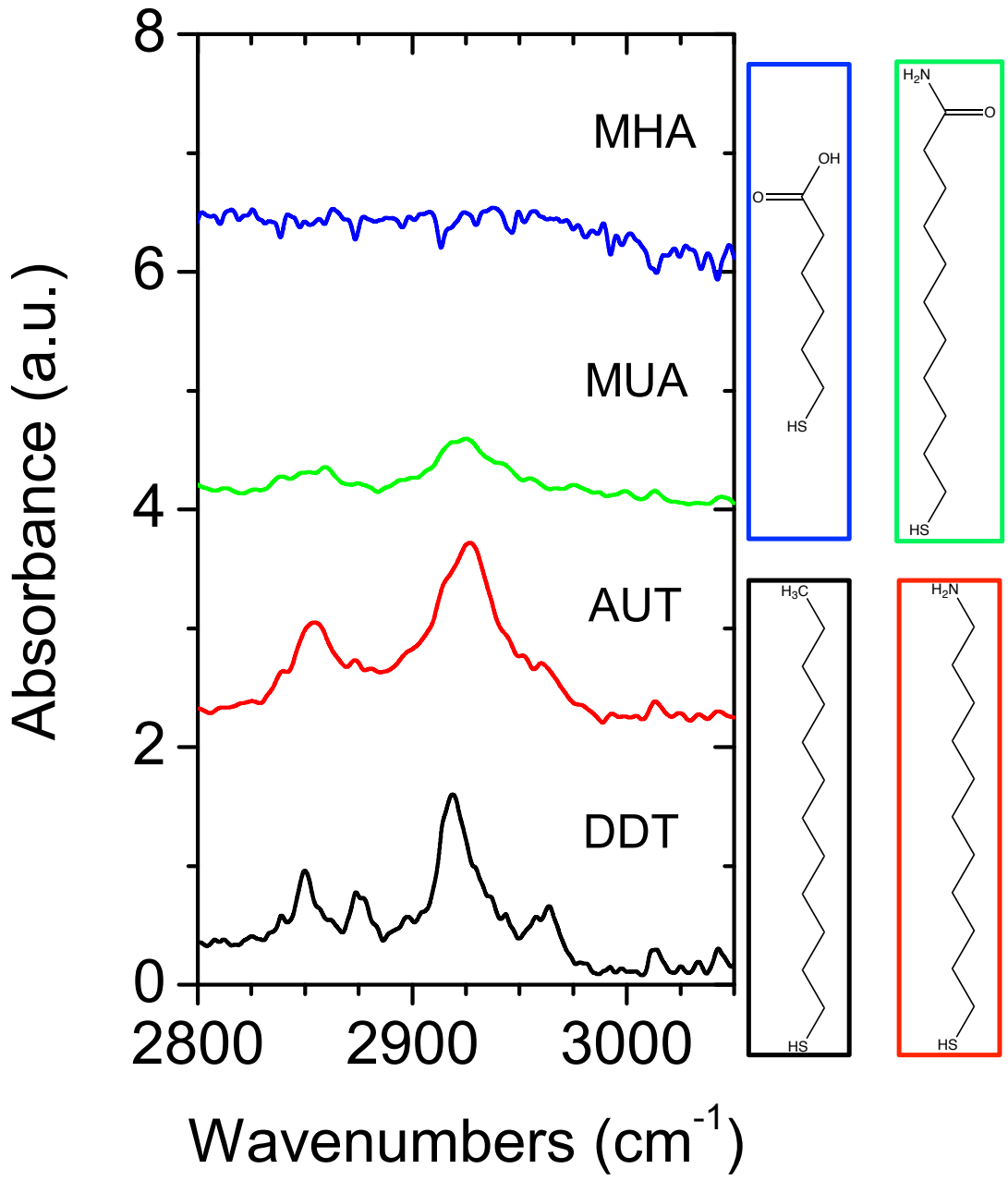

Figure 4.1: This figure shows the spectral CH stretching region for the different SAMs on gold. DDT is shown in black, AUT in red, MUA in green and MHA in blue. DDT exhibits more distinct bands in this region at about 2850 cm^{-1} and 2950 cm^{-1} whereas AUT and MUA only show two broad features at these two wavenumbers. MHA does not show any bands at all.

show any features at all in the IRRAS measurements, nevertheless the SAM formation did work as could be shown with an additional XPS measurement as well as with the presented SFG experiments. Its vanishing IR activity might be due to 40 % less carbon bonds as the MHA comprises a carbon chain with only six atoms. In contrast, DDT depicted in black exhibits on the one hand more and on the other hand more distinct bands in this region than the two other SAMs. Their CH stretching bands are rather broad features and are hence more difficult to assign. In Fig. 4.2(a) the spectral amide region of the investigated SAMs is shown. Only the hydrophilic MUA presents bands at 1610 cm^{-1} and 1668 cm^{-1}. The two bands originating from the amide termination can be assigned to the N-H and C=O stretching vibrations, respectively. Figure 4.2(b) demonstrates how the high hydrophilicity of a SAM can be shown with infrared spectroscopy. The two bands at 2335 cm^{-1} and 2363 cm^{-1} originate from gaseous carbon dioxide (red spectrum) and have already vanished (black spectrum) whereas the bands attributable to ambient water vapor are still present (black spectrum, left hand side). The water vapor bands do eventually vanish several minutes later and the bands arising from the SAM can be clearly observed (red spectrum). This effect indicates that the MUA is so hydrophilic that H_2O molecules adsorb to the surface and start to desorb only when the ambient H_2O concentration drops significantly due to constant nitrogen purging.

Assignment	**DDT**	**AUT**	**MUA**
methyl asym. (ip)	2964 cm^{-1}	–	–
methyl asym. (op)	2957 cm^{-1}	–	–
methyl FR	2932 cm^{-1}	–	–
methyl sym.	2875 cm^{-1}	–	–
methylene asym.	2919 cm^{-1}	2924 cm^{-1}	2926 cm^{-1}
methylene FR	2898 cm^{-1}	2895 cm^{-1}	2900 cm^{-1}
methylene sym.	2849 cm^{-1}	2853 cm^{-1} b	2850 cm^{-1} b

Table 4.1: Band assignments for the obtained infrared spectra of the investigated alkanethiols based on [4][5][6][7]. Abbreviations: sym: symmetric, asym: asymmetric, FR: Fermi resonance, ip: in-plane, op: out-of-plane, b: broad.

The low spectral position of the asymmetric methylene stretching band of DDT indicates that this SAM forms a well-ordered film on the gold substrates. In contrast

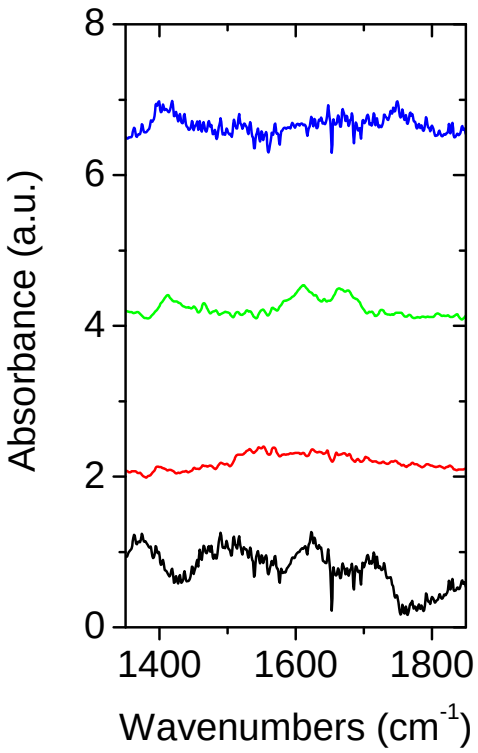

(a) This figure shows the spectral amide region for the investigated SAMs on gold. DDT, AUT and MHA (in black, red and blue) do not show any bands in this region. The only SAM exhibiting two distinct bands at 1610 cm^{-1} and 1668 cm^{-1} is MUA terminated with an amide group ($CONH_2$, in green).

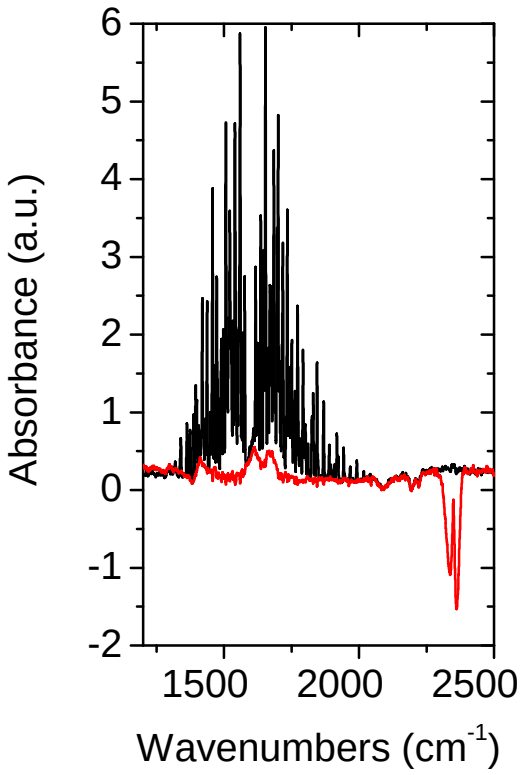

(b) This graph illustrates the high hydrophilicity of MUA. In contrast to the already vanishing CO_2 bands on the right hand side, the bands originating from water vapor are still present in the black spectrum on the left hand side. Several minutes later indicated by the overcompensated CO_2 bands, the water vapor has vanished due to constant nitrogen purging.

Figure 4.2: IRRA spectra in amide region. (b) illustrates the wettability of an amide-terminated gold surface.

the order of the amine-terminated AUT and the amide-terminated MUA is lower as the spectral position of this band lies at higher wavenumbers [101]. However, MHA possessing a chain of only 6 carbon atoms does not show any features in the CH and amide regions. Nevertheless, the formation of the SAM did work as will be demonstrated with subsequent SFG data. Furthermore, MUA is sufficiently hydrophilic to attract H_2O molecules from the ambient water vapor and maintain the adsorption until the water vapor concentration drops significantly. In the subsequent sections these SAMs will be thoroughly investigated with sum-frequency generation spectroscopy in air and *in situ*.

4.2 Contact Angle Measurements

To determine the degree of hydrophilicity of the investigated SAMs measurements of the water contact angle had been performed. Figure 4.3 shows examplarily three images used to determine the water contact angles of the respective SAMs. The contact angle of AUT is moderately below the value of 90° marking the border to hydrophobicity. However, MHA and especially MUA are very hydrophilic as can be seen from the wide spread water droplets and their rather low contact angles of 15.5° and 9.8°, respectively. The high hydrophilicity of MHA and MUA marked them both as good candidates to tailor the supports for lipid bilayer formation. However, it turned out that MHA was a more reliable choice regarding the formation and stability of supported lipid bilayers.

4.3 Sum-frequency generation spectroscopy

With its high sensitivity and surface-specificity sum-frequency generation spectroscopy does not only allow the investigation of interfacial molecules at low densities, but the investigation of effects of aqueous solutions upon those molecules *in situ*. It is especially dedicated for the analysis of SAMs with different terminal groups as will be demonstrated here for aminoundecane thiol (AUT), mercaptoundecane amide (MUA), mercaptohexanoic acid (MHA) and dodecane thiol (DDT). Furthermore, a precise analysis of the recorded spectra allows the determination of the orientation of various functional groups within the investigated SAMs allowing to draw conclusions on the overall SAM conformation.

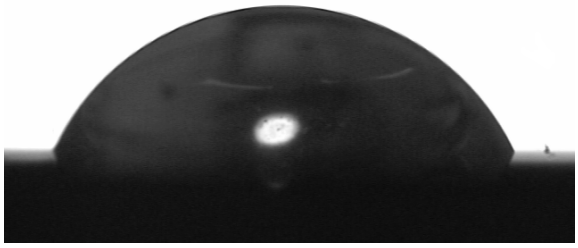

(a) AUT; 65.0°

(b) MUA; 9.8°

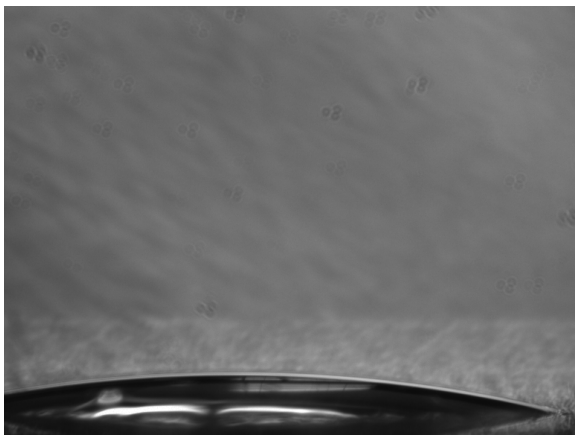

(c) MHA; 15.5°

Figure 4.3: These figures show exemplary images of the investigated SAMs with a water droplet. Numbers indicate the determined water contact angle.

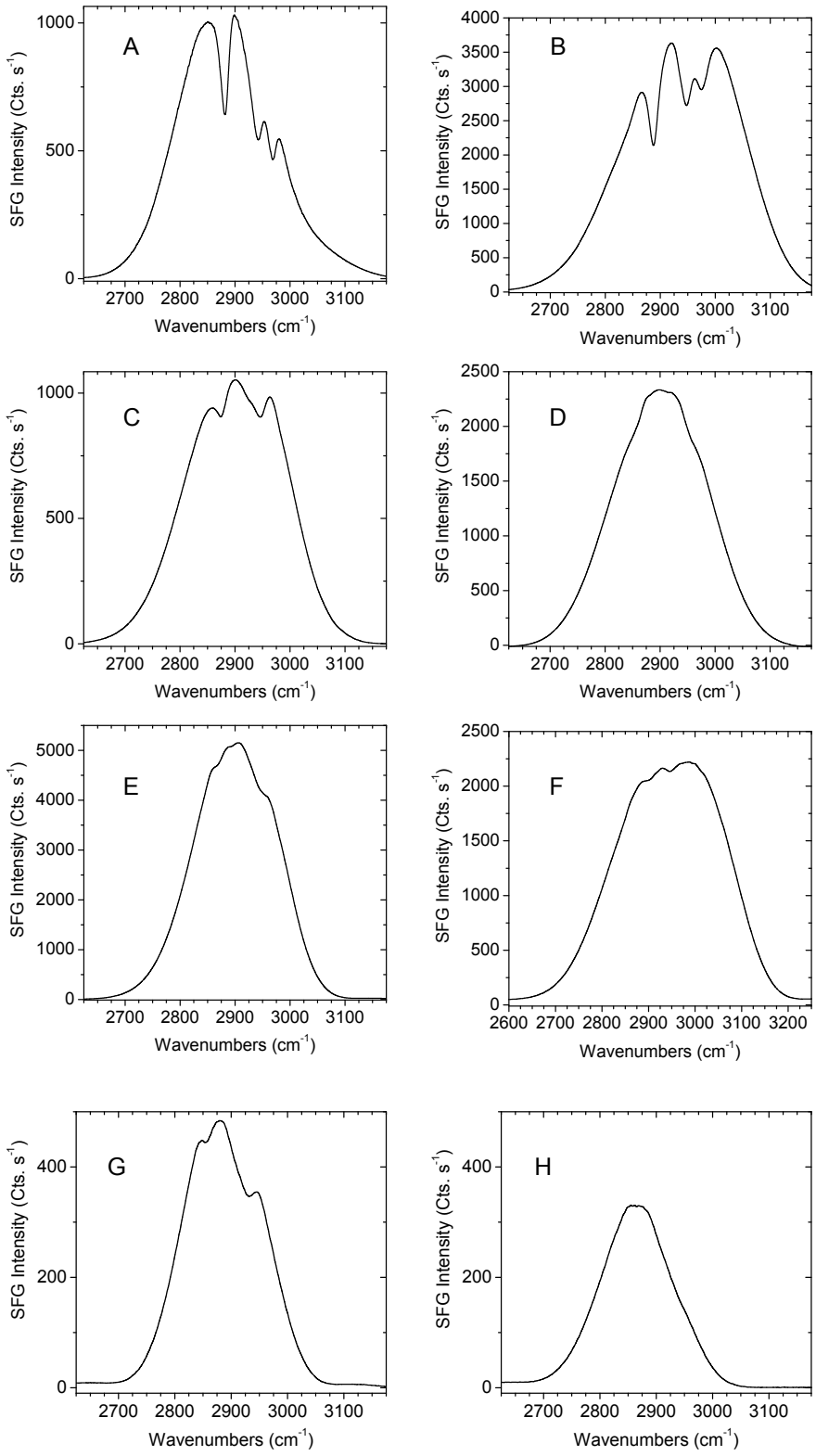

Figure 4.4: These figures show the spectral C-H stretching region for SAMs on gold. A and B show DDT spectra in air and *in situ*, respectively. C and D depict the spectra of AUT in air and liquid, whereas E and F show the respective spectra for MUA and G and H for MHA.

Figure 4.4 shows an overview of the recorded SFG spectra including the nonresonant background originating from the gold substrate. As described in section 2.1.4 in addition to these raw spectra background-suppressed spectra were recorded. From those spectra the band positions were deduced and fed into the desribed fitting routine with which the raw spectra were fit and both the phases and amplitudes of the bands could be determined. Rough conclusions on the behavior of the SAMs when exposed to liquid can also be drawn by considering only the recorded raw spectra. DDT for instance is a SAM with a hydrophobic terminal group. Thus its structure does not significantly change upon exposure to water as can be seen from the still distinct bands in the nonresonant background (A & B). In contrast, AUT exhibits only small bands emanating from CH_2 groups which possess a smaller dipole moment as compared to the CH_3 vibrations of DDT. When exposed to liquid the bands vanish almost completely indicating that the structure of AUT is disturbed (C & D). MUA also possesses only relatively small CH_2 bands as compared to AUT which is a sign for a low overall structural orientation of the respective methylene groups. However, upon exposure to water it apparently maintains its structure as the intensities of the SFG active bands change only slightly (E & F). In contrast, the order of MHA is completely disturbed as there are no more bands present in the raw SFG spectrum when it is exposed to liquid (G & H).

The results of the fitting procedure can be obtained from Tab. 4.2. For each SAM several measurements and analyses were performed showing comparable, hence reliable, results for the recordings in air. However, the results obtained for SAMs in liquid must be considered with caution as they were quite ambivalent. The table presents average values for spectral position and phase. For DDT it can be inferred that when exposed to water no essential changes occur as was already concluded from the raw spectra. However, the unchanged phases moreover indicate that the orientation of the methyl and methylene groups did not change in water [66]. Surprisingly, the orientation of AUT functional groups did change only slightly, even though the overall band intensity decreased which must be interpreted as a net loss of net orientation due to water affecting the terminal amine group and the first adjacent methylene groups.

The MUA is a SAM which is particularly interesting to study. Although this SAM did form as expected, proven by the IRRAS data, its structure with respect to the net orientation is not at all comparable with the two previous SAMs. MUA only

SAM	Position	Assignment	Width	Phase
DDT	2860 cm^{-1}	CH_2 s [101]	12.8 cm^{-1}	0°
in air	2875 cm^{-1}	CH_3 s [4]	16.0 cm^{-1}	0°
	2920 cm^{-1}	CH_2 as [101]	16.7 cm^{-1}	0°
	2942 cm^{-1}	CH_3 FR s	12.1 cm^{-1}	0°
	2952 cm^{-1}	CH_3 as [4]	14.0 cm^{-1}	0°
DDT	2859 cm^{-1}	CH_2 s [4]	23.0 cm^{-1}	28°
in H_2O	2863 cm^{-1}	CH_2(2) s [4]	13.3 cm^{-1}	0°
	2921 cm^{-1}	CH_2(2) as	19.6 cm^{-1}	0°
	2950 cm^{-1}	CH_3 as	13.3 cm^{-1}	0°
AUT	2852 cm^{-1}	CH_2 s [39]	26.0 cm^{-1}	0°
in air	2865 cm^{-1}	CH_2 (2) s	20.4 cm^{-1}	0°
	2879 cm^{-1}	CH_2 - S s	20.6 cm^{-1}	11°
	2906 cm^{-1}	CH_2 FR s [40]	20.3 cm^{-1}	10°
	2931 cm^{-1}	CH_2 - S as	14.9 cm^{-1}	3°
	2949 cm^{-1}	CH_2 gauche	20.7 cm^{-1}	0°
AUT	2851 cm^{-1}	CH_2 s [39]	18.4 cm^{-1}	0°
in H_2O	2902 cm^{-1}	CH_2 FR s [40]	20.2 cm^{-1}	0°
	2948 cm^{-1}	CH_2 gauche	17.9 cm^{-1}	0°
MUA	2851 cm^{-1}	CH_2 s [39]	15.9 cm^{-1}	–
in air	2924 cm^{-1}	CH_2 as [40]	10.5 cm^{-1}	–
	2954 cm^{-1}	CH_2 gauche	16.0 cm^{-1}	–
	2967 cm^{-1}	NH_3^+ [102]	17.0 cm^{-1}	–
	2992 cm^{-1}	NH_2 [102]	16.0cm^{-1}	–
MUA	2870 cm^{-1}	CH_2(2) s [33]	30.0 cm^{-1}	–
in H_2O	2930 cm^{-1}	CH_2(2) as [4]	30.0 cm^{-1}	–
	2946 cm^{-1}	CH_2 gauche	22.0 cm^{-1}	–
	2969 cm^{-1}	NH_3^+ [102]	30.0 cm^{-1}	–
	2984 cm^{-1}	NH_2 [102]	30.0cm^{-1}	–
MHA	2855 cm^{-1}	CH_2 s	25.0 cm^{-1}	0°
in air	2905 cm^{-1}	CH_2 FR s [40]	30.0 cm^{-1}	0°
	2930 cm^{-1}	CH_2 as [40]	28.0 cm^{-1}	0°

Table 4.2: Where not stated differently the assignments are taken from Howell et al [8], used abbreviations: s: symmetric, as: asymmetric, FR: Fermi resonance, ip: in-plane.

shows very weak CH_2 stretching bands. Furthermore, the phase determination showed a high variability. Therefore the reliability was not ensured and it will be refrained from giving any calculated phases. This finding indicates that the amide group may inhibit the formation of a densely packed and well-ordered film which in turn does not allow the SF signal generation. In combination with the comparably low band intensity in air and liquid this indicates that the conformation of the SAM does not essentially change upon exposure to water. Another reason for the already disturbed conformation in air might be that MUA is highly hydrophilic leading to an adsorption of water molecules from the ambient water vapor as could be seen from the purging experiment described for the IRRAS measurements (Sec. 4.1). Upon exposure to water, the polar amide group may then inhibit interact with the water molecules preventing a further structural disturbance of the SAM.

MHA differs from the previously investigated SAMs in an important fact, it possesses a carbon chain that is only six atoms long, in contrast DDT, AUT and MUA have chains that are as twice as long. Even though it is not as hydrophilic as MUA, the intensity of its SFG-active bands is rather similar indicating that functional groups are not well aligned. This finding is in accordance to literature [4]. Due to the bad alignment of the carbon chains its structure is less dense which in turn does not allow strong van der Waals forces between the chains. Hence, when exposed to liquid the water molecules can strongly interact with the hydrophilic end group and disorder the MHA structure. This results in isotropically oriented methylene groups allowing no SF signal generation. Hence no bands can be observed in the spectrum recorded in water.

The performed study of differently terminated SAMs was able to show how the phase determination can provide useful information for the interpretation of SF spectra with respect to structural aspects. It revealed that not only the hydrophilicity is an important factor for the behavior of a SAM upon exposure to water. Also the nature of the terminal group itself has a fundamental influence on the effects of water on the structure. A moderately hydrophilic terminal group usually leads to the destruction of the SAM structure as in the case of AUT [8]. In contrast, the structure of MUA, terminated with the large and highly hydrophilic amide group, does not change upon exposure to water. Furthermore, the study established a measurement procedure for the investigation of SAMs and comparable samples like e.g. supported lipid bilayers or molecules incorporated therein.

4.3.1 Gold related bands in the spectral CO_2 region

The absorption of infrared energy by ambient gaseous CO_2 at 2335 cm^{-1} and 2363 cm^{-1} leads to a diminished excitation of electrons in the gold substrate. This results in a reduced nonresonant background intensity. In deed, in Fig. 4.5 two dips can be observed in the nonresonant background of DDT, AUT, MUA and deuterated DDT in air and *in situ* (black spectra) as less energy remains to excite electrons in the different electronic bands of the gold. Since this phenomenon is purely related to the generation of the nonresonant signal the background-suppressed spectra are not supposed to show any bands. However, in Fig. 4.5 for all SAMs in air and liquid SFG-active bands are present at 2327 cm^{-1} and 2358 cm^{-1}(red spectra). Thus the bands cannot be related to vibrational modes of the SAMs and since they also appear in liquid at the same spectral positions they are not depending on environmental conditions.

To ultimately exclude vibrational modes of functional groups belonging to all SAMs the same recordings were performed with a CaF_2 prism sputtered on one half with 200 nm Au and on the other half coated with titanium dioxide. The 200 nm Au layer is completely reflective not allowing an evanescent wave to leave the layer and potentially pick up molecular information from the surface. The measurements started on the gold-coated side to find an SFG signal and to adjust the spectrometer to the desired spectral region. Normal SFG spectra are depicted in Fig. 4.6 A. Since TiO_2 does not have the same nonresonant SFG activity as gold the recorded (nonresonant) signal from TiO_2 (in red) is orders of magnitudes smaller as can be seen from the higher noise level. In absolute values TiO_2 has a maximum intensity of 1.0 Cts. s^{-1} whereas the maximum intensity of gold is about 602 Cts. s^{-1}. However, in both spectra dips are present where the gaseous CO_2 absorbs parts of the infrared radiation. In contrast, the spectra obtained with background suppression look completely different (Fig. 4.6 B). While the gold spectra still show the previously observed bands supposedly originating from CO_2, the titanium dioxide spectra do not. Since the experimental setup also eliminates the possibility of adsorbed CO_2 on the gold layer potentially contributing to the SFG signal this finding indicates that the bands observed in the background-suppressed spectra are a phenomenon purely related to specific properties of the employed gold layer. One might speculate that the bands emanate from excitons as their frequencies lie within the range of the probed SF signal of 1.8399 eV and 1.8436 eV [103, 104, 105].

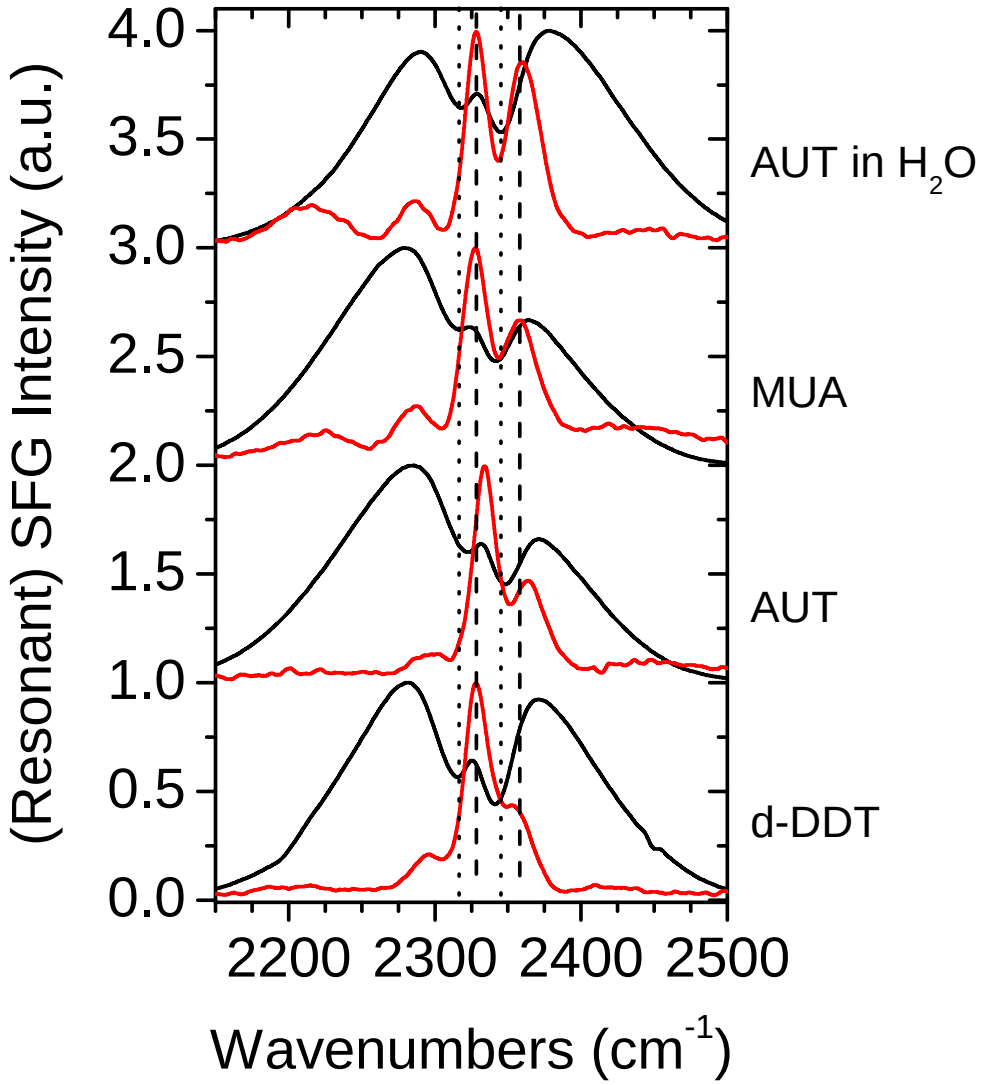

Figure 4.5: This figure depicts SFG spectra in a region where gaseous CO_2 absorbs parts of the incidence infrared light. The black curves shows spectra containing the nonresonant background whereas the red curves are background-suppressed spectra. Dotted and dashed lines mark the positions of bands in the normal and the background-suppressed spectra, respectively. Bands are located either at 2316 cm^{-1} and 2344 cm^{-1} or at 2327 cm^{-1} and 2358 cm^{-1}. For convenience all spectra were normalized to 1.

However, it is most plausible that these bands are related to specific surface plasmon resonances which can otherwise not be probed in standard IR spectroscopy as the CO_2 absorption dominates the spectrum at these positions.

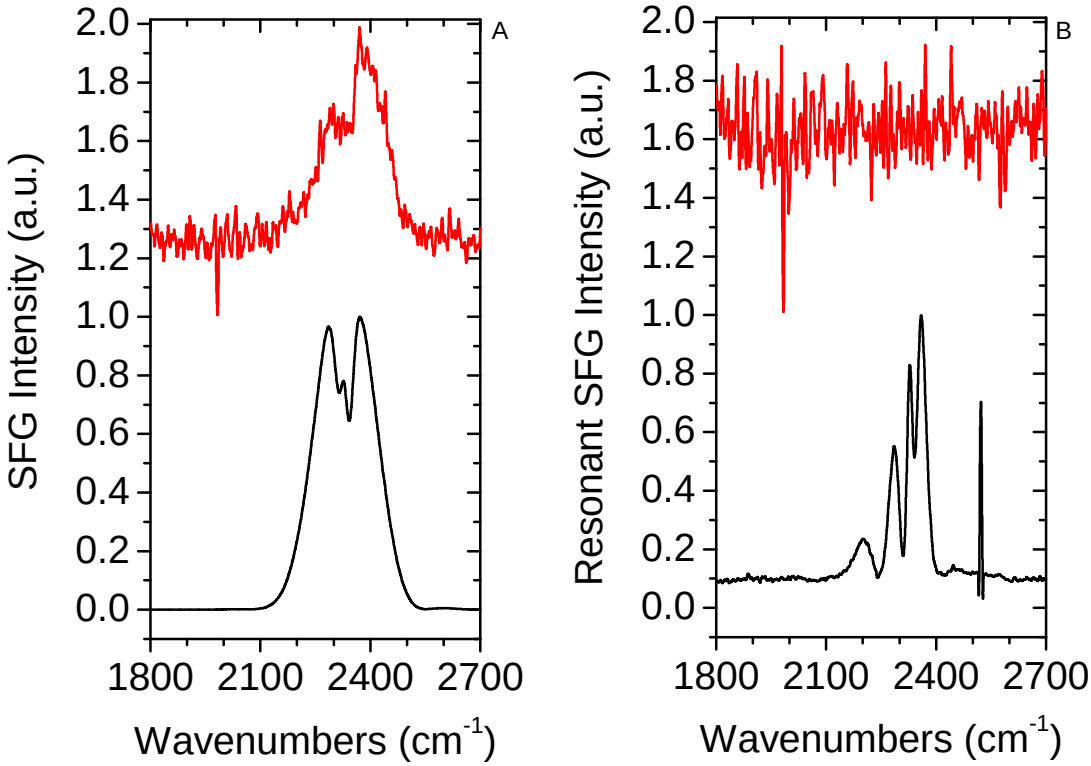

Figure 4.6: Spectra recorded from a CaF_2 prism half sputtered with gold (black) and half with titanium dioxide (red). A depicts the spectra obtained in the normal mode whereas B was measured with background suppression. Even though the intensity of titanium dioxide is much lower the two dips originating from absorbing CO_2 are visible in A. In contrast, only gold shows strong bands in the background-suppressed mode (B). From TiO_2 no such bands were detected.

4.4 Combined sum-frequency generation spectroscopy and cyclovoltammetry

The focus of the following experiment lay on the investigation of structural changes of pyridine-terminated SAMs resulting from the electrochemical desorption from a gold substrates. Prior to the actual experiment the formation and the stability of the SAMs

was determined using SFG spectroscopy in the CH stretching region. Spectra were obtained as exemplarily shown in Fig. 4.7 for PyPP2. The assignment of the observed bands can be obtained from Tab. 4.3

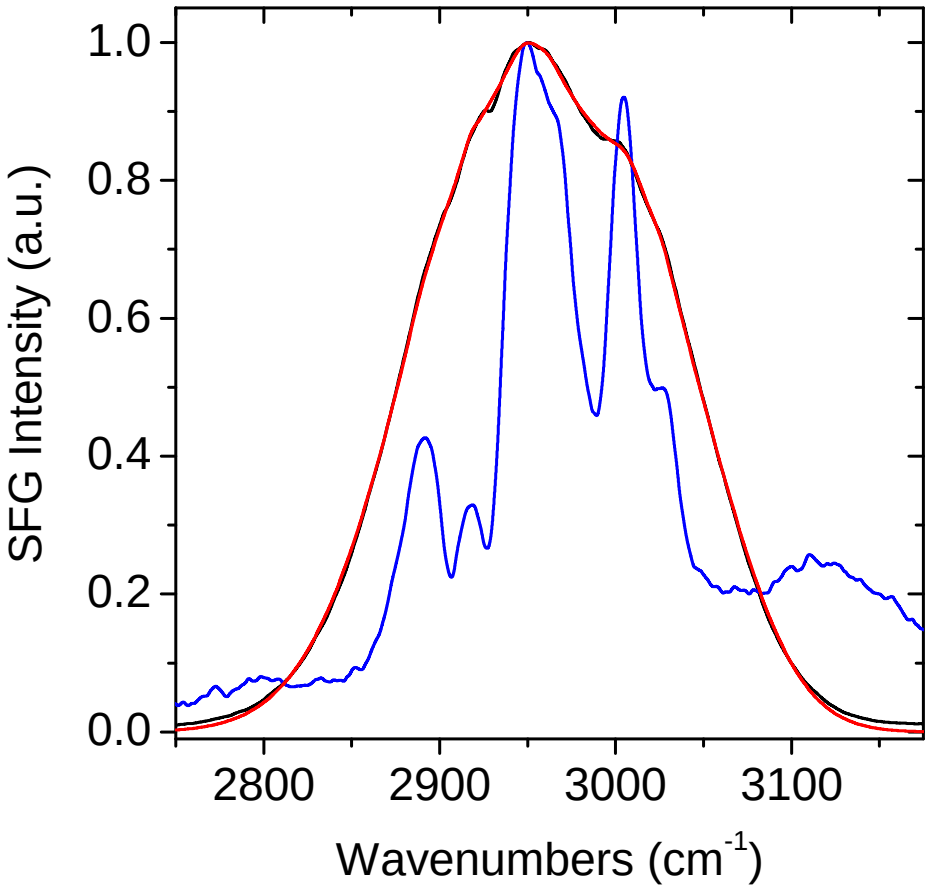

Figure 4.7: The black curve shows the recorded spectra of the spectral C-H stretching region for the PyPP2 SAM in air on gold. The fitting curve based on the background-suppressed spectrum (in blue) is depicted in red.

As a reliable and good measure of the SAM integrity a group of intense bands was additionally found in the spectral amide region around 1600 cm^{-1}. Figure 4.8 A shows in black the raw SFG spectrum, in blue the background-suppressed spectrum and in red the fit of the PyPP1 SAM. In B the respective spectra for PyPP2 are depicted. Both spectra were recorded in air to get a high signal-to-noise ratio in a reasonable time and to determine the phases of the observed bands (cf. Tab. 4.4). It was found that the probed aromatic ν_8 or C_{ar}-C_{ar} vibrations of the phenyl ring possess a phase near 0° indicating

Position	Assignment
2858 cm^{-1}	CH_2 s
2916 cm^{-1}	
2947 cm^{-1}	CH Py
2966 cm^{-1}	CH_2 FR s
3005 cm^{-1}	CH_2 as
3031 cm^{-1}	CH Ph

Table 4.3: Abbreviations: s: symmetric, as: asymmetric, FR: Fermi resonance, Ph: band mainly attributed to a vibrational mode of the phenyl ring(s), Py: band mainly attributed to a vibrational mode of the pyridine ring

an orientation of the molecular transition dipole moment away from the substrate [106]. In contrast, the C_{ar}-C_{ar} stretching vibration of the pyridine ring has a phase near 180° corresponding to an orientation towards the substrate [66]. These two findings indicate that even though the vibrations are supposed to be similar, intramolecular interactions may lead to differently oriented dipole moments of the benzene and the pyridine rings.

Position PyPP1	Position PyPP2	Assignment	Phase PyPP1	Phase PyPP2	O TDM
1514 cm^{-1}	1522 cm^{-1}	C-H phenyl, bending	165.5°	180.0°	‖
1578 cm^{-1}			47.4°		/
1602 cm^{-1}	1610 cm^{-1}	C_{ar}-C_{ar} phenyl, stretching	4.7°	1.0°	ip
1626 cm^{-1}	1633 cm^{-1}	C_{ar}-C_{ar} pyridine, stretching	175.5°	180.0°	ip

Table 4.4: Assignments and orientations of the transition dipole moment according to[2]. Abbreviations: s: symmetric, as: asymmetric, FR: Fermi resonance, O TDM: Orientation of the transition dipole moment ‖ almost of completely parallel to the molecular axis defined as line through the N-atom and the phenyl C-atom binding to the aliphatic chain; /: TDM neither parallel nor perpendicular to the molecular axis, ip: in the plane of the aromatic molecule.

After it was assured that in air the SAM structure was good and stable over time, the electrochemical cell was assembled according to section 2.4 and cyclic voltammetry and SFG spectroscopy measurements started immediately. Figure 4.9 shows the cyclovoltammograms recorded during the SFG measurements. In the voltammogram

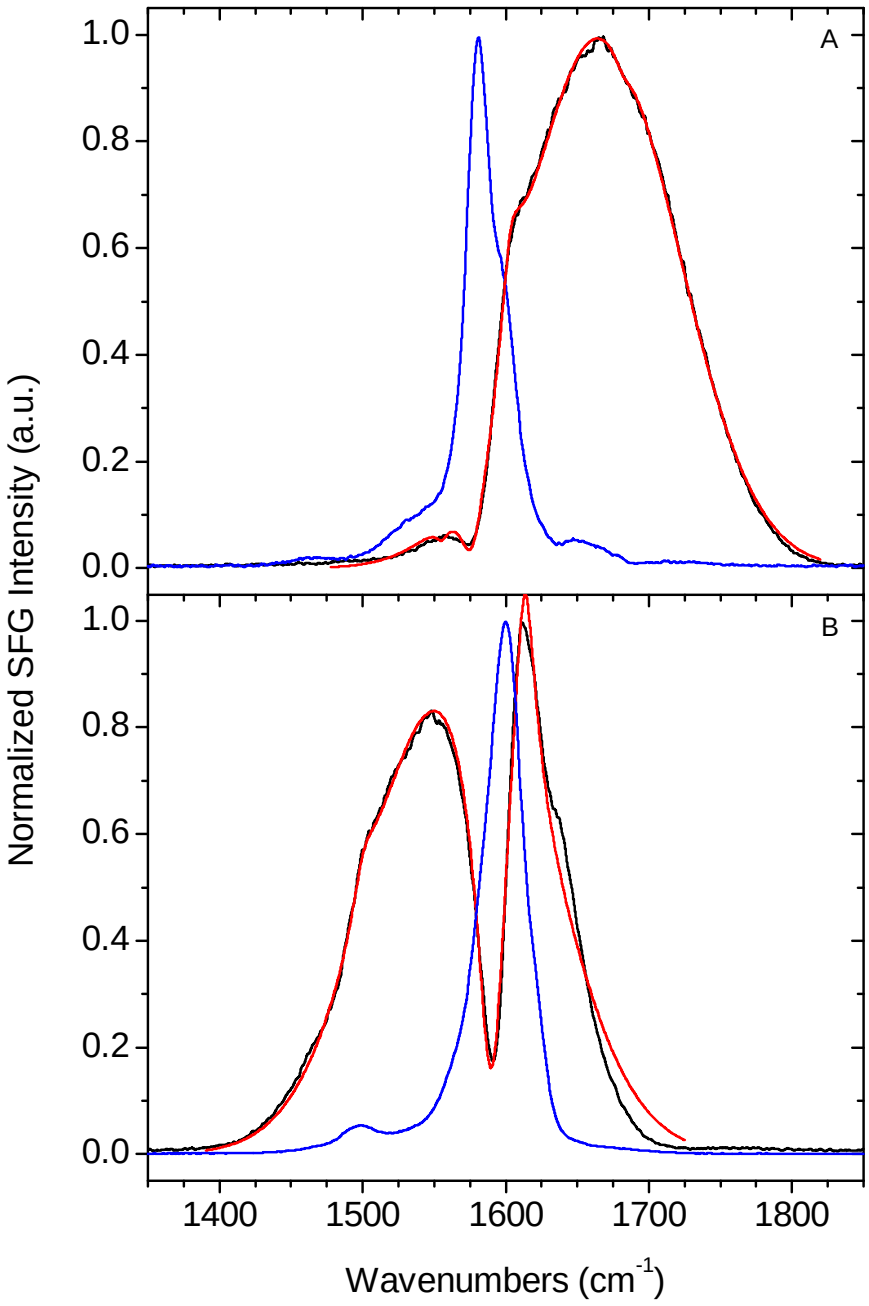

Figure 4.8: The spectral amide region for PyPP1 (A) and PyPP2 (B) is shown here. The black curve was recorded in the normal mode and fit with the standard fitting function (in red). To fix the band positions the spectra recorded in the background-suppressed mode were used (blue).

for PyPP1 (Fig. 4.9(a)) the desorption and adsorption peaks can be nicely observed. Even though they become smaller in later cycles they are still detectable. In contrast, PyPP2 only shows a desorption peak in the first cycle. Also, a slight adsorption peak is just present in the first of the ten cycles. After the first cycle no peaks are detectable in the voltammograms.

These observations are obscure and cannot be explained solely with cyclic voltammetry as well as other interface-sensitive measurements. Sum-frequency generation spectroscopy offers here the possibility to measure in parallel the voltammetric behavior and detect the changes on the surface *in situ*. The PyPP1 spectra obtained from a combined cyclic voltammetry and SFG spectroscopy measurement during the first one and a half cycles are displayed in Fig. 4.10. The depicted spectra did not undergo any data treatment. The sinusoidal behavior is remarkable and is closely related to the temporal change of the applied potential. A detailed discussion of this third-order optical phenomenon will follow in the subsequent section (4.4.1). However, an evaluation of the spectra is still possible without further knowledge of the physical background leading to this oscillation. As already described in the section on the theory of SFG (Sec. 2.1.2) the generation of a sum-frequency signal is only possible when the generating transition dipole moments are all aligned in the same direction. Furthermore, the signal scales with the degree of order. Hence it is possible to determine the order of PyPP1 and PyPP2 using the maximum of the oscillating intensity. To additionally reduce the noise the area of the bands was used instead of their maxima giving a much smoother curve. In Fig. 4.11 the evolution of the integrated intensity for each SAM is displayed versus the applied potential. Even after ten cycles PyPP1 does not show a significant decrease of the signal, whereas the intensity of PyPP2 is almost not detectable anymore. The signal of PyPP2 already declined after four cycles to half of its initial value. When the same surface density is assumed these findings indicate that PyPP1 remains in its highly state even after desorption. In contrast, PyPP2 loses its crystallinity within 4 to 5 minutes. This fact is a possible explanation for the recorded behavior in the cyclic voltammetry measurements. For PyPP2 it is not possible anymore to re-adsorb to the gold surface when the SAMs are no longer aligned in a well-ordered manner. The re-adsorption of PyPP1 though is assured as the SAM remains in its highly ordered state.

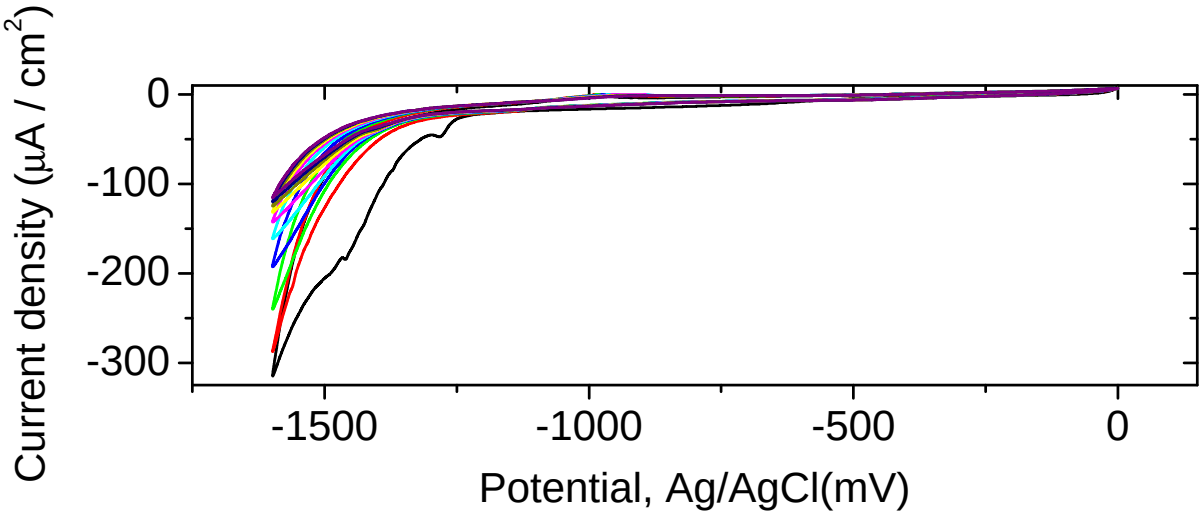

(a) PyPP1

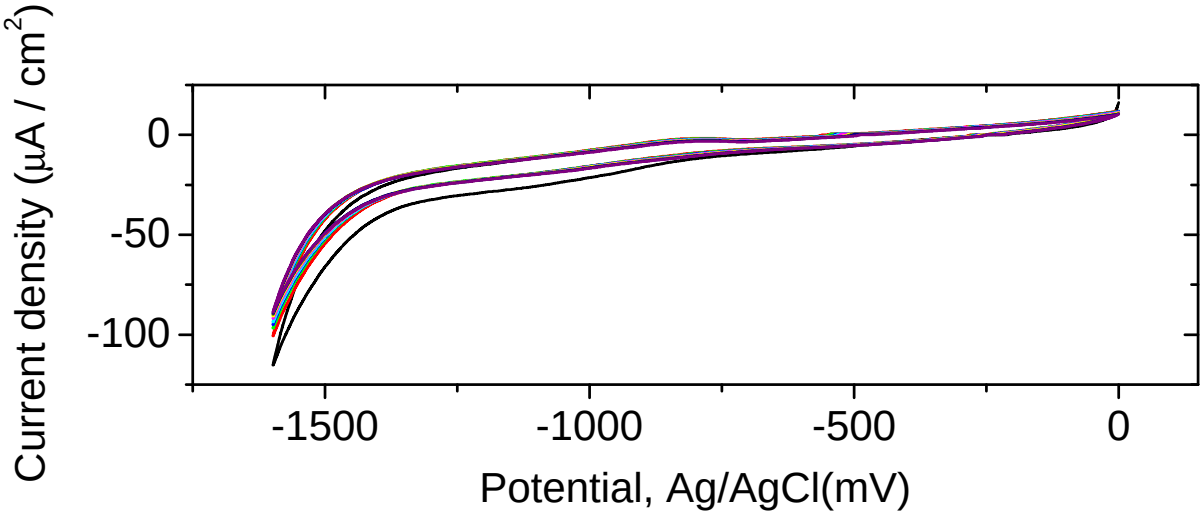

(b) PyPP2

Figure 4.9: Cyclovoltammograms of the PyPP1 and PyPP2 SAMs recorded during the SFG measurements. PyPP1 shows a huge desorption and a slight adsorption peak in the first cycle. The peaks decrease with an increasing number of cycles. In contrast, the PyPP2 SAM possesses a visible desorption peak, but only a very slight adsorption peak is present in the first cycle. The subsequent cycles do not show such peaks.

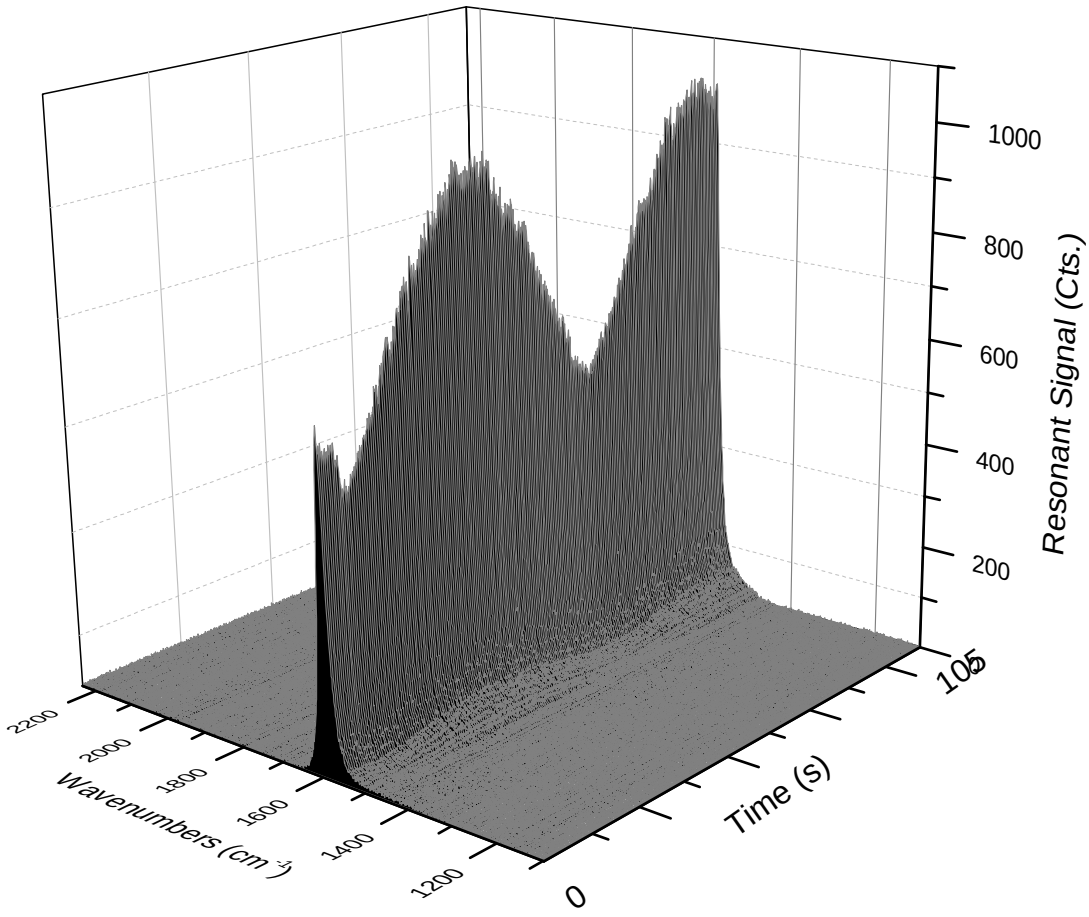

Figure 4.10: The first one and a half voltammetric cycles as recorded with SFG spectroscopy are displayed in this figure. The X and Y axes depict the wavenumbers and intensity, respectively. The Z axis shows the evolution over time. The sinusoidal behavior of the SF intensity with the applied potential is discussed in the subsequent section.

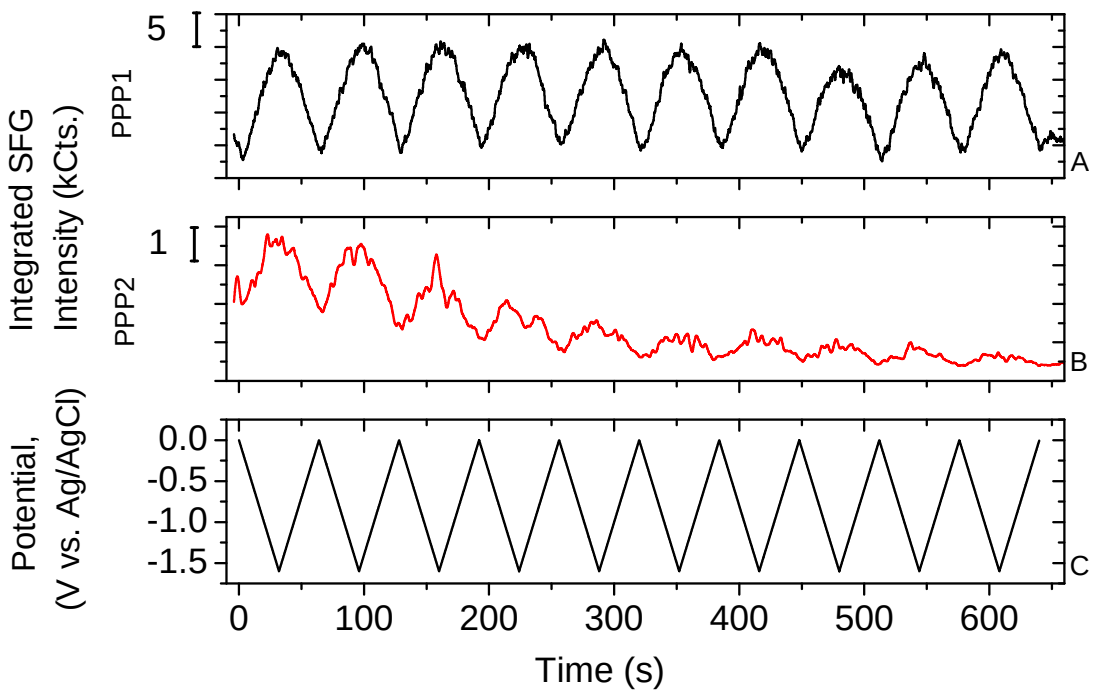

Figure 4.11: A and B show the evolutions of the integrated intensities of the SFG signal generated by the PyPP1 and PyPP2 SAM, respectively. C displays the applied potential. After ten cycles the PyPP1 intensity did not change significantly. In contrast, the signal obtained from PyPP2 vanished almost completely. Already after 4 cycles the intensity declined to half of its initial value.

The differing behavior of the two SAMs can be explained when recalling the structure of the respective SAM (Fig. 4.12). PyPP1 is oriented completely away from the gold surface, not possessing any kinks. Due to the pyridine groups and their π-π stacking interactions the PyPP1 structure seems to be so dense that no water can penetrate and disintegrate the SAM [107][108]. The interactions in the PyPP2 SAM though are weaker due to the tilt angle of more than 15°. This may allow the water molecules to enter the SAM after desorption and hence disrupt the structure. In turn PyPP2 cannot re-adsorb and maintain its crystallinity which leads to a vanishing SFG signal.

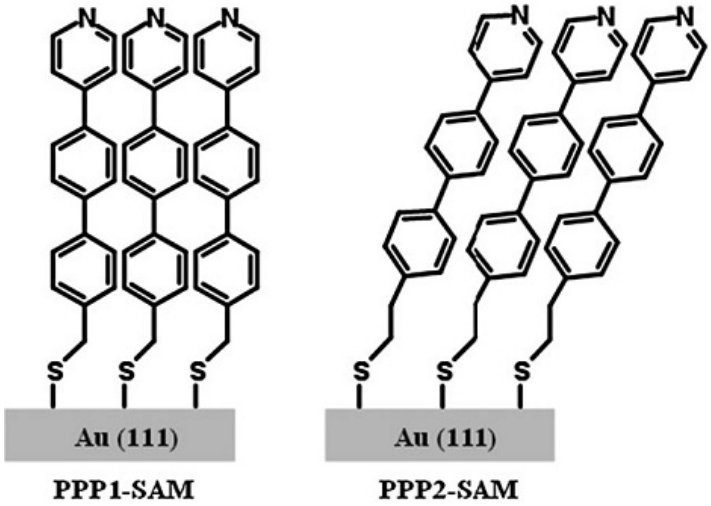

Figure 4.12: Structures of PyPP1 and PyPP2 as used in the present experiments. PyPP2 is tilted with respect to the surface normal by more than 15°. (Figure from Liu et al. [2])

4.4.1 $\chi^{(3)}$ effects in resonant and nonresonant SFG signals

A broad literature search revealed that the electrochemical studies performed in this work are the first combined SFG spectroscopy and cyclic voltammetry measurements performed in real-time with a femtosecond system. Moreover, the recorded spectra showed a sinusoidal behavior: The integrated and normalized intensity of the pyridine-related bands and of the nonresonant background is essentially depending on the varying applied potential (cf. Fig. 4.13). The intensity of the resonant SFG signal increases with an increasing potential. In contrast, the nonresonant signal of the gold background decreases as the potential is increases. This behavior is related to the fact that the

applied potential fills higher electronic bands in the gold so that the number of electrons available for the SFG process is smaller than without an additional electric field. The declining peak intensity is solely arising from issues with the experimental setup and not at all related to the underlying physical phenomena. The temporal development of the resonant signal though indicates that the applied electric field couples with the two laser beams in a nonlinear optical effect of third order. With the PyPP1 SAM this effect can be further investigated as the SAM does not change its structure upon the cyclic application of a potential. Additionally, both SFG signals follow the course of the applied potential (cf. Fig. 4.13) only with a slight shift. This is related to a potential of zero charge located at around -100 mV. This potential is characteristic for each metal. At this value the metallic electrode surface does not acquire electric charges from the electrolyte. Hence it is the potential with minimum electric field strength in the SAM.

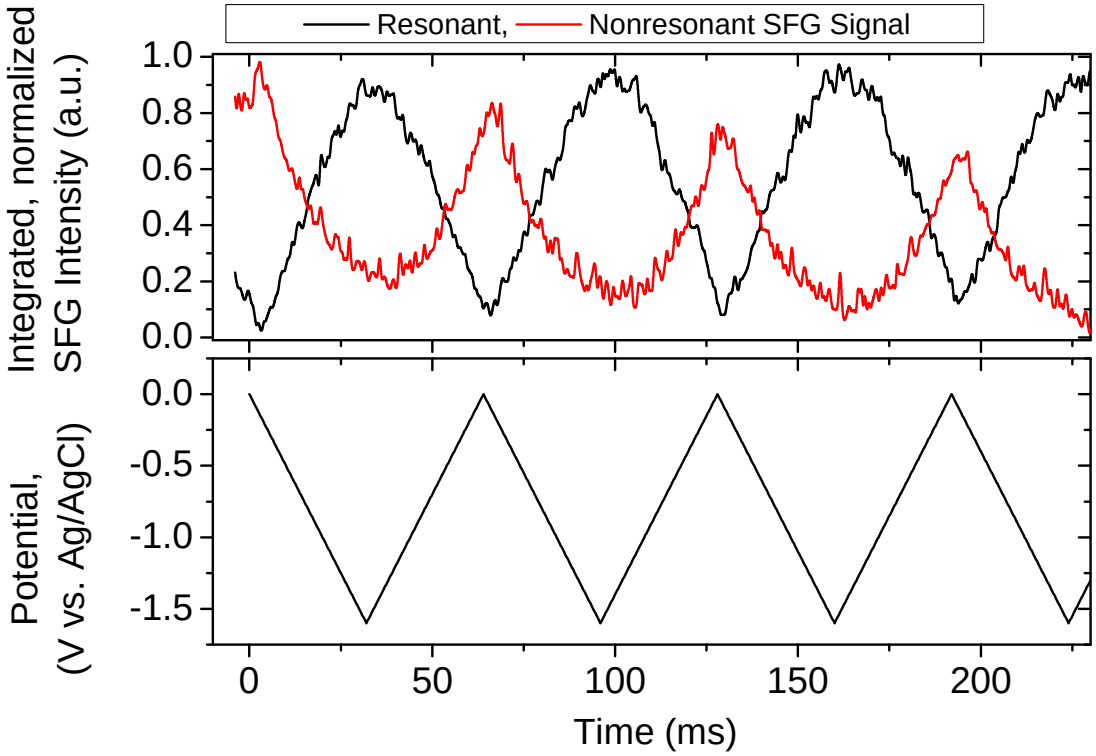

Figure 4.13: The integrated intensities of the spectra of the PyPP1 SAM recorded during the real-time cyclovoltammetric SFG measurements. The course of the intensities of the nonresonant background (red) and the SFG-active bands (black) is shifted by approximately π.

As already discussed in the methods section (2.1.2) the polarization can be expanded in a taylor series as a function of electric fields. So far, only phenomena based on two interacting fields were considered. The intensity of the sum-frequency signal is then

$$I_{\mathrm{SF}} \propto \left|\chi^{(2)}\right| I_{\mathrm{IR}} I_{\mathrm{vis}} \tag{4.1}$$

with

$$\chi^{(2)} = \chi^{(2)}_{\mathrm{NR}} + \chi^{(2)}_{\mathrm{R}} = \chi^{(2)}_{\mathrm{NR}} + \sum_k \left| \frac{A_k}{(\omega_{\mathrm{IR}} - \omega_k) + i\Gamma_k} \right| e^{i\varphi_k} \tag{4.2}$$

where $\chi^{(2)}_{\mathrm{NR}}$ and $\chi^{(2)}_{\mathrm{R}}$ are the nonresonant and resonant contributions, to the nonlinear susceptibility, respectively, φ_k is the phase difference between of resonant and nonresonant contribution, A_k is the amplitude, and Γ_k is the damping constant width of a given vibrational mode with resonant frequency ω_k.

In the present experiments the electric potential adds another electric field. This field can be considered as static since its time development is slow on the time scales of the fast oscillating incident laser light. The intensity of the sum-frequency signal generated by the electric fields at the surface differs from Eq. 4.1:

$$I \propto \left|\mathbf{P}^{(2)} + \mathbf{P}^{(3)}\right|^2 \tag{4.3}$$

$$= \left|\chi^{(2)}\mathbf{E}_{\mathrm{vis}}\mathbf{E}_{\mathrm{IR}} + \chi^{(3)}\mathbf{E}_{\mathrm{vis}}\mathbf{E}_{\mathrm{IR}}\mathbf{E}_{\mathrm{el}}\right|^2 \tag{4.4}$$

with $\mathbf{E}_{el}$ varying with time according to Eq. 4.5

$$\mathbf{E}_{\mathrm{el}} = E_0 \arcsin\sin\left(\omega(t+\sigma)\right)\mathbf{v} \tag{4.5}$$

where E_0 is the amplitude of the applied electric field and $\mathbf{v}$ is the unit vector in the field direction corresponding to the direction normal of the metal/electrolyte interface. The arcsin sin expression models here the sawtooth function of the applied cyclic potential. Thus Eq. 4.4 reads

$$I = \left|\chi^{(2)}\mathbf{E}_{\mathrm{vis}}\mathbf{E}_{\mathrm{IR}} + \chi^{(3)}\mathbf{E}_{\mathrm{vis}}\mathbf{E}_{\mathrm{IR}}\mathbf{v}E_0 \arcsin\sin\left(\omega(t+\sigma)\right)\right|^2 \tag{4.6}$$

The scalar quantity in Eq. 4.6 can be described by

$$
\begin{aligned}
I &= \sum_{m=1}^{3} \left| a_m^{(2)} + i b_m^{(2)} + a_m^{(3)} + i b_m^{(3)} \right|^2 && (4.7)\\
&= \sum_{m=1}^{3} \left(a_m^{(2)} + a_m^{(3)} \right)^2 + \left(b_m^{(2)} + b_m^{(3)} \right)^2 && (4.8)\\
&= \sum_{m=1}^{3} {a_m^{(2)}}^2 + {b_m^{(2)}}^2 + {a_m^{(3)}}^2 + {b_m^{(3)}}^2 && (4.9)\\
&\quad + 2a_m^{(2)} a_m^{(3)} + 2b_m^{(2)} b_m^{(3)}
\end{aligned}
$$

Since E_{el} is an external, (on the timescale relevant for SFG) static electric field, it can be regarded as purely real and the following relations apply

$$
\begin{aligned}
{a_m^{(2)}}^2 + {b_m^{(2)}}^2 &= C && (4.10)\\
{b_m^{(3)}}^2 = 2b_m^{(2)} b_m^{(3)} &= 0 && (4.11)\\
{a_m^{(3)}}^2 &\propto E_{el}^2 && (4.12)\\
2a_m^{(2)} a_m^{(3)} &\propto E_{el} && (4.13)
\end{aligned}
$$

with C describing any constant. Since $\mathbf{E}_{vis}$ and $\mathbf{E}_{IR}$ are considered as constant on the time scales of the applied potential Eq. 4.14 can be used to describe the temporal evolution of the SFG intensity

$$
I = C + \alpha E_0 \operatorname{arcsin}\sin\left(\omega(t+\sigma)\right) + \beta E_0^2 \operatorname{arcsin}\sin\left(\omega(t+\sigma)\right)^2 \qquad (4.14)
$$

where ω describes the frequency of the electric field changes, $\beta = {a_m^{(3)}}^2$ and $\alpha = 2a_m^{(2)} a_m^{(3)}$. σ was introduced to correct for a phase shift due to local electric fields differing from the applied potential at the surface and $C = {a_m^{(2)}}^2 + {b_m^{(2)}}^2 + {b_m^{(3)}}^2 + 2b_m^{(2)} b_m^{(3)}$. This equation accurately describes the generated nonlinear signal. Fitting the course of the signal intensity demonstrates that within the white noise the functions are in accordance with the acquired data as can be seen from Fig. 4.14. The determined fitting parameters are given in Tab. 4.5.

With the determination of the exact positions of minima and maxima for resonant SFG signal it is possible to accurately determine the change in local electric field strength caused by the SAM-substrate system. To obtain the value for the 1st maximum of the recorded signals the 1st derivative of the acquired data with respect to the

Parameter	Resonant Data
C	34219.00
α	3.97
β	- 46.04
E_0	12.02
ω	63.98
σ	29.70

Table 4.5: Fitting parameters used in the function according to the text.

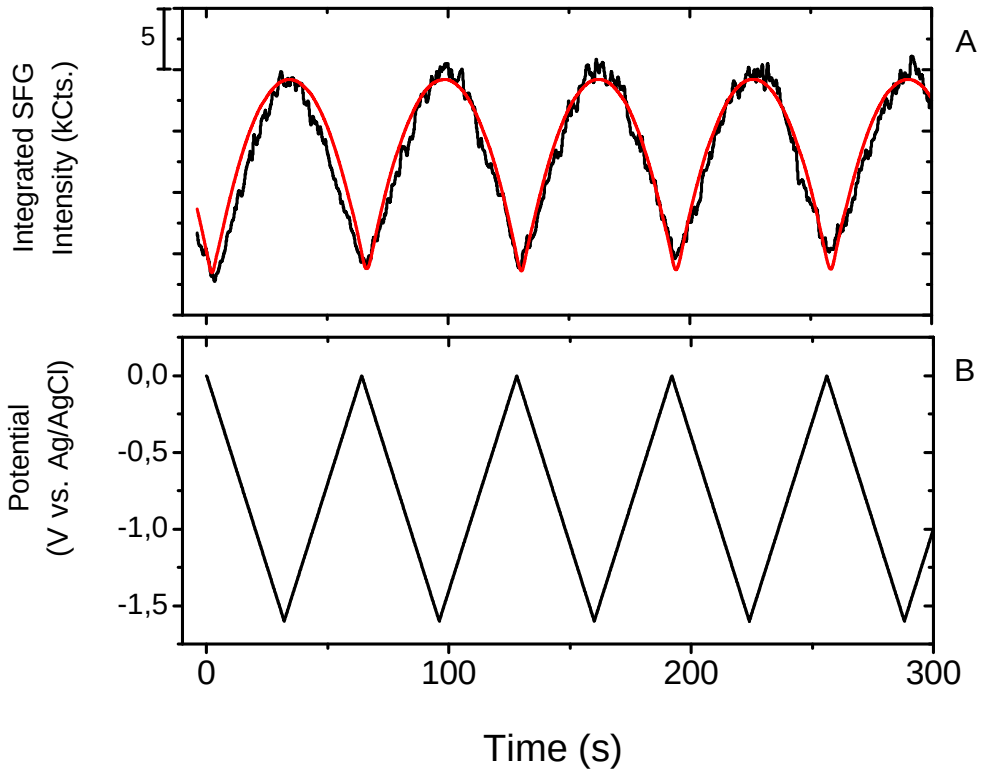

Figure 4.14: The integrated intensity of the spectra of SFG-active bands is fit with the derived function (A, in red). B additionally depicts the potential applied during the measurements.

time t is calculated (cf. Fig. 4.15) and fit with the derivative of Eq. 4.14

$$I' = \frac{\alpha E_0 \omega \cos\left((\sigma + t)\omega\right)}{\sqrt{1 - \sin\left((\sigma + t)\omega\right)^2}} + \frac{2\beta E_0^2 \omega \arcsin\sin\left((\sigma + t)\omega\right)\cos\left((\sigma + t)\omega\right)}{\sqrt{1 - \sin\left((\sigma + t)\omega\right)^2}} \tag{4.15}$$

After deriving the fit parameters (Tab. 4.6) the first zero point is calculated using a computer algebra program (Mathematica 6, Wolfram Research; Champaign, Illinois). The obtained time is $T_{\mathrm{R},0} = 2.526$ s corresponding to a potentials of $U_{\mathrm{R},\,0} = 126.4$ mV.

Parameter	**Resonant Data**
α	- 0.025
β	- 191.479
E_0	5.184
ω	63.823
σ	29.295

Table 4.6: Fit parameters used in the derivative function according to the text.

The electrochemical experiments performed with the pyridine-terminated SAMs were to the best of our knowledge the first verifications of vibrational $\chi^{(3)}$ effects with sum-frequency generation spectroscopy. The experiments also showed that this functional group obviously possesses a rather large $\chi^{(3)}$ activity resulting in a large third-order response during the coupled electrochemical and spectroscopic measurements as other groups reported only smaller third-order effects [109].

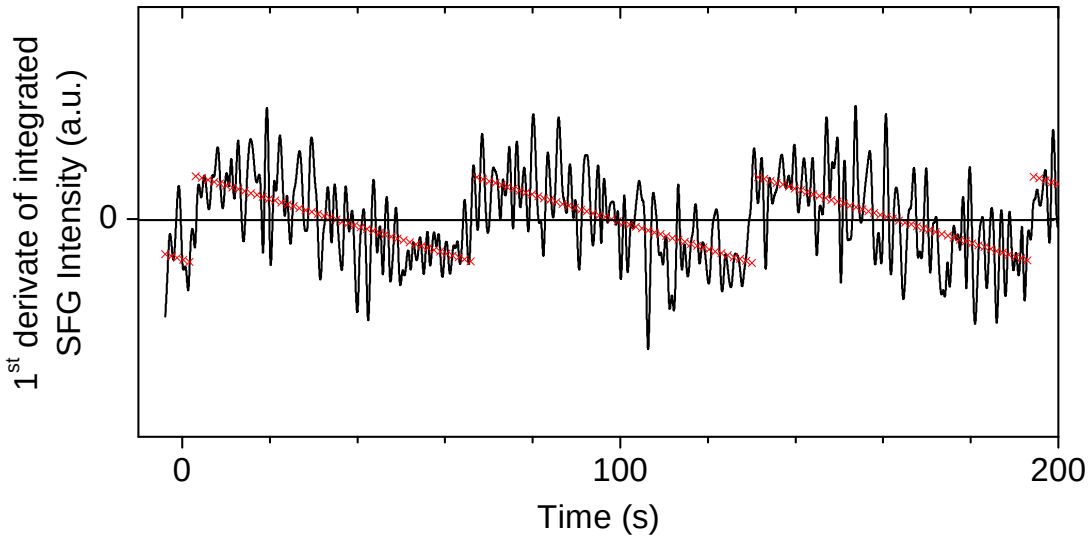

Figure 4.15: The 1st derivative of the integrated intensities of the acquired resonant spectra are shown in black. The red curves depict the fitting according to the function in Eq. 4.15.

5

Conclusions and Outlook

The focus of this thesis lay on the establishment of a platform for the investigation of phenomena related to molecular interactions with lipid bilayer membranes. It was possible to implement a procedure to produce stable supported lipid bilayers by vesicle fusion. With SFG spectroscopy bilayer-specific markers were identified in the spectral C-H stretching region allowing the detection of successfully formed supported lipid bilayers. Furthermore, the applicability of the procedures involved in bilayer formation as well as SFG spectroscopy could be tested and verified with AHLs. These biological molecules play a crucial role in prokaryotic *Quorum sensing* signaling. With deuterated AHLs the SFG-active bands were shifted into a region which is otherwise free of overlapping bands, simultaneously the bilayer markers could be kept. Bands of the deuterated AHLs could then be successfully detected. The determination of the phases of the SFG-active bands indicated an incorporation of the AHLs primarily in the upper bilayer leaflet. Moreover, from the strong bands of D-21 and D-17 it can be concluded that they are apparently highly oriented. The number of all incorporated and oriented AHL molecules though declined with a decreasing size of the AHL. In a second experiment the temporal development of the AHL-related bands was studied over 5 hrs. A declining SFG signal indicated that the AHLs diffuse through the lipid bilayer in a flipping process to compensate their concentration gradient. However, the half lives of this process were found to be exceptionally high. The half lives of D-21 and D-17 were calculated to be 14 days and 17 days, respectively. The half life of D-9 was found to be 102 days. It is speculated that the decline of this signal was rather due to a degradation process than real flipping. The half lives of D-21 and D-17 are too high

to be relevant for a signaling process which involves the crossing of the cell membrane in a diffusion or flip-flop process. This might only be an additional process occurring in nature. However, the actual biological signaling is most probably accomplished via another pathway either through an intracellular or an extracellular receptor. Therefore more research will be required in this area to identify a membrane or intracellular receptor involved in AHL signaling.

The second part of the thesis focussed on the detailed study of differently terminated SAMs. The goal was to establish a reliable measurement procedure in order to draw conclusions on the SAM conformation in contact with different media. The determination of the orientation of functional groups was successful for SAMs investigated in air. In liquid though the results were ambivalent and allowed only rather general conclusions. Future studies will now have to focus on the bands arising from the functional end groups in air as well as in liquid. This will allow to investigate the interactions of water with these groups. Also, it will be of interest to study the water bands in order to observe potential effects on the liquid. Furthermore, it was possible to assemble a sample cell for simultaneous SFG spectroscopy and electrochemical measurements in real-time. The desorption of the pyridine-terminated thiols PyPP1 and PyPP2 could be studied with this cell. The observed re-adsorption of PyPP1 is apparently related to the preservation of its structure even upon desorption. In contrast, PyPP2 loses its structure already after 4 voltammetric cycles. This is related to an additional carbon atom in the alkane chain of PyPP2 leading to a kink and thus a higher tilt angle with respect to the surface. This results in a less dense SAM structure. Therefore after desorption of PyPP2 water molecules are able to interact with the SAM and to completely disturb its structure.

During the electrochemical measurements it was possible to observe optical effects of third order generated by the additional applied electric field. A fitting function derived from nonlinear optical theory described the recorded development of the resonant SF signal. The temporal development of the nonresonant signal of gold potentailly originates from the filling of higher electronic bands thus making them unavailable for the SFG process. Furthermore, the temporal development of the signals showed an additional phase shift with respect to the applied potential. This shift originated from the potential of zero charge and hence a deviation of the local electric fields with respect

to the applied potential. The value of this shift could be determined to about 126.4 mV by calculating the exact minimum and maximum positions of the resonant signal.

Establishing the reliable production of supported lipid bilayers via vesicle fusion as well as the combination of electrochemical measurements and SFG spectroscopy will provide the way for new applications of sum frequency generation spectroscopy in the future. It will be possible to incorporate membrane proteins into the liposomes and measure their behavior and structure on a solid surface. SFG allows then to determine their reaction on specific chemical triggers e.g. new pharmaceuticals. Moreover, a combination with electrochemistry and computer-based models will allow to study the mechanism of membrane protein functionality. Thus this thesis laid the ground for future applications in a wide field of research.

The work presented in this thesis produced the following main results:

- The AHLs D-9, D-17, D-21 primarily incorporate into the upper leaflet of a supported lipid bilayer.
- The integrated AHLs are highly oriented, however their orientation or the number of the integrated molecules decreases with decreasing chain length.
- The AHLs flip through the bilayer. However, the half life of this flip-flop process is on the order of days. Hence, it cannot be relevant for signaling in bacterial biofilms.
- The molecular orientation of functional groups can be determined with SFG spectroscopy in air and *in situ*.
- SFG spectroscopy can be used in conjunction with electrochemistry to study the desorption behavior of SAMs in real-time.
- PyPP1 maintains its structure upon desorption, whereas PyPP2 loses its structure due to an additional kink.
- Nonlinear optical $\chi^{(3)}$ effects of molecular vibrations can be shown with femtosecond SFG spectrometers. These effects lead to an increasing resonant SFG signal with an increasing applied potential.

References

[1] D. Monroe, "Looking for chinks in the armor of bacterial biofilms," *PLoS Biology*, vol. 5, no. 11, pp. 2458–2461, 2007. ix, 3

[2] J. Liu, B. Schuepbach, A. Bashir, O. Shekhah, A. Nefedov, M. Kind, Terfort, and C. Woell, "Structural characterization of self-assembled monolayers of pyridine-terminated thiolates on gold," *Physical Chemistry Chemical Physics*, vol. 12, pp. 4459–4472, 2010. ix, xv, xvii, 7, 8, 89, 95

[3] D. Verreault, V. Kurz, C. Howell, and P. Koelsch, "Sample cells for probing solid/liquid interfaces with broadband sum-frequency-generation spectroscopy," *Rev. Sci. Instrum.*, vol. 81, 2010. x, 24, 26

[4] P. Laibinis, R. G. Nuzzo, and G. M. Whitesides, "Structure of monolayers formed by coadsorption of two n-alkanethiols of different chain length on gold and its relation to wetting," *J Phys Chem*, vol. 96, pp. 5097–5105, 1992. xvii, 6, 77, 83, 84

[5] H. Günzler and H.-U. Gremlich, *IR Spectroscopy - An Introduction*. Weinheim: Wiley-VCH, 2002. xvii, 45, 77

[6] L. Bellamy, *Ultrarot-Spektrum und chemische Konstitution*, vol. 2. Darmstadt: Dr. Dietrich Steinkopff Verlag, 1966. xvii, 77

[7] L. Bellamy, *The Infrared Spectra of Complex Molecules*. John Wiley & Sons, Inc., 1960. xvii, 77

[8] C. Howell, R. Maul, W. Wenzel, and P. Koelsch, "Interactions of hydrophobic and hydrophilic self-assembled monolayers with water as probed by sum-frequency-generation spectroscopy," *Chemical Physics Letters*, vol. 494, pp. 193–197, 2010. xvii, 5, 83, 84

[9] J. Costerton et al., "Bacterial biofilms in nature and disease," *Ann. Rev. Microbiol.*, vol. 41, pp. 435–464, 1987. 2

[10] J. Costerton, "The formation of biocide-resistant biofilms in industrial, natural and medical systems," *Developments in Industrial Microbiology*, vol. 25, pp. 363–372, 1984. 2

[11] T. Marrie and J. Costerton, "Morphology of bacterial attachment to cardiac pacemakers leads and power packs," *J. Clin. Microbiol.*, vol. 19, pp. 911–914, 1984. 2

[12] J. Tenney, M. Moody, K. Newman, S. Schimpff, and J. Wade, "Adherent microorganisms on lumenal surfaces of longterm intravenous catheters: Importance of staphylococcus epidermidis in patients with cancer," *Arch. Intern. Med.*, vol. 146, pp. 1949–1954, 1986. 2

[13] D. H. Choi et al., "Bacterial diversity in biofilms formed on condenser tubes in nuclear power plants," *Biofouling*, vol. 26, no. 8, pp. 953–959, 2010. 2

[14] S. Macfarlane and J. Dillon, "Microbiol biofilms in the human gastrointestinal tract," *Journal of applied Microbiology*, vol. 102, pp. 1187–1196, 2007. 2

[15] J. Costerton et al., "Bacterial biofilms: A common cause of persistent infections," *Science*, vol. 284, p. 1318 ff., 1999. 2

[16] J. Costerton and P. S. Stewart, *Persistent bacterial infections*, ch. Biofilms and device-related infections, pp. 432–439. Washington: ASM Press, 2000. 2

[17] J. Costerton and P. S. Stewart, "Antibiotic resistance of bacteria in biofilms," *The Lancet*, vol. 358, pp. 135–138, 2001. 2

[18] A. B. Semmer, W. C.B., and J. S. Mattick, "A re-examination of twitching motility in pseudomonas aeruginosa," *Microbiology*, vol. 145, pp. 2863–2873, 1999. 2

[19] D. G. Davies, "The involvement of cell-to-cell signals in the development of a bacterial biofilm," *Science*, vol. 280, p. 295, 1998. 4

[20] E. P. Greenberg et al., "Quorum-sensing in bacteria: the luxr-luxi family of cell density-responsive transcriptional regulators," *Journal of Bacteriology*, vol. 176, no. 2, pp. 269–275, 1994. 4

[21] M. Cooley, S. R. Chhabra, and P. Williams, "N-acylhomoserine lactone-mediated quorum sensing: A twist in the tail and a blow for host immunity," *Chemistry and Biology*, vol. 15, no. 11, pp. 1141 – 1147, 2008. 4

[22] K. P. Rumbaugh, J. A. Griswold, and A. N. Hamood, "The role of quorum sensing in the in vivo virulence of pseudomonas aeruginosa," *Microbes and Infection*, vol. 2, no. 14, pp. 1721 – 1731, 2000. 4

[23] D. T. Hughes and V. Sperandio, "Inter-kingdom signalling: communication between bacteria and their hosts," *Nat Rev Microbiol*, vol. 6, pp. 111–120, February 2008. 4

[24] G. Telford, D. Wheeler, P. Williams, P. T. Tomkins, P. Appleby, H. Sewell, G. S. Stewart, B. W. Bycroft, and D. I. Pritchard, "The pseudomonas aeruginosa quorum-sensing signal molecule n-(3-oxododecanoyl)-l-homoserine lactone has immunomodulatory activity," *Infect. Immun.*, vol. 66, no. 1, pp. 36–42, 1998. 4

[25] A. J. Ritchie, A. O. W. Yam, K. M. Tanabe, S. A. Rice, and M. A. Cooley, "Modification of in vivo and in vitro t- and b-cell-mediated immune responses by the pseudomonas aeruginosa quorum-sensing molecule n-(3-oxododecanoyl)-l-homoserine lactone," *Infect. Immun.*, vol. 71, no. 8, pp. 4421–4431, 2003. 4

[26] S. R. Chhabra et al., "Synthetic analogues of the bacterial signal (quorum sensing) molecule n-(3-oxododecanoyl)-l-homoserine lactone as immune modulators," *J. Med. Chem.*, vol. 46, pp. 97–104, 2003. 4

[27] K. Tateda, Y. Ishii, M. Horikawa, T. Matsumoto, S. Miyairi, J. C. Pechere, T. J. Standiford, M. Ishiguro, and K. Yamaguchi, "The pseudomonas aeruginosa autoinducer n-3-oxododecanoyl homoserine lactone accelerates apoptosis in macrophages and neutrophils," *Infect. Immun.*, vol. 71, no. 10, pp. 5785–5793, 2003. 4

[28] Z. Sabine, C. Wagner, W. Müller, G. Brenner-Weiss, F. Hug, B. Prior, U. Obst, and G. M. Haensch, "Induction of neutrophil chemotaxis by the quorum-sensing molecule n-(3-oxododecanoyl)-l-homoserine lactone," *Infect Immun*, vol. 74, pp. 5687–5692, October 2006. 4

[29] B. Heit, S. Tavener, E. Raharjo, and P. Kubes, "An intracellular signaling hierarchy determines direction of migration in opposing chemotactic gradients," *The Journal of Cell Biology*, vol. 159, no. 1, pp. 91–102, 2002. 5

[30] A. J. Ritchie, C. Whittall, J. J. Lazenby, S. R. Chhabra, D. I. Pritchard, and M. A. Cooley, "The immunolomodulatory pseudomonas aeruginosa signalling molecule n-(3-oxododecanoyl)-l-homoserine lactone enters mammalian cells in an unregulated fashion," *Immunology and Cell Biology*, vol. 85, pp. 596–602, 2007. 5

[31] J. Baio, T. Weidner, J. Brison, D. Graham, L. J. Gamble, and D. G. Castner, "Amine terminated sams: Investigating why oxygen is present in these films," *Journal of Electron Spectroscopy and Related Phenomena*, vol. 172, pp. 2–8, 2009. 5

[32] C. D. Bain, "Sum-frequency vibrational spectroscopy of the solid/liquid interface," *J. Chem. Soc. Faraday Trans*, vol. 91, no. 9, pp. 1281–1296, 1995. 5, 19

[33] M. Himmelhaus, F. Eisert, M. Buck, and M. Grunze, "Self-assembly of n-alkanethiol monolayers: A by ir-visible sum frequency spectroscopy (sfg)," *J. Phys. Chem. B*, vol. 104, pp. 576–584, 2000. 5, 6, 11, 83

[34] J. Liu and J. C. Conboy, "Direct measurement of the transbilayer movement of phospholipids by sum-frequency vibrational spectroscopy," *JACS*, vol. 126, pp. 8376–8377, 2004. 5, 69

[35] X. Chen and Z. Chen, "Sfg studies on interactions between antimicrobial peptides and supported lipid bilayers," *Biochimica et Biophysica Acta*, vol. 1758, pp. 1257–1273, 2006. 5, 59

[36] J. Lahiri et al., "Method for fabricating supported bilayer lipid membranes on gold," *Langmuir*, vol. 16, pp. 7805–7810, 2000. 5

[37] C. D. Bain, E. B. Troughton, Y. T. Tao, J. Evall, G. M. Whitesides, and R. G. Nuzzo, "Formation of monolayer films by the spontaneous assembly of organic thiols from solution onto gold," *J. Am. Chem. Soc.*, vol. 111, pp. 321–335, 1989. 6

[38] J. C. Love, L. A. Estroff, J. K. Kriebel, R. G. Nuzzo, and G. M. Whitesides, "Self-assembled monolayers of thiolates on metals as a form of nanotechnology," *Chem. Rev.*, vol. 105, no. 4, pp. 1103–1170, 2005. 6

[39] R. Wang, M. Himmelhaus, J. Fick, S. Herrwerth, W. Eck, and M. Grunze, "Interaction of self-assembled monolayers of oligo(ehylene glycol)-terminated alkanethiols with water studied by vibrational sum-frequency generation," *Journal of Chemical Physics*, vol. 122, 2005. 7, 83

[40] A. V. Benderskii et al., "Molecular organization in sams used for neuronal cell growth," *Langmuir*, vol. 24, pp. 4097–4106, 2008. 7, 11, 83

[41] O. Mermut and G. A. Somorjai et al., "In situ adsorption of a 14-amino acid leucine-lysine peptide onto hydrophobic polystyrene and hydrophilic silica surfaces using quartz crystal microbalance, atomic force microscopy and sum frequency generation vibrational spectroscopy," *JACS*, vol. 128, pp. 3598–3607, 2006. 7

[42] P. Harder, M. Grunze, R. Dahint, G. Whitesides, and P. Laibinis, "Molecular conformation in oligo(ethylene glycol)-terminated self-assembled monolayers on gold and silver surfaces determines their ability to resist protein adsorption," *J. Phys. Chem. B*, vol. 102, pp. 426–436, 1998. 7

[43] O. Shekhah, C. Busse, A. Bashir, F. Turcu, X. Yin, P. Cyganik, A. Birkner, W. Schuhmann, and C. Woell, "Electrochemically deposited pd islands on an organic surface: the presence of coulomb blockade in stm i(v) curves at room temperature," *Physical Chemistry Chemical Physics*, vol. 8, pp. 3375–3378, 2004. 7

[44] P. Oelhafen et al., "A new approach to the electrochemical metallization of organic monolayers: Palladium deposition onto a 4,4'-dithiopyridine self-assembled monolayer," *Advanced Materials*, vol. 16, no. 22, p. 2024, 2004. 7

[45] S. Yoshimoto, "Molecular assemblies of functional molecules on gold electrode surfaces studied by electrochemical scanning tunneling microscopy: Relationship between function and adlayer structures," *Bulletin of the Chemical Society of Japan*, vol. 79, no. 8, pp. 1167–1190, 2006. 7

[46] C. Woell et al., "Ir spectroscopic characterization of sams made from homologous series of pyridine disulfides," *Journal of Electron Spectroscopy and Related Phenomena*, vol. 172, no. 1-3, pp. 120–127, 2009. 7

[47] M. Zharnikov et al., "Self-assembly of a pyridine-terminated thiol monolayer on au(111)," *Langmuir*, vol. 25, no. 2, pp. 959–967, 2009. 7

[48] M. Zharnikov et al., "X-ray photoelectron spectroscopy and near-edge x-ray absorption fine structure study of water adsorption on pyridine-terminated thiolate self-assembled monolayers," *Langmuir*, vol. 20, pp. 11022–11029, 2004. 7

[49] H. Taira et al., "Simple methods for preparation of a well-defined 4-pyridinethiol modified surface on au(111) electrodes for cytochrome c electrochemistry," *Electrochimica Acta*, vol. 45, no. 18, pp. 2843–2853, 2000. 7

[50] Y.-T. Long, H.-T. Rong, M. Buck, and M. Grunze, "Odd-even effects in the cyclic voltammetry of self-assembled monolayers of biphenyl based thiols," *Journal of Electroanalytical Chemistry*, vol. 524, pp. 62–67, 2002. 8

[51] P. Franken, A. Hill, C. Peters, and G. Weinreich, "Generation of optical harmonics," *Physical Review Letters*, vol. 7, pp. 118–119, 1961. 9

[52] Y. Shen, *The principles of nonlinear optics*, vol. 1. Hoboken, New Jersey: Wiley, 2003. 9

[53] A. Tadjeddine and P. Guyot-Sionnest, "Study of ag(111) and au(111) electrodes by optical second-harmonic generation," *J. Chem. Phys.*, vol. 92, p. 734 ff., 1990. 9

[54] F. M. Geiger, "Second harmonic generation, sum frequency generation and $\chi 3$: Dissecting environmental interfaces with a nonlinear optical swiss army knife," *Annual Review of Physical Chemistry*, vol. 60, pp. 61–83, 2009. 11, 22

[55] M. J. Shultz, C. Schnitzer, D. Simonelli, and S. Baldelli, "Sum frequency generation spectroscopy of the aqueous interface: Ionic and soluble molecular solutions," *International Reviews in Physical Chemistry*, vol. 19, no. 1, pp. 123–153, 2000. 11

[56] D. E. Gragson, B. M. McCarty, and G. L. Richmond, "Ordering of interfacial water molecules at the charged air/water interface observed by vibrational sum frequency generation," *Journal of the American Chemical Society*, vol. 119, no. 26, pp. 6144–6152, 1997. 11

[57] J. Kim and G. A. Somorjai, "Molecular packing of lysozyme, fibrinogen, and bovine serum albumin on hydrophilic and hydrophobic surfaces studied by infraredâ^'visible sum frequency generation and fluorescence microscopy," *Journal of the American Chemical Society*, vol. 125, no. 10, pp. 3150–3158, 2003. PMID: 12617683. 11

[58] C. Howell, M.-O. Diesner, M. Grunze, and P. Koelsch, "Probing the extracellular matrix with sum-frequency-generation spectroscopy," *Langmuir*, vol. 24, pp. 13819–13821, 2008. 11

[59] J. Liu and J. C. Conboy, "Phase transition of a single lipid bilayer measured by sum-frequency vibrational spectroscopy," *JACS*, vol. 126, pp. 8894–8895, 2004. 11

[60] X. Chen, J. Wang, A. P. Boughton, C. B. Kristalyn, and Z. Chen, "Multiple orientation of melittin inside a single lipid bilayer determined by combined vibrational spectroscopic studies," *JACS*, vol. 129, pp. 1420–1427, 2007. 11

[61] X. Chen, H. Tang, M. Even, J. Wang, G. Tew, and Z. Chen, "Observing a molecular knife at work," *JACS*, vol. 128, pp. 2711–2714, 2006. 11

[62] M. Born and E. Wolf, *Principles of Optics: Electromagnetic Theory of Propagation, Interference and Diffraction of Light*, vol. 7. Cambridge University Press, 1999. 12

[63] P. P. Banerjee, *Nonlinear Optics*, vol. 10. New York: Marcel Dekker Inc, 2004. 12

[64] L. Dreesen, C. Humbert, M. Celebi, J. Lemaire, A. Mani, P. Thiry, and A. Peremans, "Influence of the metal electronic properties on the sum-frequency generation spectra of dodecanethiol self-assembled monolayers on pt (111), ag (111) and au (111) single crystals," *Appl. Phys. B*, vol. 74, pp. 621–625, 2002. 19

[65] R. W. Boys, *Nonlinear Optics*, vol. 3. Elsevier, 2008. 19

[66] R. N. Ward, P. B. Davies, and C. D. Bain, "Orientation of surfactants adsorbed on a hydrophobic surface," *J. Phys. Chem.*, vol. 97, pp. 7141–7143, 1993. 20, 65, 82, 89

[67] A. Lagutchev, S. A. Hambir, and D. D. Dlott, "Nonresonant background suppression in broadband vibrational sum-frequency generation spectroscopy," *Physical Chemistry Letters C*, vol. 111, pp. 13645–13647, 2007. 21

[68] H. Stoecker, *Taschenbuch der Physik*, vol. 4. Harri Deutsch, frankfurt am main ed., 2000. 24

[69] M. Skoda, R. Jacobs, S. Zorn, and S. F., "Optimizing the pmirras signal from a multilayer system and application to self-assembled monolayers in contact with liquids," *Journal of Electron Spectroscopy and Related Phenomena*, vol. 172, no. 1-3, pp. 21–26, 2009. 26

[70] L. K. Tamm and S. A. Tatulian, "Infrared spectroscopy of proteins and peptides in bilayers," *Quarterly Reviews of Biophysics*, vol. 30, no. 4, pp. 365–429, 1997. 30

[71] E. Sackmann, "Supported membranes: Scientific and practical applications," *Science*, vol. 271, pp. 43–48, 1996. 30

[72] L. K. Tamm and H. M. McConnell, "Supported phosphlipid bilayers," *Biophysical Journal*, vol. 47, pp. 105–113, 1985. 30

[73] R. Richter, A. Mukhopadhyay, and A. Brisson, "Pathways of lipid vesicle deposition on solid surfaces: A combined qcm-d and afm study," *Biophysical Journal*, vol. 85, pp. 3035–3047, 2003. 30, 35, 49

[74] J. Wilschut, N. Duezguenes, and D. Papahadjopoulos, "Calcium/magnesium specificity in membrane fusion: kinetics of aggregation and fusion of phosphatidylserine vesicles and the role of bilayer curvature," *Biochemistry*, vol. 20, no. 11, pp. 3126–3133, 1981. 30

[75] A. Kunze, F. Zhao, A.-K. Marel, S. Svedhem, and B. Kasemo, "Ion-mediated changes of supported lipid bilayers and their coupling to the substrate. a case of bilayer slip?," *Soft Matter*, 2011. 30

[76] E. Kalb, S. Frey, and L. K. Tamm, "Formation of supported planar bilayers by fusion of vesicles to supported phospholipid monolayers," *Biochimica et Biophysica Acta*, vol. 1103, pp. 307–316, 1992. 30

[77] M. L. Wagner and L. K. Tamm, "Tethered polymer-supported planar lipid bilayers for reconstitution of integral membrane proteins: Silane-polyethyleneglycol-lipid as a cushion and covalent linker," *Biophysical Journal*, vol. 79, pp. 1400–1414, 2000. 30

[78] A.-S. Andersson, K. Glasmäster, D. Sutherland, U. Liedberg, and B. Kasemo, "Cell adhesion on supported lipid bilayers," *Journal of Biomedical Materials Research Part A*, 2001. 31

[79] E. Briand, M. Zäch, S. Svedhem, B. Kasemo, and S. Petronis, "Combined qcm-d and eis study of supported lipid bilayer formation and interaction with pore-forming peptides," *Analyst*, vol. 135, pp. 343–350, 2010. 31

[80] R. P. Richter et al., "Formation of solid-supported lipid bilayers: An integrated view," *Langmuir*, vol. 22, pp. 3497–3505, 2006. 33, 35, 57

[81] G. Sauerbrey, "Verwendung von Schwingquarzen zur Waegung duenner Schichten und zur Mikrowaegung," *Zeitschrift fuer Physik*, vol. 155, pp. 206–222, 1959. 35

[82] A. J. Bard, ed., *Electroanalytical chemistry*. New York, NY: Dekker. 35

[83] Y. Okahata and H. Ebato, "Absorption behaviors of surfactant molecules on a lipid-coated quartz-crystal microbalance. an alternative to eye-irritant tests," *Analytical Chemistry*, vol. 63, no. 3, pp. 203–207, 1991. 35

[84] R. C. Ebersole and M. D. Ward, "Amplified mass immunosorbent assay with a quartz crystal microbalance," *JACS*, vol. 110, no. 26, pp. 8623–8628, 1988. 35

[85] C. Keller, K. Glasmäster, V. Zhdanov, and B. Kasemo, "Formation of supported membranes from vesicles," *Physical Review Letters*, vol. 84, no. 23, pp. 5443–5446, 2000. 35

[86] C. Lu and A. Czanderna, eds., *Applications of piezoelectric quartz crystal microbalances*, vol. 7. Amsterdam, Oxford, New York, Tokyo: Elsevier, 1984. 35

[87] M. Rodahl, F. Höök, A. Krozer, P. Brzezinski, and B. Kasemo, "Quartz crystal microbalance setup for frequency and q-factor measurements in gaseous and liquid environments," *Rev. Sci. Instrum.*, vol. 66, pp. 3924–3930, July 1995. 36

[88] K. Heister, M. Zharnikov, L. Johannson, and M. Grunze, "Adsorption of alkanethiols and biphenylthiols on au and ag substrates: A high-resolution x-ray photoelectron spectroscopy study," *J Phys Chem B*, vol. 105, pp. 4058–1061, 2001. 39

[89] J. T. Woodward, M. L. Walker, C. W. Meuse, D. J. Vanderah, G. Poirier, and A. L. Plant, "Effect of an Oxidized Gold Substrates on Alkanethiol Self-Assembly," *Langmuir*, vol. 16, pp. 5347–5353, 2000. 39

[90] S. Jiang et al., "Improved method for the preparation of carboxylic acid and amine terminated self-assembled monolayers of alkanethiolates," *Langmuir*, vol. 21, no. 7, pp. 2633–2636, 2005. 40

[91] B. Schuepbach and A. Terfort, "A divergent synthesis of oligoarylalkanethiols with lewis-basic n-donor termini," *Organic and biomolecular Chemistry*, vol. 8, pp. 3552–3562, 2010. 40

[92] R. M. Murphy, "Static and dynamic light scattering of biological macromolecules: what can we learn?," *Current Opinion in Biotechnology*, vol. 8, pp. 25–30, 1997. 41

[93] F. Hallett, J. Watton, and P. Krygsman, "Vesicle sizing: Number distributions by dynamic light scattering," *Biophysical Journal*, vol. 59, pp. 357–362, 1991. 41

[94] S. Egelhaar et al., "Determination of the size distribution of lecithin liposomes: a comparative study using freeze fracture, cryoelectron microscopy and dynamic light scattering," *Journal of Microscopy*, vol. 184, no. 3, pp. 214–228, 1996. 41

[95] B. J. Frisken, "Revisiting the method of cumulants for the analysis of dynamic light scattering data," *Applied Optics*, vol. 40, no. 24, pp. 4087–4091, 2001. 41

[96] R. Stock and W. Ray, "Interpretation of photon correlation spectroscopy data: A comparison of analysis methods," *J Pol Sci B*, vol. 23, pp. 1393–1447, 1985. 42

[97] J. L. Ihrig and D. Y. Lai, "Contact angle measurement," *Journal of chemical education*, vol. 34, no. 4, p. 196 ff., 1957. 44

[98] A. Stalder, G. Kulik, D. Sage, L. Barbieri, A. Stalder, G. Kulik, D. Sage, L. Barbieri, and P. Hoffmann, "A snake-based approach to accurate determination of both contact points and angles," *Colloids and Surface A: Physicochemical and Engineering Aspects*, vol. 286, no. 1-3, pp. 92–103, 2006. 44

[99] X. Chen, M. Clarke, J. Wang, and Z. Chen, "Sum frequency generation vibrational spectroscopy studies on molecular conformation and orientation of biological molecules at interfaces," *International Journal of Modern Physics B*, vol. 19, no. 4, pp. 691–713, 2005. 59

[100] C. S.-C. Yang, L. J. Richter, J. C. Stephenson, and K. A. Briggman, "In situ, vibrationally resonant sum frequency spectroscopy study of the self-assembly of dioctadecyl disulfide on gold," *Langmuir*, vol. 18, no. 20, pp. 7549–7556, 2002. xvii, 65, 66

[101] M. D. Porter, T. B. Bright, D. L. Allara, and C. E. Chidsey, "Spontaneously organized molecular assemblies. 4. structural characterization of n-alkyl thiol monolayers on gold by optical ellipsometry, infrared spectroscopy, and electrochemistry," *J. Am. Chem. Soc.*, vol. 109, pp. 3559–3568, 1987. 79, 83

[102] A. Hooper, D. Werho, T. Hopeon, and O. Palmer, "Evaluation of amine- and amide-terminated self-assembled monolayers as molecular glues for au and sio2 substrates," *Surface and Interface Analysis*, vol. 31, pp. 809–814, 2001. 83

[103] T. Dekorsy, V. Yakolev, W. Seidel, M. Helm, and F. Keilmann, "Infrared-phonon-polariton resonance of the nonlinear susceptibility in gaas," *Physical Review Letters*, vol. 90, no. 5, 2003. 85

[104] D. Boggetti and R. Loudon, "Theory of two-photon absorption by polaritons," *Physical Review Letters*, vol. 28, no. 16, 1972. 85

[105] N. Singh and S. Prakash, "Phonon frequencies and cohesive energies of copper, silver and gold," *Physical Review B*, vol. 8, no. 12, p. 5532 ff, 1973. 85

[106] E. B. Wilson, "The normal modes and frequencies of vibration of the regular plane hexagon model of the benzene molecule," *Physical Review*, vol. 45, p. 706, 1934. 89

[107] H. W. Roesky and M. Andruh, "The interplay of coordinative, hydrogen bonding and pi–pi stacking interactions in sustaining supramolecular solid-state architectures.: A study case of bis(4-pyridyl)- and bis(4-pyridyl-n-oxide) tectons," *Coordination Chemistry Reviews*, vol. 236, no. 1-2, pp. 91–119, 2003. 95

[108] M.-G. Choi and R. J. Angelici, "Pyridine-pyridine pi-pi stacking interactions in pentacarbonyl[pyridine-4(1h)-thione]tungsten(0)," *Acta Crystallographica Section C*, vol. C56, pp. 808–810, 2000. 95

[109] W. Zheng, O. Pluchery, and A. Tadjeddine, "Sfg study of platinum electrodes in perchloric acid solutions," *Surface science*, vol. 502-503, pp. 490–497, Jan 2002. 100

Acknowledgements

This work was performed at the Institute of Toxicology and Genetics at the Karlsruhe Institute of Technology under the supervision of Patrick Koelsch. First I would like to express him my deepest thanks for introducing me into the technique of nonlinear optical spectroscopy. He also helped me with his broad knowledge and supported me during my time in his group wherever he could. Secondly, I would like to thank Prof. Dr. Joachim Spatz for taking the first referee position.

Then, I would like to thank my group members Dominique Verreault, Anne Keese, Volker Kurz, Caitlin Howell, Mark-Oliver Diesner and Markus Niermeyer for helping with fruitful discussions and for making the time in the group as enjoyable as possible.

Furthermore, I would like to thank Sofia Svedhem from the Chalmers University of Technology and Frances Anastassacos from the University of St. Andrews for help with lipid bilayer production and QCM-D measurements. Another big thank you goes to Stefan Heissler from the IFG for help with the IRRAS measurements and Hans-Michael Bruns and his team for preparation of the gold wafers and XPS measurements. Also I would like to thank Dorota Jakubczyk for the preparation of deuterated AHLs.

A great thanks goes to Pancho Bezanilla for having the possibility to spent three months in his group at the University of Chicago in order to learn all techniques necessary for the success of this thesis. Especially, I would like to thank Sebastian Villareal and Jeremy Treger.

Also, I would like to greatly acknowledge financial support from the Exzellenzinitiative and the BioInterfaces International Graduate School.

I would also like to thank Prof. Bernhard Steinhoff for his catching optimism especially in difficult situations.

Thank you, Mom and Dad, for always supporting me in my childhood and now.

Finally, I want to thank Kerstin for believing in me and making life besides work just great. Sweetheart, I know life wasn't always easy with me, but together we can make it everywhere.

I hereby affirm that I have written this thesis independently and without use of resources other than those quoted. Cited and copied work is marked as such.

Oftersheim, November 21, 2011

Christoph Barth